



18th International Microscopy Congress

Prague, Czech Republic

7 - 12 September, 2014

APPENDIX TO THE PROCEEDINGS

LATE POSTERS

IFSM



Copyright© 2014 Czechoslovak Microscopy Society

No parts of this publication may be reproduced, stored in a retrieval system or transmitted in any form or by any means without the written permission of the publisher, except as stated below. Single photocopies of abstracts may be made for private study or research. Illustrations and short extracts from the text of individual abstracts may be copied provided that the source is acknowledged and permission of the authors has been obtained.

The publishers have made every effort to reproduce the figures at optimum contrast and with optimum resolution from the original material provided by the authors. The publishers accept no liability for the loss of image quality resulting from supply of low quality material or improperly prepared digital records. The content of the individual abstracts remains the responsibility of the respective authors.

Table of Content

IT-1. Electron optics and optical elements

[Poster] IT-1-P-6140 Toward holographic approach to spherical aberration correction in STEM

IT-3. Super-resolution light microscopy and nanoscopy imaging

[Poster] IT-3-P-6078 Beyond Electron Microscopy with Super-Resolution Nanoscopy in Soft Matter

IT-4. Scanning electron microscopy

[Poster] IT-4-P-6101 Direct-write chlorine based etching of semiconductor devices utilizing a SEM

[Poster] IT-4-P-6105 New opportunities for biomedical research in the Saint-Petersburg State University

[Poster] IT-4-P-6135 airSEM™, high resolution SEM operating in open air, a new approach for correlative imaging of hydrated samples

[Poster] IT-4-P-6136 airSEM™: Enabling EDX material analysis in open air

[Poster] IT-4-P-6138 airSTEM: high resolution STEM detection in open air

IT-7. In-situ microscopic techniques and cryo-microscopies

[Poster] IT-7-P-6125 Beyond Current SEM – AFM Solutions: A Highly Flexible in-situ AFM for Correlated Microscopy in Micromechanical Testing

[Poster] IT-7-P-6127 In situ observations of confined platinum nanoparticles coalescing within carbon nanotubes

IT-8. Ultrafast and high-throughput microscopies

[Poster] IT-8-P-6102 Development of femtosecond time-resolved relativistic-energy electron microscopy

[Poster] IT-8-P-6122 High-Throughput Characterization of Nanoparticles by TEM

IT-10. Electron tomography

[Poster] IT-10-P-6113 On resolution in electron tomography of beam sensitive materials

IT-11. Electron holography and lens-less imaging

[Poster] IT-11-P-6126 Three-wave electron vortex lattices for vortex interferometry

IT-12. Surface microscopy, spectromicroscopy and microspectroscopy

[Poster] IT-12-P-6115 Angle-Resolved Cathodoluminescence Imaging Spectroscopy

IT-13. Focused ion beam microscopy and techniques

[Poster] IT-13-P-6109 High Resolution, Stable and Low Damage FIB Nanofabrication employing Gallium and New Ion Species

IT-16. Electron microscopy theory and simulations

[Poster] IT-16-P-6075 Examination of the possibility of application of the Monte Carlo method for study of electron diffraction of textured nanocomposite materials

[Poster] IT-16-P-6106 Improving quantification in Scanning Electron Microscopy by comparing transmission experiments with Monte Carlo Simulation.

[Poster] IT-16-P-6132 Resolution Simulation of the Practical Rayleigh Criterion Taking Account of Particle Diameter and Contrast-to-Noise Ratio for Scanning Electron Microscopes

IT-17. Atom probe and non-traditional microanalytical tasks

[Poster] IT-17-P-6104 Sub-angstrom resolution in 3D - Exploring high-resolution atom probe microscopy

MS-1. Nanoobjects and engineered nanostructures, catalytic materials

[Poster] MS-1-P-6137 Sb-Te films: crystallized microstructures and "transrotation" examined by TEM

MS-3. Thin films, coatings and surfaces

[Poster] MS-3-P-6128 TEM study of Epitaxial SrIrO₃ Thin Films Grown by Pulsed Laser Deposition Technique

MS-4. Metals, alloys and metal matrix composites

[Poster] MS-4-P-6120 Microstructure Evolution in the Corrosion of Steel Alloys

MS-6. Polymers and organic materials

[Poster] MS-6-P-6092 TEM of Layered Silicate Nanocomposites Based on Polyamide-6

MS-8. Semiconductors and materials for information technologies

[Poster] MS-8-P-6133 Metal Oxide Semiconductor Capacitor fabricated by Electron Beam Induced Deposition

MS-9. Defects in materials and phase transformations

[Poster] MS-9-P-6131 On the complex superstructural ordering of oxygen absorption-desorption in the system BaFeO_{3-δ}, $0 \leq \delta \leq 0.5$

[Poster] MS-9-P-6134 TEM of radiation damage in ferritics: role of image forces

MS-10. Porous and architected materials

[Poster] MS-10-P-6107 Mesoporous zeolite Y studied by rotation electron diffraction and electron tomography

MS-12. Magnetic, superconducting, ferroelectric and multiferroic materials

[Poster] MS-12-P-6114 Scanning electron microscopy and energy dispersive spectroscopy to study the nanomagnetism in minerals

MS-14. Energy-related materials

[Poster] MS-14-P-6116 Ex-situ TEM analysis on extra capacities of SnO₂ lithium-ion battery anode material

[Poster] MS-14-P-6129 AFM and SEM studies on high fluence, low energy iodine implantation in 6H-SiC

LS-1. Live imaging of cells, tissues and organs

[Poster] LS-1-P-6077 The importance of PTEN-PI3K-AKT Signaling Pathway on Invasive Breast Cancer Cell Lines MDA-MB-231

[Poster] LS-1-P-6103 The involvement of Nitric Oxide in breast cancer pathogenesis. Image based investigation at the resolution of single cell clusters (spheroids)

LS-2. Structure and function of cells and organelles

[Poster] LS-2-P-6117 Multi-protein assemblies underlie the mesoscale organization of the plasma membrane

[Poster] LS-2-P-6118 SEM/FIB of cell-interface in 3D-electrodes

LS-3. Super-resolution localization of molecular targets and macromolecular complexes

[Poster] LS-3-P-6085 3D structured illumination superresolution microscopy (3D-SIM) for studying the synaptonemal complex

[Poster] LS-3-P-6108 3D Super Resolution Microscopy: Multi-plane Imaging

[Poster] LS-3-P-6119 Polarized Emission of CdSe Nanorods to Probe Three-Dimensional Structural Dynamics of Single Molecular Motor Proteins

LS-4. Structure of macromolecules and macromolecular complexes

[Poster] LS-4-P-6130 Structural characterization of Photosystem II supercomplex from Norway spruce indicates a different organization of light-harvesting antenna compared to flowering plants

LS-6. Microbiology and virology

[Poster] LS-6-P-6121 Targeting Buried Features in a Resin-Embedded Mouse Cornea with Correlative X-ray and Electron Microscopy

LS-14. Neuroscience

[Poster] LS-14-P-6123 Time-Dependent Changes Between Immature Neurons Contacting GABAergic Nerve Cells Using Double Immunogold Labeling in Wistar and GAERS rats

ID-5. Nanoparticles: Biomedical applications and bio-safety issues

[Poster] ID-5-P-6111 A closer look at hydrophilic core-shell iron oxide nanoparticles for medical applications

ID-10. Advances in sample preparation techniques

[Poster] ID-10-P-6139 Beam damage of embedding media sections and their investigations by SEM

IT-1. Electron optics and optical elements

Type of presentation: Poster

IT-1-P-6140 Toward holographic approach to spherical aberration correction in STEM

Grillo V.¹, Karimi E.³, Balboni R.⁴, Gazzadi G. C.¹, Frabboni S.¹, Mafakheri E.¹, Boyd R.³

¹CNR-Istituto Nanoscienze, Centro S3, Via G Campi 213/a, I-41125 Modena, Italy, ²CNR-IMEM, Parco delle Scienze 37a, I-43100 Parma, Italy, ³Department of Physics, University of Ottawa, 25 Templeton, Ottawa, Ontario, K1N 6N5 Canada, ⁴CNR-IMM Bologna, Via P. Gobetti 101, 40129 Bologna, Italy, ⁵Dipartimento FIM, Università di Modena e Reggio Emilia, Via G. Campi 213/a, 41125 Modena, Italy, ⁶Institute of Optics, University of Rochester, Rochester, New York 14627, USA

Email of the presenting author: vincenzo.grillo@unimore.it

The introduction of the holographic plate has allowed unprecedented control over the phase of the electron wavefront in a microscope. Beyond the early application to electron vortex beams we describe the improvements toward the realization of an efficient compensator for spherical aberration in STEM. The hologram replaces one the condenser apertures and the formed probe can be scanned directly on the sample.

We assumed a fixed spherical aberration C_s coefficient equal to 1.2 mm (for our FEI Technai) , and created an hologram with phase

$$\varphi = kx - 2\pi/\lambda(0.25 C_s (x^2 + y^2)^2 - 0.5 \Delta f (x^2 + y^2))$$

With x, y are Cartesian coordinates, and appropriately scaled so that a distance of 50um corresponds to an inclined ray of 9mrad in the probe plane. Here λ is the electron wavefunction (at 200Kev), k is the grating modulation frequency and Δf is an additional defocus that has been added in the hologram. The addition of this term determines a compensation of the oscillation at high angle in the phase φ due to spherical aberration, this makes the technological realization of the hologram more feasible and has been set to around 110nm underfocus.

The generated hologram profile was obtained by calculating the depth of excavation as

$$T = s \cdot \text{Mod}(\varphi, 2\pi)$$

where s is a scaling constant and the function $\text{Mod}(m, n)$ is the remainder on division of m by n .

Unfortunately the fabricated profile was imperfect and we observe non negligible intensity on all orders of diffraction from the hologram.

Fig 1a and b are the projected and the fabricated hologram, while fig 1c shows the resulting probes where the most intense is the first order diffraction.

REFERENCES

- [1] J. Verbeeck *et al.* Nature **467**, 301 (2010).
- [2] B. J. McMorran *et al.* Science **331**, 192 (2011).
- [3] V. Grillo *et al.* Appl. Phys. Lett. **104**, 043109 (2014).

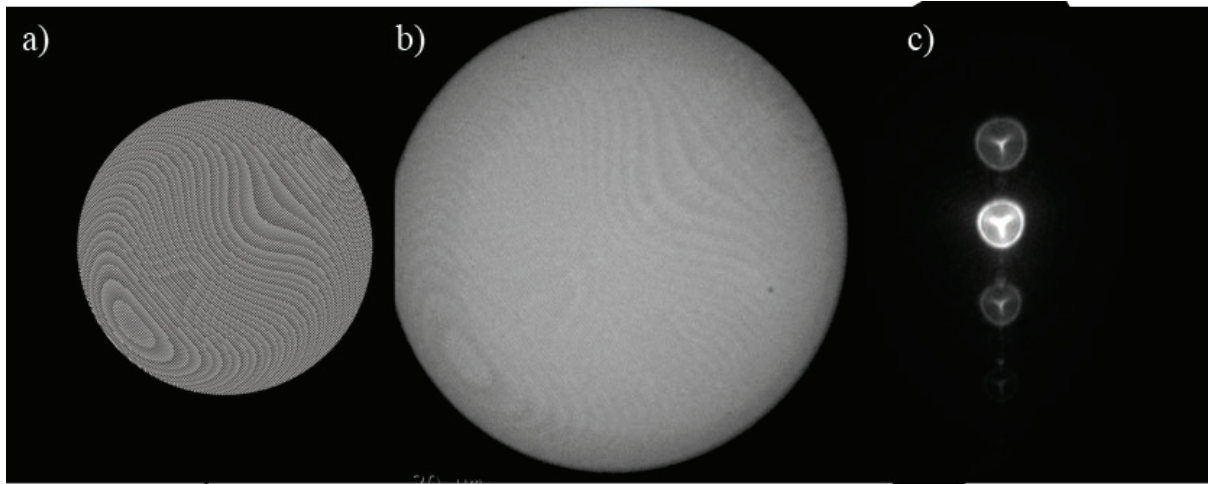


Fig. 1: Fig1 (a) Numerically simulated and (b) fabricated effective hologram (TEM image) of the holographic aberration corrector. (c)Image of the beam diffracted by the hologram highlighting the uncorrected 3-fold astigmatism

IT-3. Super-resolution light microscopy and nanoscopy imaging

Type of presentation: Poster

IT-3-P-6078 Beyond Electron Microscopy with Super-Resolution Nanoscopy in Soft Matter

King J. T.¹, Granick S.¹

¹University of Illinois, Urbana-Champaign

Email of the presenting author: jtking@illinois.edu

Abstract

Electron microscopy traditionally leads optical microscopy considering the diffraction limit, yet optical microscopy has the appeal of studying dynamics of soft complex systems in situ. In these systems, however, the structures and dynamics of interest are often on the nanoscale, well below the diffraction limit. The desire to open all complex systems to the world of imaging has inspired the development of super-resolution techniques capable of spatial resolutions down to the nanometer length scale. While this new technology has already been harnessed by the imaging community to study frozen structures, there remains great potential in the adaptation of these techniques to dynamic systems.

In particular, sub-diffraction microscopy techniques based on stimulated emission depletion (STED) enable the routine achievement of spatial resolution on the order of tens of nanometers without sacrificing time-resolution, lending itself particularly well to dynamic studies. STED nanoscopy relies on exciting a diffraction-limited volume of chromophores, but then selectively turning off portions of the ensemble with a spatially shaped beam that drives stimulated emission. By overlapping a doughnut-shaped depletion beam, tuned to the emission wavelength of the chromophores, with the excitation beam, molecules situated in the high intensity ring of the doughnut are depleted, leaving only molecules in the diffraction-unlimited doughnut hole to be detected.

To this end, we are working to adapt STED imaging to a variety of dynamic measurements, including fluorescence correlation spectroscopy (FCS), dynamic anisotropy, and time-resolved spectroscopic imaging. Previously, in work by others, STED nanoscopy largely focused on biological systems. We focus instead on nanoscale dynamics of materials systems. This presentation will demonstrate the benefits of such experimental capabilities in a diverse range of complex systems, ranging from nanoscale segmental diffusion of polymer systems to super-resolution spectroscopic imaging of polymer films under stress.

Acknowledgement: This work was supported by DOE Award No. DE-FG02-07ER46471.

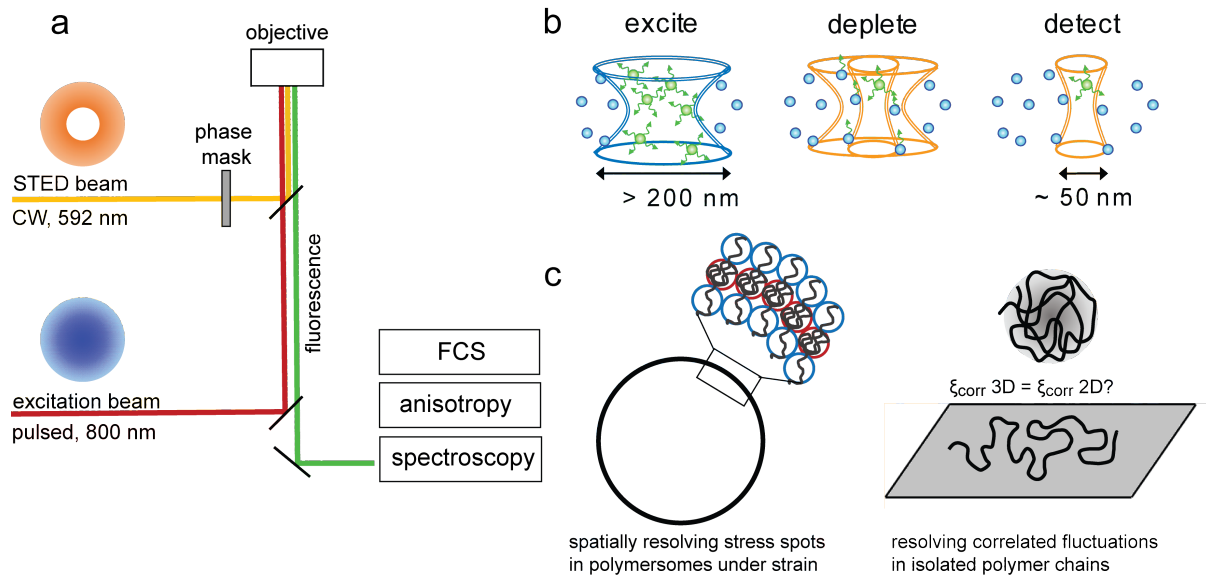


Fig. 1: Figure 1. (a) Experimental setup of STED nanoscopy, showing the excitation scheme coupled to several different observables. (b) Principle of stimulated depletion using spatially shaped depletion beams. (c) Examples of systems being studied: nonequilibrium dynamics of polymersomes and internal dynamics of polymer chains in various environments.

IT-4. Scanning electron microscopy

Type of presentation: Poster

IT-4-P-6101 Direct-write chlorine based etching of semiconductor devices utilizing a SEM

Gökdeniz Z. G.¹, Shawrav M. M.¹, Wanzenboeck H. D.¹, Mika J.¹, Bassem I.¹, Zeiner C.¹, Lugstein A.¹, Bertagnolli E.¹

¹Vienna University of Technology, Vienna, Austria

Email of the presenting author: zeynep.goekdeniz@tuwien.ac.at

Focused electron beam induced etching (FEBIE) is a direct-writing technique where an electron beam is utilized to etch away material with the help of precursor molecules. This is a mask-free, resist-free method which can be performed inside a Scanning Electron Microscope in a single process step. Recently, this technique has got increasing attention due to its nanometer precision.

Semiconductor nanowires are promising candidates for future nanoelectronics devices. Among various nanowire types, Si-NWs and Ge-NWs have potential for innovative sensor ideas and various photovoltaics applications. The custom-designed modification of optical and electrical behavior of nanowires is essential for developing new type of devices. However, it is a real challenge to tune the properties of specific nanowire on a surface.

Introducing chlorine as etch gas in FEBIE can be a novel method to tune the properties of these nanowires. It eludes some of the major drawbacks of the ion beam induced etching process. In this work, we will report on the alteration of geometrical changes and the electric properties of Si-NWs and Ge-NWs. The effect of different parameters such as pixel spacing, dwell time etc. involved on the etch process will be thoroughly investigated. The impact of chlorine flux on the etch process will also be determined. The HRSEM and HRTEM results will be shown to prove the tuned geometry of the Ge-NWs. A Raman spectroscopy technique have been used to show the status of the nanowire before and after FEBIE process.

Acknowledgement: Austrian Science Fund (FWF) - P24093

Center for Micro- and Nanostructures (ZMNS)

University Service Centre for Transmission Electron Microscopy (USTEM)

Austrian Society for Electron Microscopy (ASEM)

Type of presentation: Poster

IT-4-P-6105 New opportunities for biomedical research in the Saint-Petersburg State University

Vorobev M.¹

¹Saint-Petersburg State University, Saint-Petersburg, Russian Federation

Email of the presenting author: vorobiev.maxim@rambler.ru

New opportunities for biomedical research in the Saint-Petersburg State University

The Research Resource Center for Molecular and Cell Technologies was recently established in Saint-Petersburg State University. The Center is aimed at carrying out research projects in the field of life sciences and biomedicine. Unique biomedical analytical instruments and all kinds of routine equipment for sample preparation along with up-to-date technologies provided in the Center allow to solve complex tasks while investigating both fixed and living biological specimen. The Center offers confocal microscopy, including true scanning, spinning disk and super resolution (STED-CW) confocal microscopy; wide field microscopy; quantitative FRET microscopy in combination with FLIM and FCS. Transmission electron microscopy, cryo TEM, tomography and cryo tomography, plunge freezing, cryosectioning, immunostaining, freeze substitution and low temperature embedding. Scanning electron microscopy, energy-dispersive X-ray spectroscopy, high pressure freezeeng for freze fracture and cryo SEM analysis.

The data obtained can be analyzed using various image processing software packages allowing image visualization, morphometric and deconvolution analyses of all microscopic images, processing of time-lapses, multi-channel imaging and 3D-imaging.

An additional tool for complex biomedical investigations is presented by the molecular histology and cell science techniques. The Center provides unique equipment for laser microdissection, cell analyzing and sorting, and histological visualization using MALDI-imaging. Highly qualified specialists support users with the integral methodological base starting with the help in development of the experimental design of the scientific research projects and finishing with the processing of the results obtained. The Center is open for international cooperation with researchers and companies from all over the world.

Type of presentation: Poster

IT-4-P-6135 airSEM™, high resolution SEM operating in open air, a new approach for correlative imaging of hydrated samples

Addadi S.¹, Milstein Y.¹, de Picciotto R.¹, Shachal D.¹

¹B-nano Ltd. Rehovot 76326, Israel. www.b-nano.com

Email of the presenting author: dubi_shachal@b-nano.com

airSEM™ technology enables high resolution SEM imaging of an object residing in ambient conditions. The airSEM™ represents a new approach to electron microscopy, allowing to image objects close to their natural state and simplifying the integration of multiple imaging techniques on a single imaging platform.

The technology addresses two of the main challenges associated with vacuum SEM imaging of life science samples:

a. Having the sample in its hydrated state; thus preserving both chemical and structural information, which might be lost when using conventional sample preparation protocols appropriate for vacuum SEM. airSEM™ surpasses the steps of fixation, dehydration, drying or coating which in many cases alter the chemistry of the sample and its structure and may introduce artifacts.

b. Cross correlating data from different modalities which are commonly situated on different platforms. In addition, the airSEM™ allows to substantially shorten the time needed to extract data and reduces the probability for sample contamination or damage.

In order to demonstrate these advantages, two representative case studies are presented:

1. Correlative fluorescence SEM imaging of lung extracellular matrix: Collagen type I is specifically localized by direct correlative imaging of immunofluorescence and SEM tissue morphology.

2. Calcium uptake in sea urchin embryos: Fluorescently labelled mineral is specifically localized, in fully hydrated minimally processed sea urchin embryo section, by correlation to the SEM image. Calcium mapping (by EDX) of the sample shows complete match to the correlated area.

Acknowledgement: N. Vidavsky, L. Addadi, S. Weiner Dep. of Structural Biology and I. Solomonov, D. Talmi-Frank, I. Sagi, Dep. of Biological Regulation Weizmann Institute of Science, Rehovot Israel.

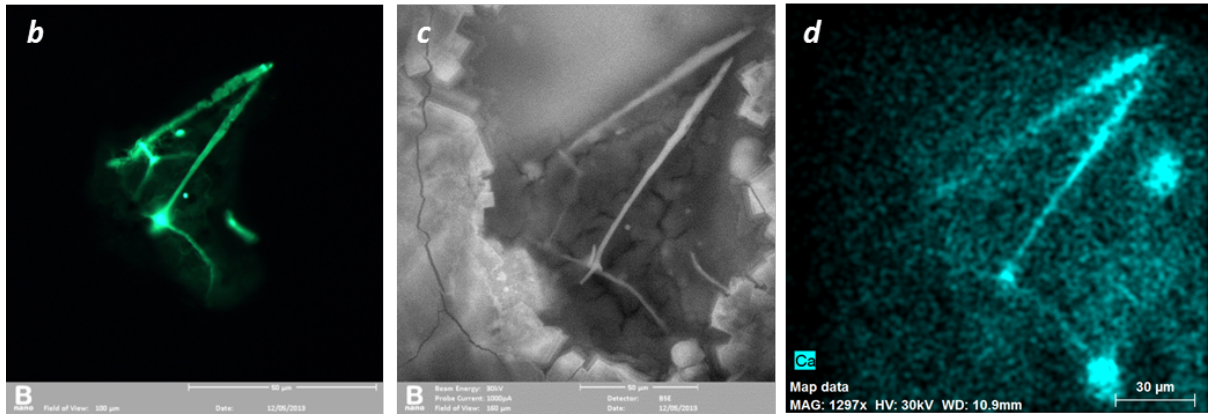


Fig. 1: Chemical and structural correlative information of hydrated samples. (a) airSEM™ imaging station showing the optical microscope, airSEM™, translation stage and sample holder (b) Calcein fluorescence image of embryo vibratome slice embedded in gel. (c) airSEM™ BSE image. (d) EDX map of the same region as (b).

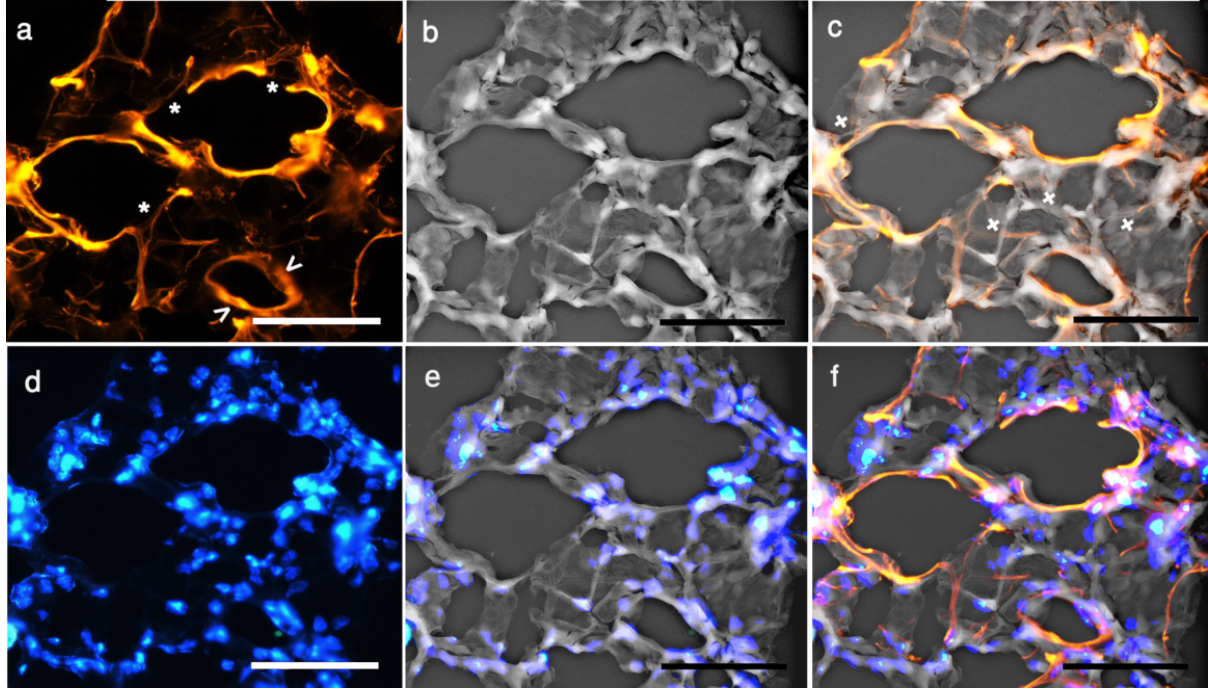


Fig. 2: Structural and functional correlative imaging of fresh tissue samples. (a) Fresh frozen cryo-sectioned lung slice labeled with anti collagen type I- Cy3. (b) airSEM™ BSE image. (d) Cell nuclei (DAPI). (c,e) Overlay of b with a and d respectively. (f) Overlay of all channels (a,b,d). Scale bar: 50 μ m.

Type of presentation: Poster

IT-4-P-6136 airSEM™ : Enabling EDX material analysis in open air

Milstein Y.¹, de Picciotto R.¹, Brami Y.¹, Shachal D.¹

¹B-nano Ltd. Rehovot 76326, Israel. www.b-nano.com

Email of the presenting author: dubi_shachal@b-nano.com

airSEM™ is an innovative scanning electron microscope which sidesteps the main obstacles stemming from the need for vacuum as a prerequisite for capture of high-resolution images. The technology overcomes fundamental electron beam imaging related challenges, such as scattering of electrons by gas molecules and efficient signal collection, leading to a resolution of 5nm under ambient conditions.

The airSEM™ represents a new approach to electron microscopy, enabling to image objects close to their natural state and simplifying the integration of multiple imaging techniques on a single imaging platform.

This technology facilitates the employment of electron-beam related analysis techniques in full atmospheric pressure, a possibility which have been limited to a vacuum environment thus far. One of these opportunities is performing EDX analysis at ambient conditions.

The advantages of using EDX in airSEM™ are manifold; First, performing analysis on samples which are not vacuum compatible becomes possible. Second, since operating in air suppresses sample charging, it removes the necessity to coat insulating samples which may interfere with quantitative analysis. Third, material analysis of large substrates, for example panels in the FPD industry becomes simple without the need to construct a large vacuum chamber to accommodate the sample. Finally, EDX may be incorporated as one of the modalities in the airSEM™ imaging station enabling one stop imaging and analysis.

This study focuses on the characterization of EDX performance in airSEM™. We show that the basic features, such as count rate, sensitivity and ability to analyze low Z materials down to Boron, are preserved. EDX Spectra and maps taken from representative samples are shown.

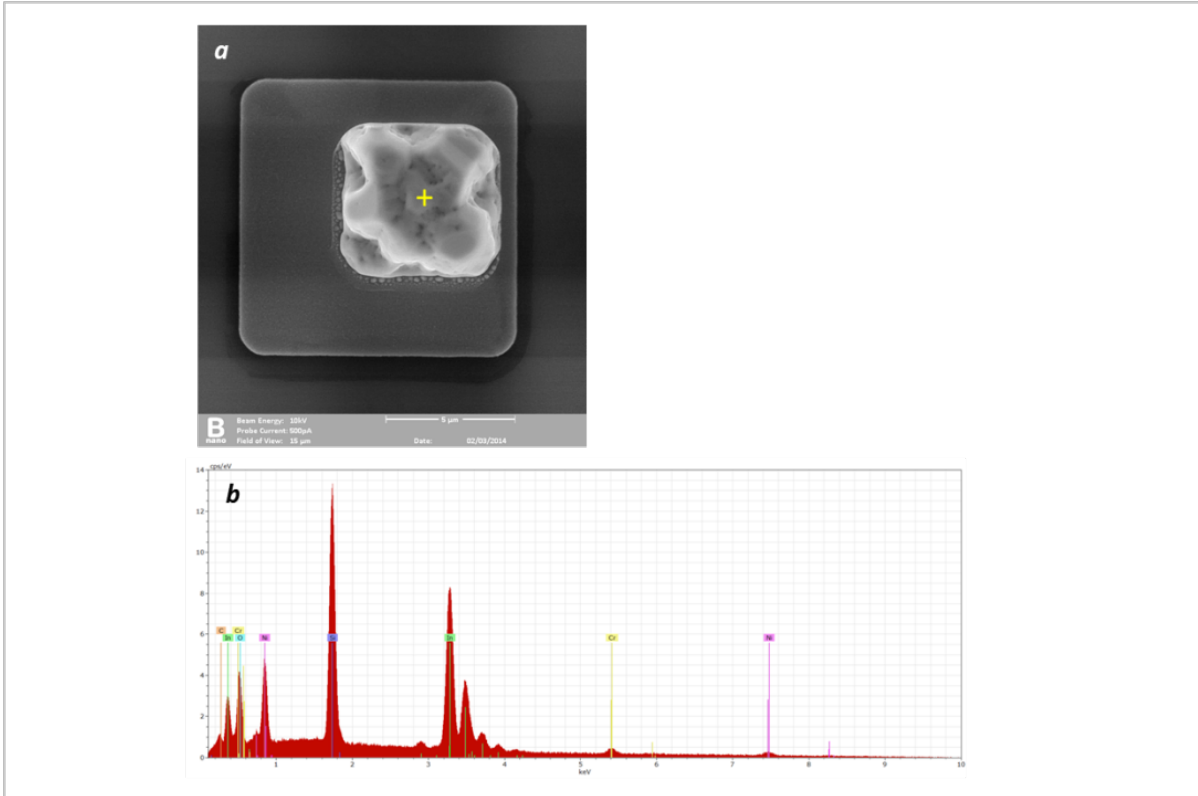


Fig. 1: Imaging and material analysis of an Indium bump taken in open air. (a) airSEM™ image (b) EDX spectrum taken in the marked location of (a). Imaging conditions: Beam energy 10keV, Beam current 500pA.

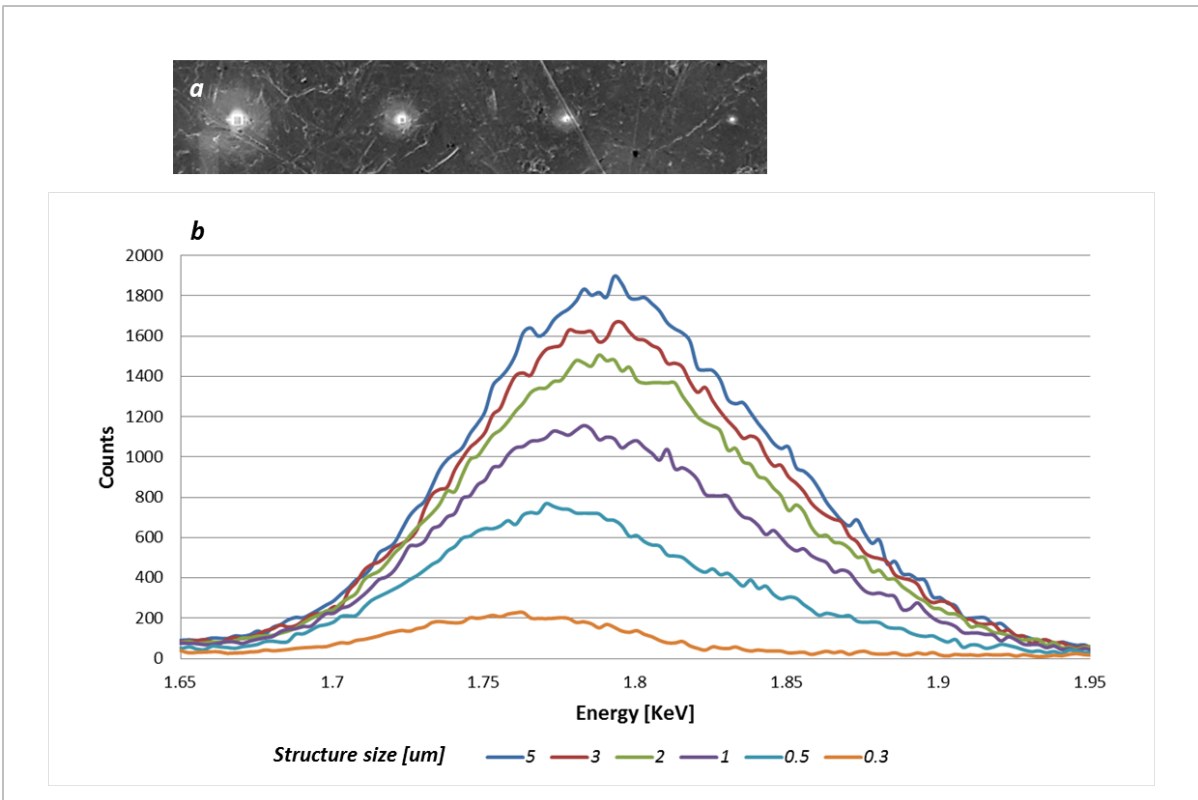


Fig. 2: EDX detection sensitivity in open air. (a) SEM image of some of the W FIB depositions used for sensitivity characterization. (b) EDX data showing the effect of structure size on peak intensity. Imaging conditions: Beam energy 30keV, Beam current 500pA.

Type of presentation: Poster

IT-4-P-6138 airSTEM: high resolution STEM detection in open air

Milstein Y.¹, Brami Y.¹, de Picciotto R.¹, Shachal D.¹

¹B-nano Ltd. Rehovot 76326, Israel. www.b-nano.com

Email of the presenting author: dubi_shachal@b-nano.com

airSEM™ is an innovative scanning electron microscope which sidesteps the main obstacles stemming from the need for vacuum as a prerequisite for capture of high-resolution images.

The technology overcomes fundamental electron beam imaging related challenges, such as scattering of electrons by gas molecules and efficient signal collection, leading to a resolution better than 5nm under ambient conditions.

The airSEM™ represents a new approach to electron microscopy, enabling to image objects close to their natural state and simplifying the integration of multiple imaging techniques on a single imaging platform.

Having STEM detection capability in open air addresses several challenges associated with vacuum STEM: a. Imaging samples which are not vacuum compatible in particular hydrated samples. b. Cross correlating data from different modalities which are commonly situated on different platforms. In addition operating in air simplifies operation and significantly reduces the time for data acquisition.

This study focuses on the characterization of STEM performance in airSEM™, in particular measuring the scattering angle of transmitted electron in air. The angles were measured for two SiN membranes of different thickness and at different distances separating the scattering membrane and the detector.

The data shows that mass thickness contrast is preserved despite the scattering of electrons by the air molecules. Images of biological cross sections, organic and inorganic particles taken with airSTEM detector both in bright field and dark field modes are shown.

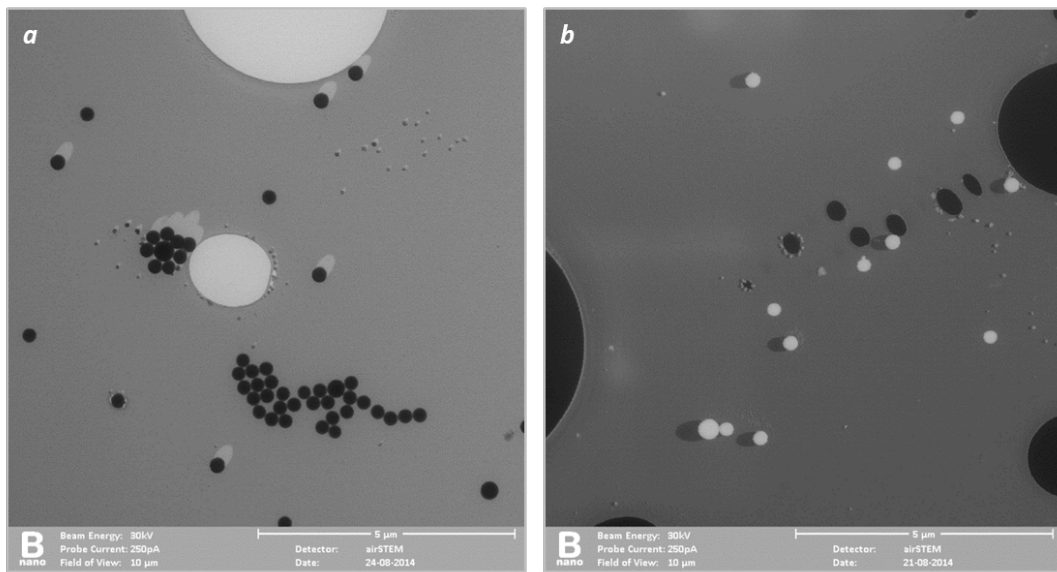


Fig. 1: 300nm Polystyrene latex on Formvar/Carbon film. (a) airSTEM Bright field mode (b) airSTEM Dark field mode

IT-7. In-situ microscopic techniques and cryo-microscopies

Type of presentation: Poster

IT-7-P-6125 Beyond Current SEM - AFM Solutions: A Highly Flexible in-situ AFM for Correlated Microscopy in Micromechanical Testing

Cordill M. J.¹, Kreith J.¹, Winkler R.², Hofer F.^{2,5}, Fantner G. E.³, Strunz T.⁴, Erickson B.⁴, Fantner E. J.⁴, Plank H.⁵

¹Erich Schmid Institute of Materials Science and Dept. Material Physics, Montanuniversität Leoben, Austria, ²Centre for Electron Microscopy, Graz, Austria, ³École Polytechnique Fédérale de Lausanne, School of Engineering, Interfaculty Institute of Bioengineering, Lausanne, Switzerland, ⁴GETec, Langenlois, Austria, ⁵Institute for Electron Microscopy and Nanoanalysis, Graz University of Technology, Graz, Austria

Email of the presenting author: harald.plank@felmi-zfe.at

The advent of integrated atomic force microscopes (AFMs) in stand-alone scanning electron microscopes (SEMs) opened new possibilities due to quantitative 3D information even on complex surface morphologies. This does not only reduce turnaround times but also expanded the information for both techniques character in a comprehensive manner due to the quasi-simultaneous correlation within one setup. One example in material science is the investigation of slip steps structures and its correlation to the active dislocation sources after nano-indentation of metallic single crystals. The collective density of dislocations and the formation of spatially complex dislocation structures have been studied with a combined AFM and SEM (AFSEM™, GE-Tec, Austria). This system uses a highly flexible, *in-situ* tip scanning system with a wide range of scan-head modules according to customer demands. While the SEM acts as the high resolution navigation tool and can provide structural information via electron backscatter diffraction (EBSD) analyses, the integrated AFM solution provides laterally resolved, quantitative step height information with nm and even sub-nm resolution in XY and Z, respectively. This is an enormous advantage as it is very complicated to distinguish between real surface features on the lower nanoscale and coverage layers via SEM due to the electron beam penetration depth. By that, both techniques are complemented by each other in a straightforward manner providing comprehensive insights practically impossible or extremely complicated via individual technique or two separate instruments, respectively.

Type of presentation: Poster

IT-7-P-6127 In situ observations of confined platinum nanoparticles coalescing within carbon nanotubes

Cichocka M. O.^{1,2,3,5,9}, Zhao J.², Bachmatiuk A.^{2,3,4,5}, Quang H. T.^{2,3}, Gorantla S. M.⁵, Gonzalez-Martinez I. G.^{5,6}, Eckert J.^{5,6}, Fu L.⁷, Warner J. H.⁸, Rummeli M. H.^{2,3,10}

¹Department of Materials and Environmental Chemistry, Stockholm University, SE-106 91 Stockholm, Sweden, ²IBS Center for Integrated Nanostructure Physics, Institute for Basic Science (IBS), Daejeon 305-701, Republic of Korea, ³Department of Energy Science, Department of Physics, Sungkyunkwan University, Suwon 440-746, Republic of Korea, ⁴Center of Polymer and Carbon Materials, Polish Academy of Sciences, M. Curie-Sklodowskiej 34, Zabrze 41-819, Poland, ⁵IFW Dresden, Institute of Complex Materials, P.O. Box 270116, D-01171 Dresden, Germany, ⁶Technical University (TU) Dresden, Institute of Materials Science, D-01062 Dresden, Germany, ⁷College of Chemistry and Molecular Science, Wuhan University, 430072, China, ⁸Department of Materials, University of Oxford, 16 Park Road, Oxford OX1 3PH, United Kingdom, ⁹M O Cichocka was formerly at affiliations 2,3 and 5 were this all this work was conducted., ¹⁰corresponding author: email:mark@rummeli.com

Email of the presenting author: cichocka.mg@gmail.com

Carbon nanotubes (CNT) in which the core is filled with a metal are receiving increased attention due to their potential application in catalysis [1], and electronic devices [2]. Moreover, the structural and chemical properties of metals inside CNT can be different as compared to their bulk counterparts. For example, metal residing inside CNT usually show enhanced catalytic performance than CNT decorated with metal nanoparticles [3]. In the specific case of platinum filled CNT (Pt@CNT) they can show higher hydrogenation activity, enantioselectivity and average turnover frequency than CNT with surfaces decorated with Pt NPs.

When using nanoparticles for catalytic purposes it is crucial to stabilize the nanoparticles, because coalescence is the main cause of their catalytic deactivation. The details of these processes in a confined environment, for example, inside a CNT have not yet been explored. This work focuses on an in-situ study of Pt nanoparticles inside carbon nanotubes using Cs aberration corrected TEM with an acceleration voltage of 80 kV. The confined environment of the CNT restricts the freedom of movement for the Pt nanoparticles compared to non-confined reactions. The study shows the various processes during coalescence of Pt nanoparticles which can occur via particle reorientation, relaxation and direct attachment of atoms on the surface. In addition, we find many Pt nanoparticles have their (111) plane parallel to the tube wall which might suggest preferential alignment.

Acknowledgement:

1 P Serp, E. Castillejos, ChemCatChem, 2010, 2, 41-47;

2 D. Golberg, P.M.F.J. Costa, M. Mitome, S. Hampel, D. Haase, Ch. Mueller, A. Leonhardt, Y. Bando, Adv. Mater., 2007, 19, 1937-1942;

3 C. Mateo-Mateo, C. Vazquez-Vazquez, M. Perez-Lorezno, V. Salgueirino, M.A. Correa-Duarte, Journal of Nanomaterials, 2012, 2012, 6 pages.

IT-8. Ultrafast and high-throughput microscopies

Type of presentation: Poster

IT-8-P-6102 Development of femtosecond time-resolved relativistic-energy electron microscopy

Yang J.¹, Tanimura K.¹, Yoshida Y.¹, Urakawa J.²

¹The Institute of Scientific and Industrial Research, Osaka University, Japan, ²High Energy Accelerator Research Organization, Japan

Email of the presenting author: yang@sanken.osaka-u.ac.jp

The direct visualization of structural dynamic processes in matter occurring on femtosecond time scales over sub-nanometer (even atomic) spatial dimensions has long been a goal in scientists. Transmission electron microscopy (TEM) is a powerful tool to observe directly the image from specimen with high spatial resolution. When coupled with time resolution, it, which also called ultrafast electron microscopy (UEM), would be the strongest tool for the study of ultrafast dynamics in materials. Currently, the UEM with the time-spatial resolution of nanosecond and nanometer has been achieved in conventional TEM through the use of photo-activated electron source driven by a nanosecond laser in the non-space-charge-limited regime with ns-long pulse length. A large number of important phenomena, i.e. phase transformations, melting, resolidification, nucleation and growth of damage in nanosecond time region, have been investigated. To achieve a high time resolution overcoming the space-charge limitation, we have proposed and designed a femtosecond time-resolved relativistic-energy electron microscopy using a photocathode radio-frequency (RF) electron gun. In 2009, we have developed a new RF gun to generate a low-emittance femtosecond-bunch electron beam: 100 fs and 0.2 mm-mrad, which are essential for the achievement of nm-fs space-time resolution in future. In 2010, we constructed successfully an instrument of ultrafast relativistic-energy electron diffraction (UED) using the RF gun. The time resolution of 100 fs has been achieved. A first prototype of RF gun based relativistic-energy TEM has been constructed at Osaka University in 2012. Both the static measurements of both relativistic-energy electron diffraction and image have been succeeded in the prototype. In this poster, the activities on UED and UEM are introduced. The requirements and limitations of the beam parameters in UEM are reviewed. The concept and design of RF gun based relativistic-energy TEM prototype are reported. The beam dynamics and challenges in femtosecond RF gun will be discussed. Finally, some demonstrations of the relativistic-energy TEM images, the single-shot and time-resolved UED measurements are reported.

Acknowledgement: This work was supported by JSPS KAKENHI Grant Numbers 21226022, 26246026.



Fig. 1: The first prototype of femtosecond time-resolved relativistic-energy TEM using a photocathode RF gun.

Type of presentation: Poster

IT-8-P-6122 High-Throughput Characterization of Nanoparticles by TEM

Dufresne C.¹, Ivanov-Pankov S.¹, Weigel W.¹, Bared G.¹

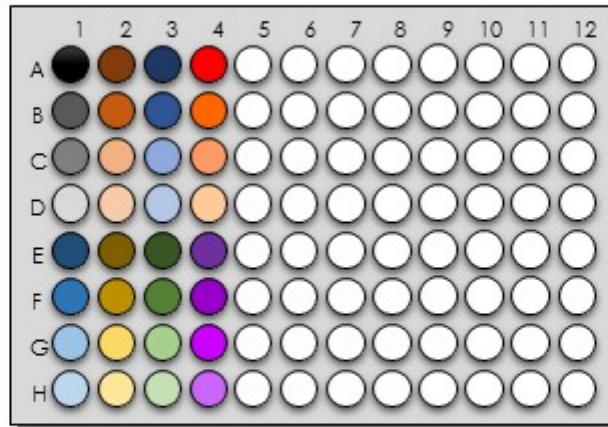
¹Scienion AG, Berlin, Germany

Email of the presenting author: dufresne@scienion.com

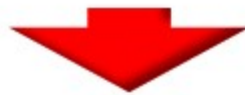
Analysis of nanoparticles by TEM is a very useful characterization method. However, by nature of TEM instrument design placing sample grids under high vacuum, the number of samples that can be looked at in a given time period is very limited. Indeed, for each sample placed on a TEM grid, the TEM has to undergo a complete cycle of losing and re-establishing vacuum conditions. Having the capability to insert multiple samples at once inside the TEM and then acquiring all images without breaking vacuum for each one, would result in a tremendous increase in the number of samples that can be analyzed per hour.

For over 10 years, SCIENION's picoliter liquid dispensing technology has been used to deposit arrays of different sample solutions onto a wide variety of substrates. Applying this well-proven technology to dispense multiple liquid samples onto a single TEM grid is an obvious extension. In this poster, we illustrate the process by which one can deposit up to 100 different samples onto a single 3 mm TEM grid's 1 x 1 mm window. In summary, analytical suspensions of nanoparticles are loaded in the instrument using a 96-well plate. For each sample, the instrument aspirates a small aliquot of a few microliters, and dispenses 50-100 picoliters onto a precise, indexed location inside the TEM window. The process is repeated until all samples have been deposited inside the grid in different locations. The most suitable TEM windows have to be selected according to the nature of the nanoparticles to be investigated. The hydrophilicity of the window material is important to allow high quality spot formation as well as homogeneous distribution of the nanoparticles inside each spot.

Acknowledgement: Thanks to Dr.-Ing. Werner Österle, from BAM (Federal Institute for Materials Research and Testing) in Berlin.



Standard 96-well microtiter plate shown with 32 different sample suspensions or solutions



32 different samples deposited into a single 3 mm TEM Grid

Fig. 1: Representation of 32 unique samples transferred from a microtiter plate into a single TEM grid window

IT-10. Electron tomography

Type of presentation: Poster

IT-10-P-6113 On resolution in electron tomography of beam sensitive materials

Chen D. L.¹, Goris B.², Bleichrodt F.³, Heidari Mezerji H.², Bals S.², Batenburg K. J.³, de With G.¹, Friedrich H.¹

¹Laboratory of Materials and Interface Chemistry, Eindhoven University of Technology, Netherlands, ²EMAT, University of Antwerp, Belgium, ³Centrum Wiskunde & Informatica, Amsterdam, Netherlands

Email of the presenting author: d.chen@tue.nl

Electron tomography (ET) is nowadays frequently utilized in materials science to reveal 3D morphology of functional nanostructures such as e.g. organic solar cells. However, obtaining 3D quantitative information from organic samples is hampered by the low reconstruction quality which is dominated by the beam sensitivity of the specimen. Additionally, limited tilt range, angular sampling, and artifacts introduced by the reconstruction algorithms also play important roles. Therefore the fidelity of 3D reconstruction is not only determined by one individual factor but is the combination of all the aforementioned factors. To develop smart 3D imaging strategies in ET, this combined effect should be addressed. In this work, we simulate the entire ET workflow starting with a well-defined model system, over calculating tilt series to reconstructing the 3D morphology, ending with qualitative and quantitative comparisons (Fig 1).[1,2] To provide a direct link to the attainable resolution, edge profiles which characterize the transition between different materials are analyzed locally and globally by fitting of an edge spread function and comparing with the ground truth of the model. First, we systematically studied the influence of electron doses, tilt ranges, and angular sampling on the reconstruction quality by WBP (Fig. 2).[1] Results show the reconstruction quality increases with an increasing total electron dose, and also with an increasing maximum tilt range. For the studied specimen, isotropic resolution is realized at a tilt range of $\pm 75^\circ$, regardless of electron dose and tilt increments, which can be considered optimal for subsequent quantification. We find that using large tilt increments at low electron doses, the reconstruction quality is preserved or even improved, which is counterintuitive to Crowther's sampling based resolution estimate. Furthermore, we investigated the properties of SIRT, TVM, and DART reconstruction algorithms with respect to electron doses and angular sampling schemes (Fig. 3).[2] Results show SIRT algorithm is the most stable method and insensitive to changes in angular sampling, thus it is suited for materials of any beam sensitivity or changing experimental conditions. TVM algorithm reduces noise and sharpens edges, but edge positions are strongly influenced by the chosen tilt scheme and objects become thinned. DART algorithm provides a segmented reconstruction and significantly reduces elongation artifacts along the beam direction which is a clear advantage for quantification. Finally, no advantage of TVM and DART to deal better with fewer projections was observed.

References:

[1] D.L. Chen, et al., J. Phys. Chem. C, 118 (2014) 1248-1257.

[2] D.L. Chen, et al., Ultramicroscopy (2014) DOI: 10.1016/j.ultramic.2014.08.005

Acknowledgement: This research forms part of the research program of the Dutch Polymer Institute (DPI), projects #615. This work is supported by the Research Foundation Flanders (FWO Vlaanderen) through a Ph.D research grant to B.G.

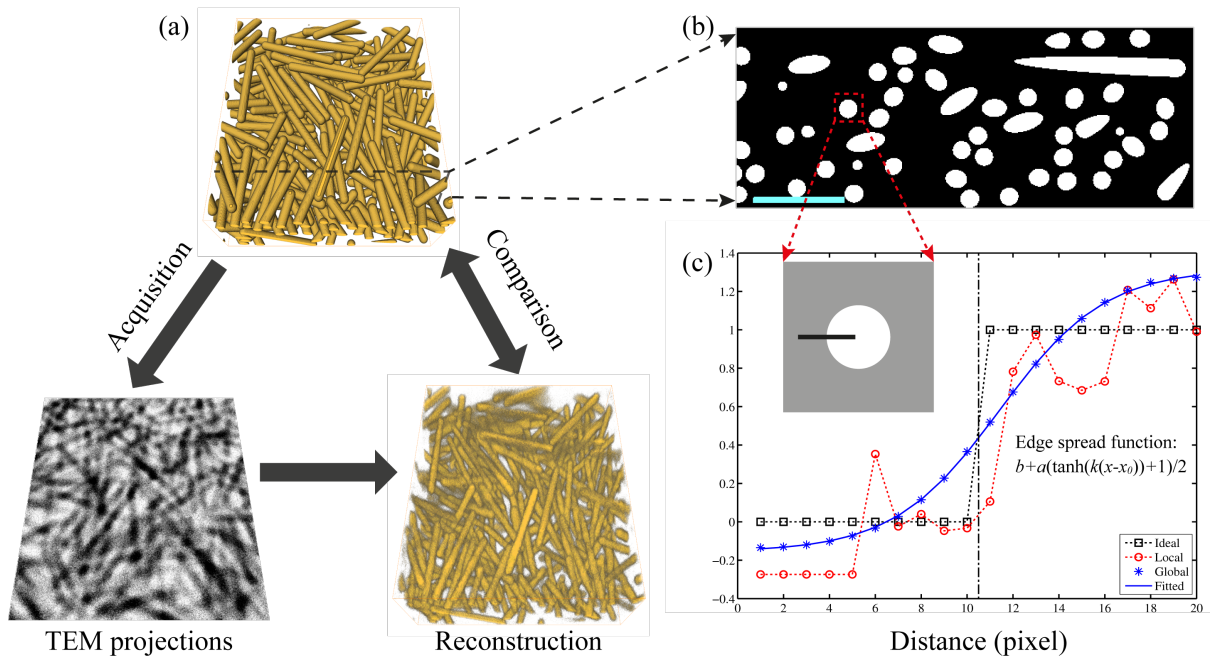


Fig. 1: (a) Flowchart of the simulation approach. (b) and (c) Illustration of the edge intensity profile which is taken across the background-object edge.

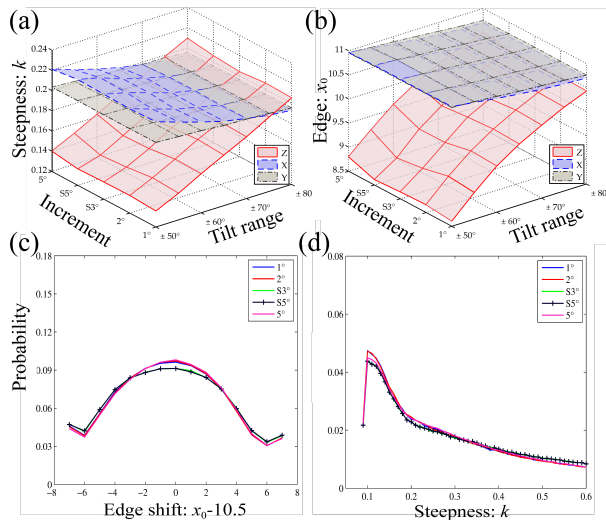


Fig. 2: Steepness k (a) and edge position x_0 (b) of global edge intensity profiles along X (blue), Y (grey), and Z (red) directions for various acquisition schemes at a total electron dose $10^4 \text{ e}/\text{\AA}^2$. Probability density distribution of edge shift Δx_0 (c) and steepness k (d) along the beam direction Z for various tilt increments at 10^4 and $\pm 75^\circ$.

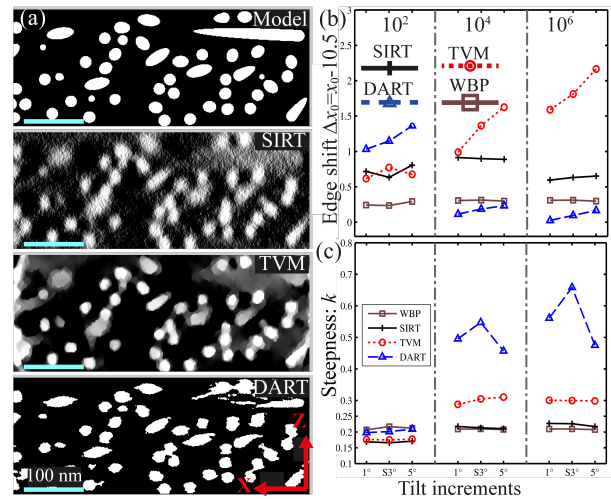


Fig. 3: (a) An XZ numerical cross-section through the model, SIRT, TVM, and DART reconstruction at 10^4 , 1° tilt increment. Edge shift (b) and steepness (c) of global edge profiles along X direction. S3° and S5° denote the Saxton scheme with an angular starting interval of 3° and 5° .

IT-11. Electron holography and lens-less imaging

Type of presentation: Poster

IT-11-P-6126 Three-wave electron vortex lattices for vortex interferometry

Dwyer C.¹, Boothroyd C. B.¹, Chang S.¹, Dunnin-Borkowski R. E.¹

¹Forschungszentrum Juelich, Juelich, Germany

Email of the presenting author: dwyerch1@gmail.com

Apart from their intrinsic appeal from the perspective of physical optics, vortical electron wavefields may prove very useful for the measurement of nanoscale electromagnetic fields. Vortical wavefields are characterised by points at which the amplitude is zero, and around which the phase of the wavefield winds by some (non-zero) integer multiple of 2π . The method considered here is "electron vortex interferometry", which utilizes a vortex lattice - a wavefield containing a periodic array of vortices and antivortices. An electromagnetic field displaces the vortices, so that the vortex positions encode the slowly-varying phase of the wavefield. Such approaches have been demonstrated in light optics [1, 2]. Compared to most Fourier-space reconstruction schemes, this approach offers the benefit of directly measuring the unwrapped phase, and potentially better spatial resolution by bypassing the requirement of sideband separation.

Here, we have used three plane waves [3] to generate vortex lattices appropriate for electron vortex interferometry. Three plane waves is the minimum number needed to produce vortices. While previous work [4] has employed four plane waves, three plane waves have several advantages: (1) An intensity zero produced by three interfering plane waves is guaranteed to contain a vortex [2, 3]; (2) Under free-space propagation, three-wave vortices trace out straight parallel lines, and they do not exhibit creation or annihilation [3]; (3) The vortices are stable with respect to phase and amplitude perturbations [2]; (4) Three-wave lattices are robust with respect to lens aberrations. A schematic representation of the vortex lattice generated by three non-coplanar plane waves is shown in Fig. 1.

To be useful for electromagnetic field measurements, the generation and interference of the plane waves must be performed in a highly controllable and repeatable way, which can be achieved in a TEM using multiple electron biprisms [5]. Fig. 2 shows the generation of three-wave electron vortex lattices using two biprisms separated by an angle of approximately 60 degrees. We have confirmed the existence of vortices in such wavefields by using a third biprism to measure the phase. This approach enables a relatively simple scheme for producing vortex lattices suitable for electron vortex interferometry.

[1] J. Masajada et al., *Optics Comm.* 207, 85 (2002).

[2] S. A. Eastwood et al., *Optics Express* 20, 13947 (2012).

[3] K. W. Nicholls and J. F. Nye, *J. Phys. A: Math. Gen.* 20, 4673 (1987).

[4] T. Niermann et al., *Ultramicroscopy* 136, 165 (2014).

[5] T. Hirayama et al., *Appl. Phys. Lett.* 67, 1185 (1995).

Acknowledgement: The authors acknowledge the European Commission for an Advanced Grant, and the Deutsche Forschungsgemeinschaft for a Deutsch-Israelische Projektkooperation Grant.

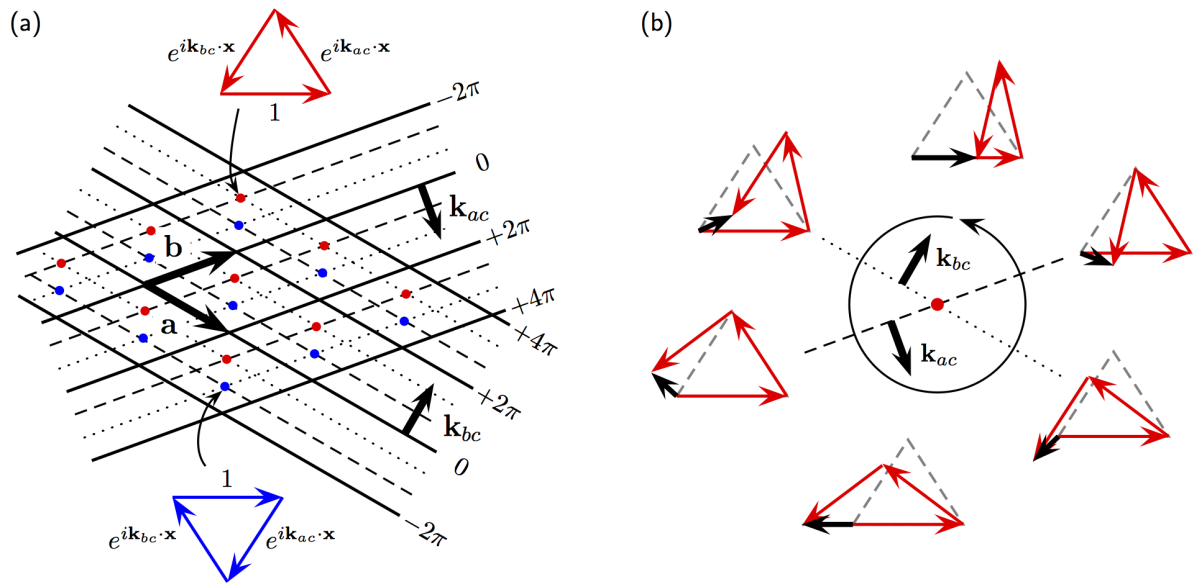


Fig. 1: Schematic of a three-wave vortex lattice. a, The wave function in a plane perpendicular to the optic axis. Vortices and antivortices (red and blue dots, respectively) exist wherever the three phasors form a closed triangle in the complex plane. b, The phasor sum acquires a phase of 2π as an anticlockwise path is traversed around a vortex.

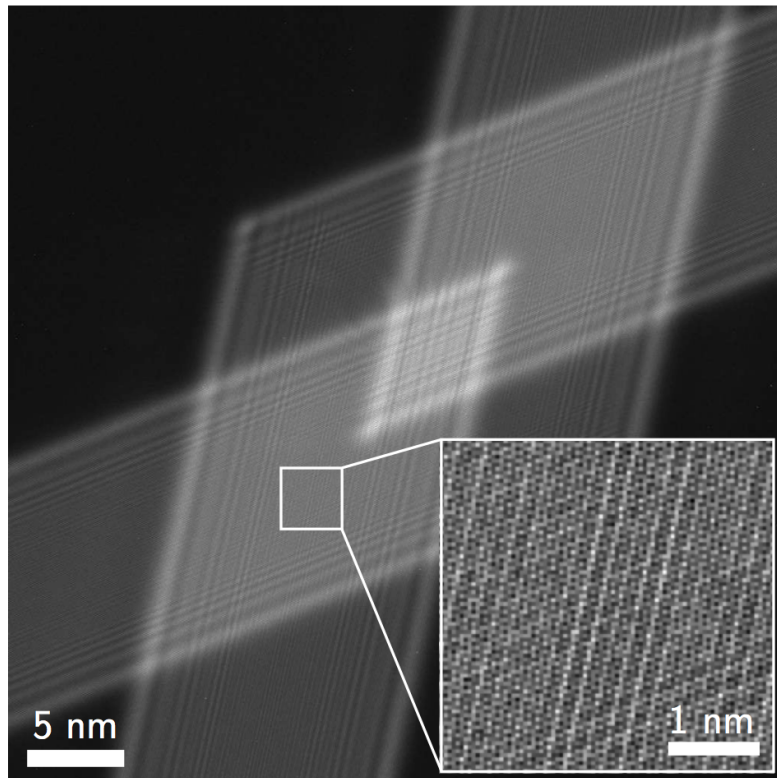


Fig. 2: Interference pattern produced by two biprisms separated by an angle of 60 degrees. The pattern contains regions of two-, three- and four-wave interference (identifiable by their intensities). The three-wave regions contain vortex lattices with a fringe spacing of 0.08 nm and a useable field of view approximately 10 nm wide.

IT-12. Surface microscopy, spectromicroscopy and microspectroscopy

Type of presentation: Poster

IT-12-P-6115 Angle-Resolved Cathodoluminescence Imaging Spectroscopy

Coenen T.¹, Brenny B. J.¹, Polman A.¹

¹FOM Institute AMOLF

Email of the presenting author: coenen@amolf.nl

Recently, electron-beam spectroscopy techniques have emerged as powerful probes in nanoscience due to their ability to generate, probe, and control light at length scales far below the diffraction limit of light. Taking advantage of the extremely high spatial resolution, novel techniques have appeared that combine electron beam excitation with optical spectroscopy. Spatially-resolved cathodoluminescence (CL) spectroscopy, in which the electron-beam-induced radiation is collected inside an electron microscope, is one of these techniques that holds great potential for nanoscience. For a long time CL spectroscopy was mainly used in geology to analyze and identify minerals, but in the past two decades its scope has expanded significantly. Recently it has been used to study fundamental optical properties of a myriad of metallic, semiconductor, and dielectric (nano)materials in the fields of materials science and nanophotonics, including plasmonics and metamaterials. We have developed a special version of CL spectroscopy in which we can both effectively measure the emitted spectrum as well as the angular emission distribution (Angle-Resolved Cathodoluminescence Imaging Spectroscopy, ARCIS) [1-3].

ARCIS is performed in a scanning electron microscope (SEM) which is relatively easy to operate and does not require electron-transparent samples. As a result the technique is widely applicable. Recent improvements to our CL-system, including an improved light collection with a piezo-controlled parabolic mirror and the development of angle-resolved CL, have further expanded the possibilities. In Figure 1 we show a photograph of the CL collection system (a) and an illustration of how the angle-resolved measurements are performed (b). We will explain in detail how our system operates and give several examples of the properties that can be measured on different types of (nano)materials. In Figure 1(c-d) we give an example of a spatial scan and an angular pattern, measured on a defect cavity in a photonic crystal membrane [3].

[1] T. Coenen, E. J. R. Vesseur, and A. Polman, *Appl. Phys. Lett.* 99, 143103 (2011).

[2] T. Coenen, E. J. R. Vesseur, A. Polman, and A. F. Koenderink, *Nano Lett.* 11, 3779 (2011).

[3] R. Sapienza, T. Coenen, J. Renger, M. Kuttge, N. F. van Hulst, and A. Polman, *Nature Mater.* 11, 781 (2012).

Acknowledgement: This work is part of the research program of the 'Stichting voor Fundamenteel Onderzoek der Materie' (FOM). It is also funded by NanoNextNL and the European Research Council (ERC).

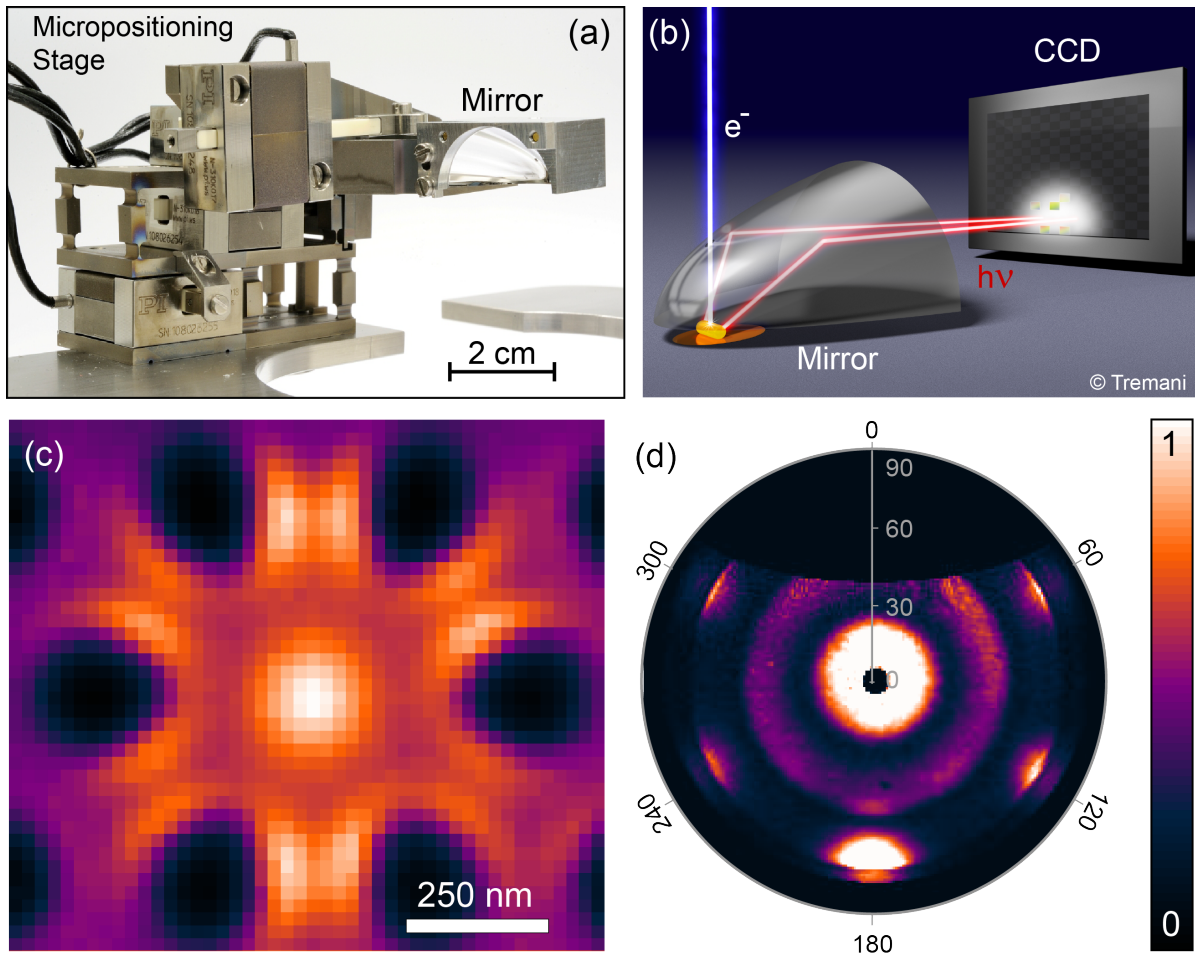


Fig. 1: (a) Piezo-controlled mirror system for efficient light collection (e) Graphical representation of angle-resolved detection of CL where light coming from a parabolic mirror is projected onto a 2D CCD. (c) Spatial CL emission distribution measured on a defect cavity in a photonic crystal membrane. (d) The corresponding angular pattern of the cavity.

IT-13. Focused ion beam microscopy and techniques

Type of presentation: Poster

IT-13-P-6109 High Resolution, Stable and Low Damage FIB Nanofabrication employing Gallium and New Ion Species

Bauerdick S.¹, Mazarov P.¹, Nadzeyka A.¹, Bruchhaus L.¹, Jede R.¹

¹Raith, Dortmund, Germany

Email of the presenting author: bauerdick@raith.de

FIB systems and combined FIB-SEM microscopes are widely used for sample preparation and various analytical tasks. The Gallium-based LMIS (liquid metal ion source), which has been ubiquitous with -FIB- for many decades, is partly giving way to GFIS (gas field ion source) microscopes, as well as Xenon -plasma- sources. This trend has been mainly driven by ultra-high resolution microscopy and large volume milling for special sample preparation applications, respectively.

Nanofabrication presents different and more demanding requirements for FIB in terms of stability, resolution, and the support of new processing techniques. To advance FIB nanofabrication applications, we report a significant advance in gallium-based LMIS with a stable gun emission design enabling long-term stability without the need for the frequent heating required at conventional gallium ion sources, and producing low drifts in probe current and beam position. Moreover, we report a FIB spot allowing excellent patterning resolution with low collateral damage. A FIB spot is usually not a pure Gaussian distribution, instead exhibiting significant beam tails outside the central spot, which have to be as small as possible for high resolution nanofabrication. In order to measure the beam current distribution we employed a method based on the amorphization of single crystal silicon by Gallium ions. Compared with conventional LMIS FIB, the results here show a very narrow and large central Gaussian part carrying >85% of the total current and very low tails. As the most relevant part for milling is in the dose range of 1 to 10⁻³, this technology offers superior performance, especially for nanofabrication.

The type of ion defines the nature of the interaction mechanism with the sample and thus has dramatic consequences the resulting nanostructures. Therefore, we have extended the focused ion beam technology towards the stable delivery of multiple species into a nanometer-scale focused ion beam by employing a liquid metal alloy ion source (LMAIS). A mass separation filter is incorporated into the column to allow for fast and easy switching between different ion species or clusters within seconds. This provides single and multiple charged species of different mass (Figure 1), e.g. Si, Ge and Au, resulting in significantly different interaction mechanisms. We present the capabilities of the multiple-ion instrument including excellent long-term current stability and sub-10 nm beam resolutions for various ions like Be, Si (Figure 2) and Au. The characteristics and applications of different species will be discussed in terms of patterning, functionalization, and imaging.

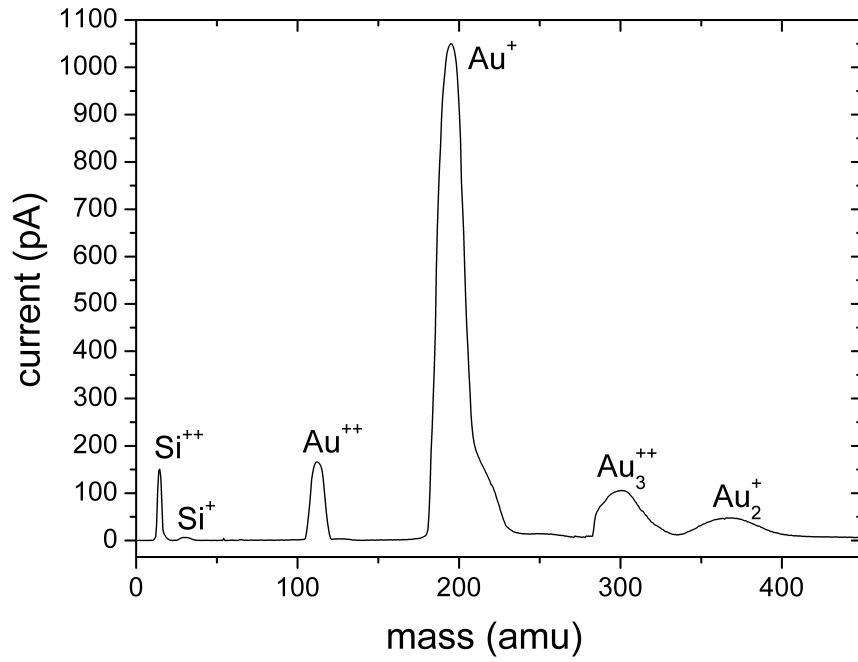


Fig. 1: Mass spectrum showing ions of different charge and mass for a single AuSi Liquid Metal Alloy Ion Source (LMAIS).

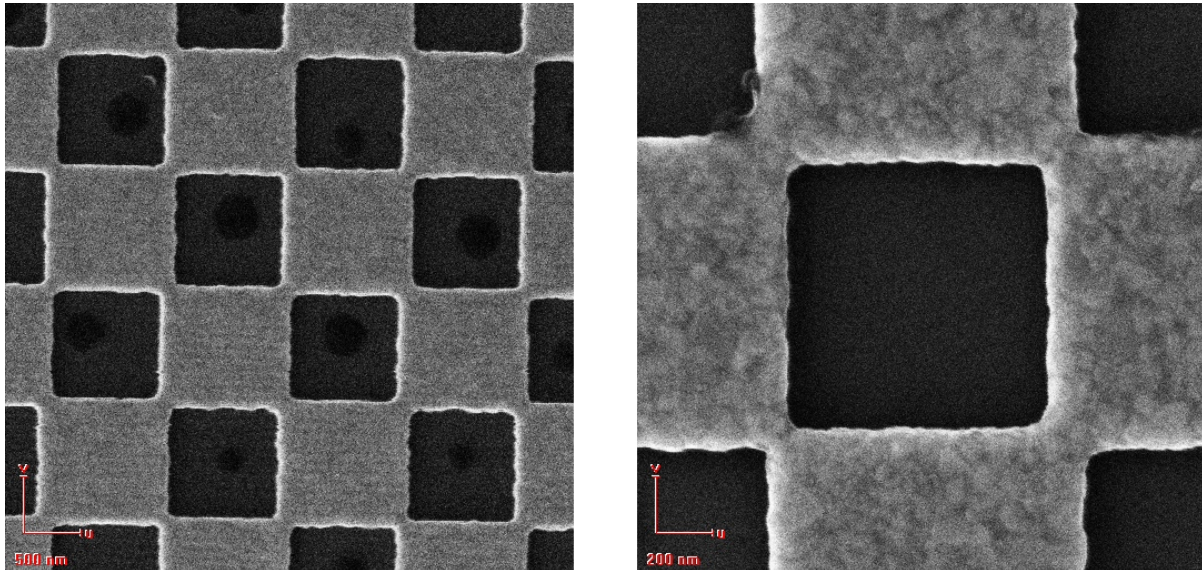


Fig. 2: Secondary electron images obtained by scanning a focused Si^{++} (left) or a Be^{++} (right) ion beam at 35 kV (70 kV ion energy) over a sample of gold squares ($1\ \mu\text{m}$) on silicon. The obtained beam diameters are about 6 nm and 3 nm, respectively.

IT-16. Electron microscopy theory and simulations

Type of presentation: Poster

IT-16-P-6075 Examination of the possibility of application of the Monte Carlo method for study of electron diffraction of textured nanocomposite materials

Kolonits T.¹, Czigány Z.¹

¹Institute for Technical Physics, Research Centre for Natural Sciences, Budapest, Hungary

Email of the presenting author: tomsolid65536@gmail.com

There are many various methods for calculating the electron diffraction of nanograined materials. However there is a size range (a few ten nanometres in grain size) where the exact methods (based on the Debye formula) have require to much computational capacity and the traditional numerical formulas (based on the line profile modification) are not reliable.

In this paper we propose a numerical method which provides results in a good range of error but has a runtime faster than the exact Debye formula. However the main advantage of our method - in addition to the speed - is that we can calculate the diffraction of patterns which can't be calculated by the exact Debye formula (e.g. samples having texture).

The acceleration is due to that the kernel algorithm of our Monte Carlo model is linear in the number of counted atoms instead of quadratic. In this paper we suggest how to choose the parameters of the simulation to reach the best error within the fastest runtime. Because of the nature of the numerical problem a special parameter was defined for quantifying the error of the simulation (Fig.1.). This parameter (delta-epsilon on Fig.1.) can be calculated on the fly and it is proportional to the difference from the exact value.

During the development we calculated the diffratogram of several nanograined nickel and fcc manganese samples. Using this calculations we ascertained the time dependence of the algorithm taking into account the expected error. Using this results we developed an adaptive algorithm which automatically chooses the simulation parameters to get the best runtime (Fig.2.).

Our conclusion is that in the case of non-textured material using the improved algorithm there is a range in grain size where the numerical method is significantly faster than the Debye formula. In the case of textured material there is no choice between the Monte-Carlo method and the Debye formula: the Debye formula simply doesn't work in this case.

Finally we present a way how can this simulation be used to estimate the grain size distribution from an electron diffractogram of a nanocrystalline metal sample (Fig.3-4.).

Acknowledgement: Acknowledgment: OTKA 81808 and Bolyai Research Scholarship of Hungarian Academy of Sciences are acknowledged for financial support.

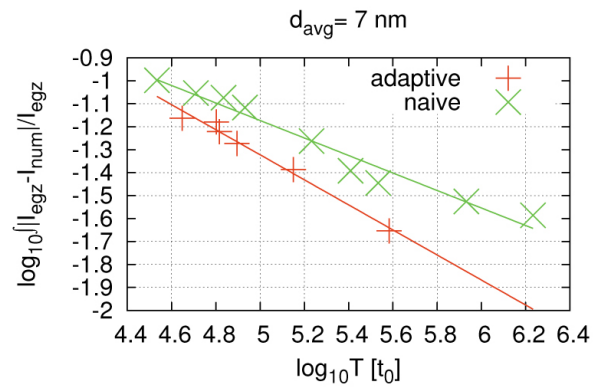
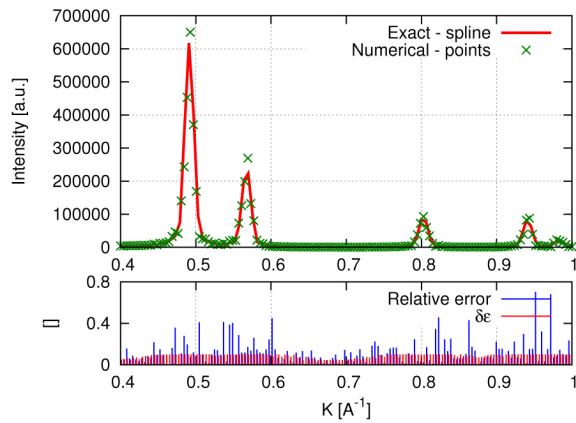


Fig. 1: The exact and the numerical simulation of a cluster having approx. 22000 atoms with the same runtime. Lower and the improved adaptive algorithms. graph: two error measurements parameter.

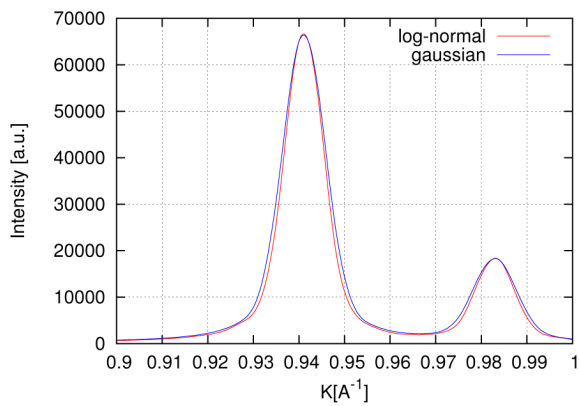


Fig. 3: The shape of the diffractive peaks in case of normal and log-normal grain size distribution (average 7 nm).

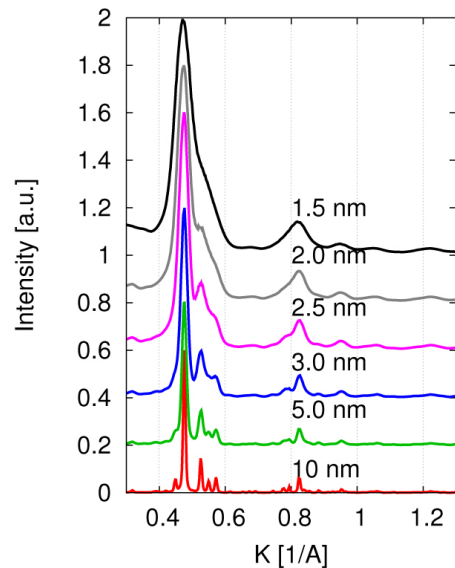


Fig. 4: Simulations for α -Mn having different average grain size. The smaller the grain size the bigger the broadening of the peaks.

Type of presentation: Poster

IT-16-P-6106 Improving quantification in Scanning Electron Microscopy by comparing transmission experiments with Monte Carlo Simulation.

Walker C. G.¹, Mika F.¹, Frank L.¹, Konvalina I.¹, Müllerová I.¹

¹Institute of Scientific Instruments of the ASCR, v. v. i., Brno, Czech Republic

Email of the presenting author: chris@isibrno.cz

Introduction

The quantification of signals from Scanning Electron Microscopes (SEMs) is still an area of research activity despite the longevity and widespread use of the SEM in the scientific literature. Knowledge of the transmission of electrons through thin films can provide important information regarding the thickness of the films. Hence a series of experiments were carried out to compare the transmission of electrons through thin films of various materials in the range 15-30keV to establish a quantitative basis for further investigations.

Experiment & Monte Carlo simulation

The experiments were carried out using an FEI ultra-high resolution Magellan 400 SEM [1] and a home built scanning low energy electron microscope (SLEEM)[2]. The Magellan SEM was equipped with a multi-annular semiconductor STEM detector (Fig. 1a) which is divided into a central disk and five concentric annuli, allowing imaging in the bright field (BF) mode, four dark field modes (DF1-4) and a high angle annular dark field (HAADF) mode. The detector was placed under the sample with the BF region on the axis of the electron column. Signals that were detected through a thin film were compared with signals with no film. The films were either Si or Au and 100nm thick and each signal was normalized to the intensity of the BF signal. The Magellan SEM was operated in high resolution mode, so magnetic fields were present in the sample region. These were taken into account in the simulation.

The SLEEM microscope was equipped with a YAG single channel scintillator screens for detecting both backscattered and transmitted electrons. The sample had zero bias and no magnetic field was applied, so the sample region was regarded as field free.

Electron transport simulations within each material was carried out using Monte Carlo (MC) calculations and modelling of the trajectories of the electrons in the magnetic field after the electrons had been emitted from the sample using the program EOD [3].

Results & Conclusions

Good agreement is found for the results from the SLEEM instrument (see Fig 1b). In contrast, the distribution of signals on the multi-annular detector show much greater intensities for the HAADF region in the MC simulations as compared to the experiment (see Figs. 2 and 3). This is especially the case for high Z elements. However, the overall trend across the different detectors is the same for experiment and simulation.

References

[1] www.fei.com

[2] Müllerová I., et al. *Microsc. and Microan.* 18 (2012), p. 996.

[3] Zlámál J., Lencová B., *Nucl. Instr. and Meth. A.* 645 (2011), p. 278.

Acknowledgement: The work is supported by the TA CR (TE01020118), MEYS CR (LO1212), its infrastructure by MEYS CR and EC (CZ.1.05/2.1.00/01.0017) and by ASCR (RVO:68081731)

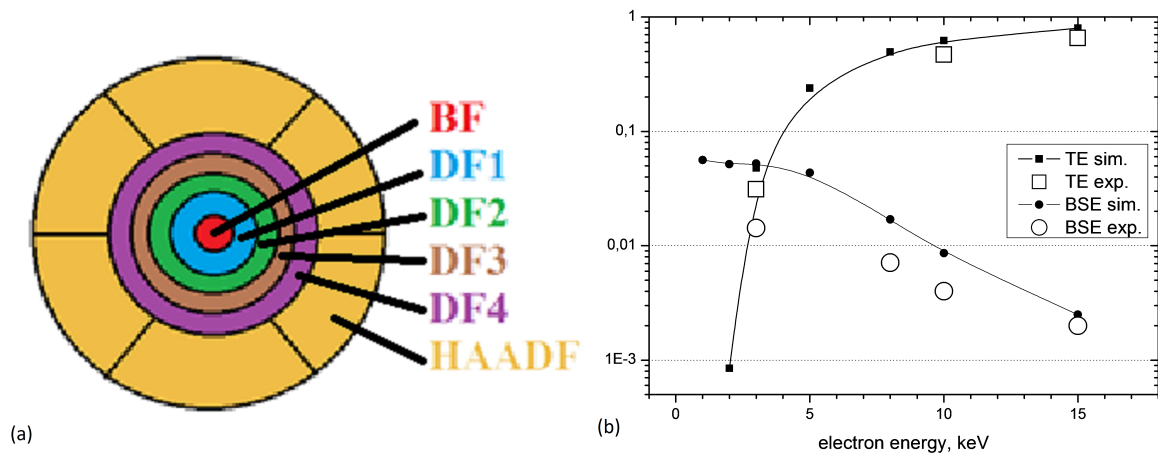


Fig. 1: Figure 1a. The multi-annular detector. BF = Bright Field, DF = Dark Field, HAADF = High Angle Annular DF. Figure 1b. SLEEM Instrument results (100nm Si). BSE = Backscattered Electrons, TE = Transmitted electrons. The discrepancy for BSE is believed due to difficulties in determining the 100% experimental signal and unknown detector response.

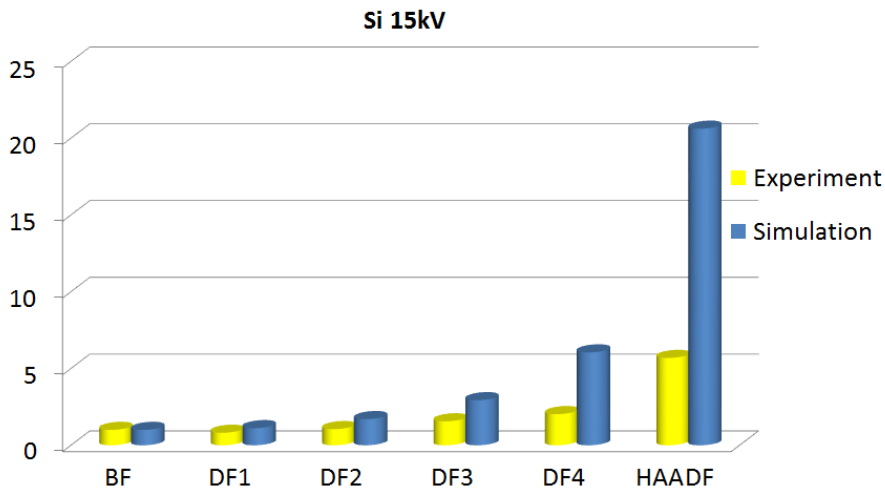


Fig. 2: Figure 2. Results from the Magellan - Si 15kV 100nm. All signals are normalised to the Bright Field (BF) signal.

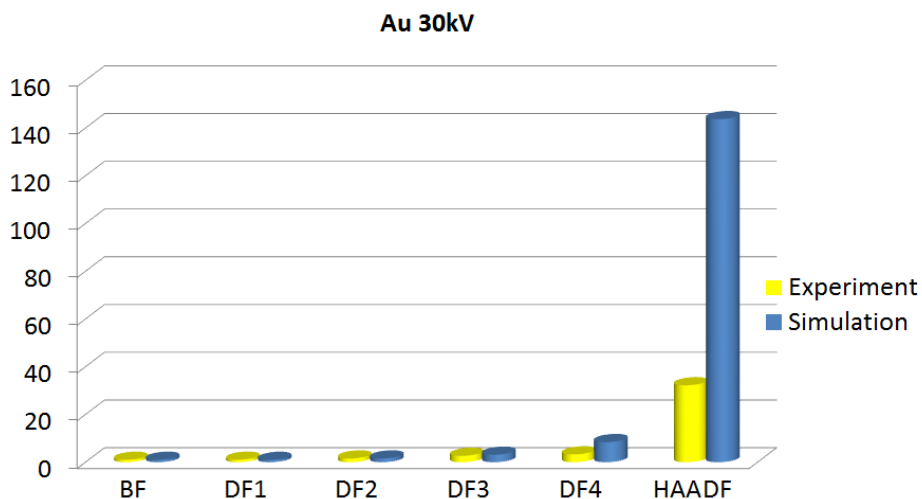


Fig. 3: Figure 3. Results from the Magellan - Au 30kV 100nm. All signals are normalised to the Bright Field (BF) signal.

Type of presentation: Poster

IT-16-P-6132 Resolution Simulation of the Practical Rayleigh Criterion Taking Account of Particle Diameter and Contrast-to-Noise Ratio for Scanning Electron Microscopes

Sasaki T.^{1,2}, Sato M.¹, Hidaka K.³, Onuki J.²

¹Hitachi High-Technologies Corporation, ²Graduate school of Science and Engineering, Ibaraki University, ³Department of Education, Art and Science, Yamagata University

Email of the presenting author: sasaki-tomoyo@naka.hitachi-hitec.com

The spatial resolution of Scanning Electron Microscopes (SEMs) is one of the most important factors for imaging and is closely connected with the electron beam size. In one of the classic definitions of the resolution of SEMs, the Rayleigh criterion, the theoretical resolution is defined as the minimum distance between the separate infinitesimal particles that can be distinguished; this resolution corresponds to the beam radius R_{Airy} of the Airy disk [1]. However, because the particles shown in the real SEM image have a certain size, their diameter D_p might cause a discrepancy between the theoretical resolution R_{Airy} and the practical resolution R_{es} . Moreover, although it is assumed that there is no brightness noise in the Rayleigh criterion, the brightness noise or contrast-to-noise ratio CNR cannot be neglected as an influential factor determining the spatial resolution of SEMs [2]. In this presentation, whose aim is to estimate more precisely the practical resolution R_{es} of SEMs, we demonstrate the simulation of the Rayleigh criterion taking account of the particle diameter D_p and the contrast-to-noise ratio CNR . The concept of the practical resolution R_{es} of SEMs in this simulation is shown in Fig. 1. In the Rose criterion, the minimum brightness contrast recognized as an image feature, not noise, at near 100% certainty is defined as 5 times the standard deviation σ_n of a Gaussian noise [3]. The practical resolution R_{es} is defined as the minimum distance L_{p-p} of particles satisfying the Rose criterion ($C_g \geq 5 \times \sigma_n$; the gap contrast C_g) and the Rayleigh criterion ($C_g \geq 1/4 \times C_p$; the particle contrast C_p) at the same time. The SEM images showing particles and their gap, which are shown in Fig.2, are simulated by convoluting binary particle images and blur functions, and adding the convoluted images and the Gaussian noise.

When $CNR = C_e / \sigma_n$ is worse, as shown in Fig.2(a), the Rose criterion should predominantly determine the practical resolution R_{es} . On the other hand, when CNR is good enough, as shown in Fig.2(b), the Rayleigh criterion should predominantly determine the practical resolution R_{es} . Furthermore, when CNR is good enough and the particle diameter D_p is small enough, the practical resolution R_{es} and the theoretical resolution R_{Airy} are almost in agreement, as in Fig.2(c), with an error 3%. In this presentation, other results and detailed consideration will be demonstrated.

[1] L. Rayleigh, Phil. Mag. **8** (5) (1879), p. 261.

[2] M. Sato and J. Orloff, Ultramicroscopy **41** (1992), p. 181.

[3] A. Rose, J. Opt. Soc. Am., **38** (2) (1948), p. 196.

Acknowledgement: The authors are grateful to Dr. A. M. Blackburn for his valuable comments.

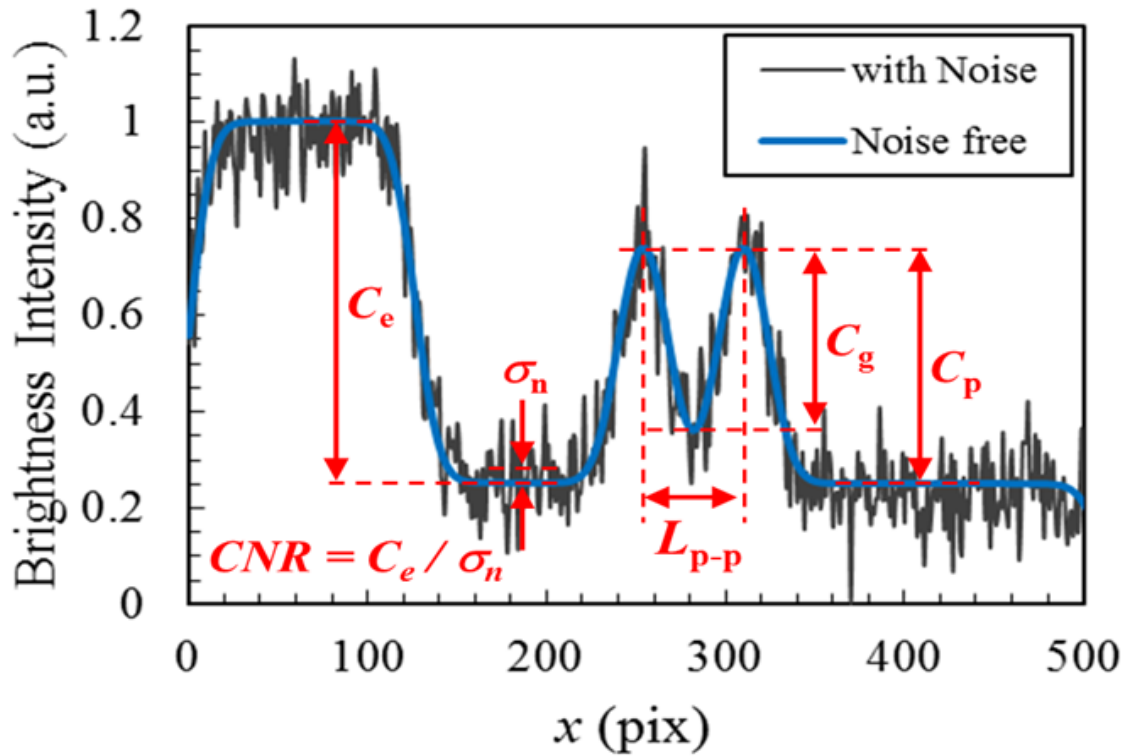


Fig. 1: The concept of the practical resolution R_{es} . The practical resolution R_{es} is defined as the minimum distance L_{p-p} of particles satisfying the Rose criterion ($C_g \geq 5 \times \sigma_n$; the gap contrast C_g , the standard deviation σ_n of a Gaussian noise) and the Rayleigh criterion ($C_g \geq 1/4 \times C_p$; the particle contrast C_p) at the same time.

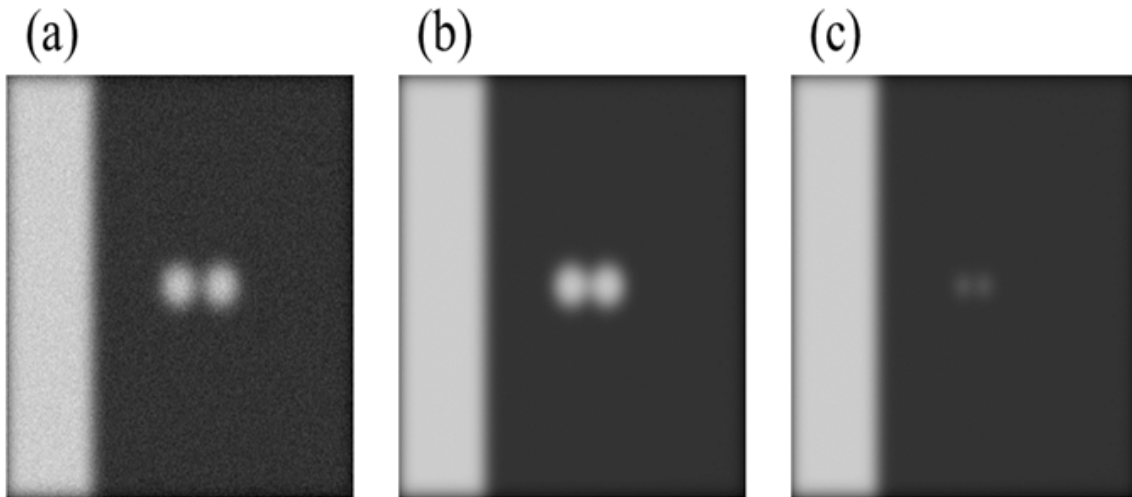


Fig. 2: The simulated SEM images (512×512 pixels, $R_{Airy} = 30$ pixels) showing particles and their gap. (a) $CNR = 10$, $D_p / R_{Airy} = 1.6$, and $R_{es} / R_{Airy} = 2.07$, (b) $CNR = 400$, $D_p / R_{Airy} = 1.6$, and $R_{es} / R_{Airy} = 1.77$, and (c) $CNR = 400$, $D_p / R_{Airy} = 0.4$, and $R_{es} / R_{Airy} = 1.03$.

IT-17. Atom probe and non-traditional microanalytical tasks

Type of presentation: Poster

IT-17-P-6104 Sub-angstrom resolution in 3D - Exploring high-resolution atom probe microscopy

Liddicoat P. V.¹

¹The University of Sydney

Email of the presenting author: peter.liddicoat@sydney.edu.au

The atom probe (AP) microscope's 3D sub-nanometre resolution and parts per million sensitivity has enabled revealing new phenomena in high-impact studies of nanostructured electronic, structural, and functional materials. Yet, the scale at which next generation materials are being designed – atomic layers or single atoms – drives a demand for an order of magnitude increase in both resolution and sensitivity. AP resolution is limited by field-evaporation effects and constrained by the detection efficiency of the atoms, ~50% in most instruments. In this paper, a multi-modal imaging method and data feature synthesis is demonstrated to achieve 3D sub-angstrom resolution and ~100% efficiency.

Acknowledgement: PVL would like to acknowledge the scientific, technical and financial support from the Australian Microscopy & Microanalysis Research Facility (ammrf.org.au) node at The University of Sydney, Sydney Microscopy & Microanalysis, and the Australian Research Council under the DECRA funding scheme (project number DE120102778).

MS-1. Nanoobjects and engineered nanostructures, catalytic materials

Type of presentation: Poster

MS-1-P-6137 Sb-Te films: crystallized microstructures and "transrotation" examined by TEM

Kolosov V. Y.¹, Schwamm C. L.¹, Veretennikov L. M.¹

¹Ural Federal University

Email of the presenting author: Vladimir.Kolosov@usu.ru

Transmission diffraction electron microscopy including bend-contour pattern analysis [1] was used to study peculiarities of crystal growth and microstructure in thin binary *Sb-Te* films evaporated preferably with strong gradients in thickness and composition (in mutually perpendicular directions) [2]. Vacuum deposits with very thin carbon sublayer were usually initially amorphous, Fig. 1. Upon aging or being exposed to more intense electron beam these films undergo amorphous - crystalline transformation. Two main phases (Figs. 1-5) of crystalline areas were *Sb* (JCPDS №05-0562) and *Te* (JCPDS №04-0554). Very **intriguing is the internal crystal lattice bending of different geometry** [3] (e.g. negative for Fig.1 or positive for Fig. 5 a-b) with diverse lattice orientation gradients (minimal at Fig. 2a and strong at Fig. 2b) observed for both phases. This phenomenon often accompanies the crystallization in amorphous films as follows from our studies of numerous extinction bend-contour patterns on TEM images. Besides above "transrotation" [4] *Sb* crystal growth results primarily in fine-grained microstructures which differ in grain size, grain/crystallite morphology, crystal texture ([0 0 1] and [-1 1 1] are dominated, Fig. 1-2) and domains (detectable only in dark field, Fig. 3 a-b). The microstructures of hexagonal *Te* are even more varied in the range from fine-grained crystalline matrix (Fig. 4 c) to rather large isolated crystals (up to several μm in length) surrounded by amorphous phase (Fig. 4 a). The last are most prominent examples of transrotational crystals with regular internal lattice bending (torus-like bending geometry) **exceeding 100 degrees/ μm** (shown schematically by rotation of hexagons in imaginary cross-section along (001) planes at Fig. 5 a, and also at the bottom of the scheme of Fig. 5 b). The total rotation of the unit cell along the crystal length at Fig. 5a is almost 360 degrees and is one of the unambiguous proofs of the internal lattice bending rather than crystal bending/buckling as a whole. Such transrotation was recognized in particular in some phase-change materials used for non-volatile memory devices including DVD RW [5, 6].

[1] I. E. Bolotov and V. Yu. Kolosov, Phys. Stat. Sol. 69a (1982), 85.

[2] V. Yu. Kolosov et al, Semiconductors, 39 (2005), 955 (Springer, translated from Russian)

[3] V. Yu. Kolosov, Proc. 13 EMC, Antwerp, v.II (2004), 255

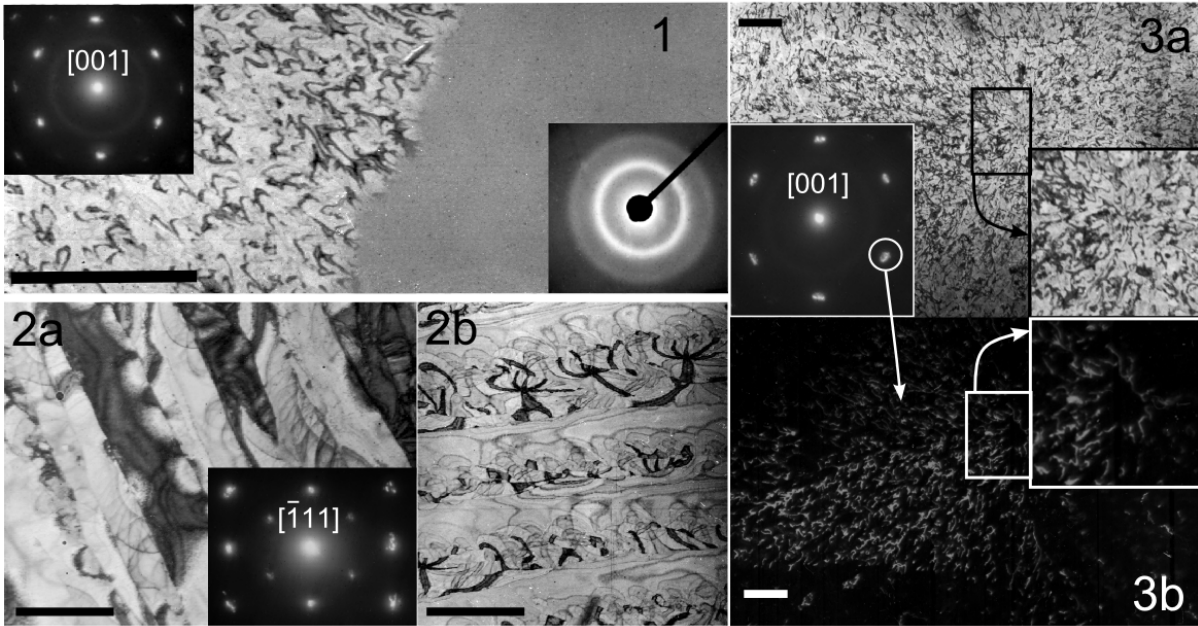
[4] V. Yu. Kolosov and A. R. Tholen, Acta Mater. 48 (2000) 1829.

[5] B. J. Kooi and J. T. M. De Hosson, J. App. Phys. 95 (2004), 4714.

[6] E. Rimini et al, J. App. Phys. 105 (2009), 123502.

Acknowledgement: Partial support of RFBR (grant 12-03-01118) and RF Ministry of Education and Science is acknowledged

Sb



Te

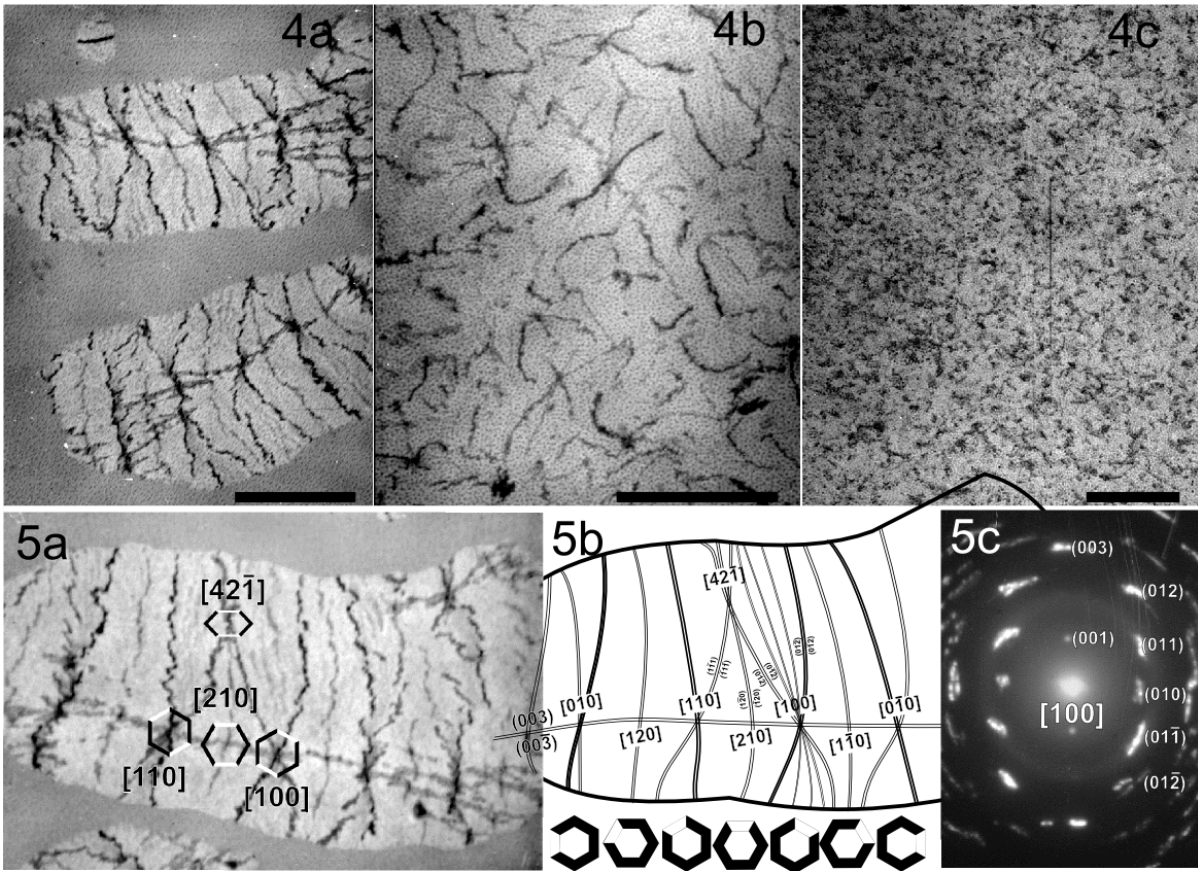


Fig. 1: -5: 1 - Sb amorphous-crystalline front. 2 - Elongated grains, texture with transrotation: weak (a) and strong (b). 3 - Sb domain in b.f. (a), d.f. (b). 4 -Te microstructures (a- crystal in amorphous matrix, b, c - larger and smaller grains). 5 - Transrotational Te crystal (a) with scheme of bend contours and orientations below (b), SAD (c). Bar=1 μ m

MS-3. Thin films, coatings and surfaces

Type of presentation: Poster

MS-3-P-6128 TEM study of Epitaxial SrIrO₃ Thin Films Grown by Pulsed Laser Deposition Technique

Kim E.¹, Kuo C. T.^{2,3}, Sohn W.¹, Kang S. J.^{1,2}, Kim M.^{2,3}, Kim M.¹, Noh T. W.^{2,3}

¹Department of Materials Engineering, Seoul National University, Seoul 151-747, Republic of Korea, ²IBS-CCES, Seoul National University, Seoul 151-747, Republic of Korea, ³Department of Physics and Astronomy, Seoul National University, Seoul 151-747, Republic of Korea

Email of the presenting author: eunju0316@snu.ac.kr

Recently, 5d transition metal oxides (5d TMOs) attract much attention due to their intriguing physical properties driven by strong spin-orbit coupling. For example, it was demonstrated that novel insulating states could emerge from the competition between spin-orbit coupling and electron correlation in the Ruddlesden-Popper series of $\text{Sr}_{n+1}\text{Ir}_n\text{O}_{2n+1}$ [1]. Theoretically, 5d TMOs are predicted as possible candidates for novel topological insulator [2], for example, Weyl semimetal or Axion insulator, originating from the correlation effect of oxides. However, optimizing growth conditions of the materials is found to be difficult, prohibiting from unraveling electronic structure.

In this study, we report the characterization of epitaxially grown SrIrO₃ thin films on the SrTiO₃ (001) substrate. The SrIrO₃ thin films are grown by pulsed laser deposition technique with in situ high-pressure reflection high-energy electron diffraction (RHEED). Based on the oscillation of RHEED pattern intensity, we can monitor the growth mode in real time making it much faster to confirm the ideal growth condition at which films are grown with layer by layer growth mode. The surface morphologies of the films are further confirmed by atomic force microscope (AFM). We can observe clear step-and-terrace structure in the high quality thin film samples. For chemical investigation, energy dispersive spectroscopy is used to examine the stoichiometry of films.

The crystalline quality and epitaxial arrangement are determined with high-resolution X-ray diffraction (XRD) and cross-sectional transmission electron microscopy (TEM). The XRD spectra show that SrIrO₃ thin films are well stabilized with pseudo-cubic perovskite structure. The high-resolution TEM images (HRTEM) show epitaxially grown SrIrO₃ thin film on SrTiO₃ substrates.

Figure 1 shows a HRTEM image of the SrIrO₃ thin film showing a misfit dislocation. For clarifying epitaxial relationship, we filtered the HRTEM image using inverse Fourier Transformation and observed edge dislocations near the interface which help release the misfit strain between the film and substrate. Inset of Figure 1 is a Fast Fourier Transformation image including superlattice spots. On the other hand, Figure 2 shows the area without any edge dislocation. The interface between the films and the substrate is further studied using scanning transmission electron microscopy. Our results demonstrate the possibility to investigate the non-trivial topological properties of SrIrO₃ thin films.

Acknowledgement: This work was supported by the Institute for Basic Science (IBS) in Korea (IBS-R009-D1-2014-a01).

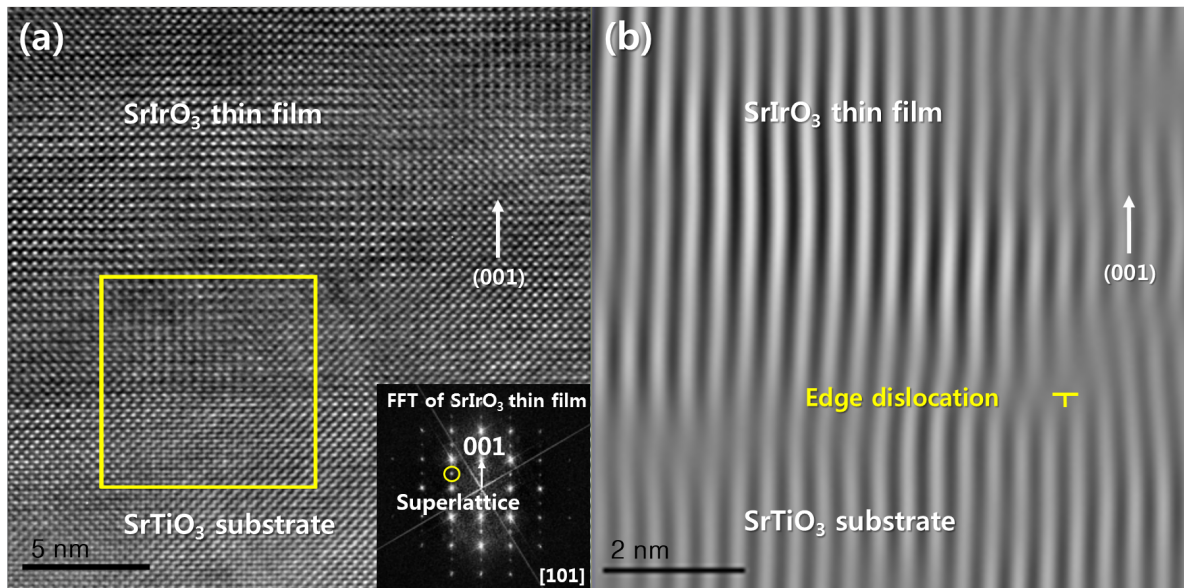


Fig. 1: (a) HRTEM images of SrIrO₃ thin films on SrTiO₃ substrate near the interface. Inset of (a) shows Fast Fourier Transformation image (FFT) of SrIrO₃ thin film. (b) Inverse Fourier-filtered image of square marked area in (a) shows the presence of edge dislocations at the interface between film and substrate.

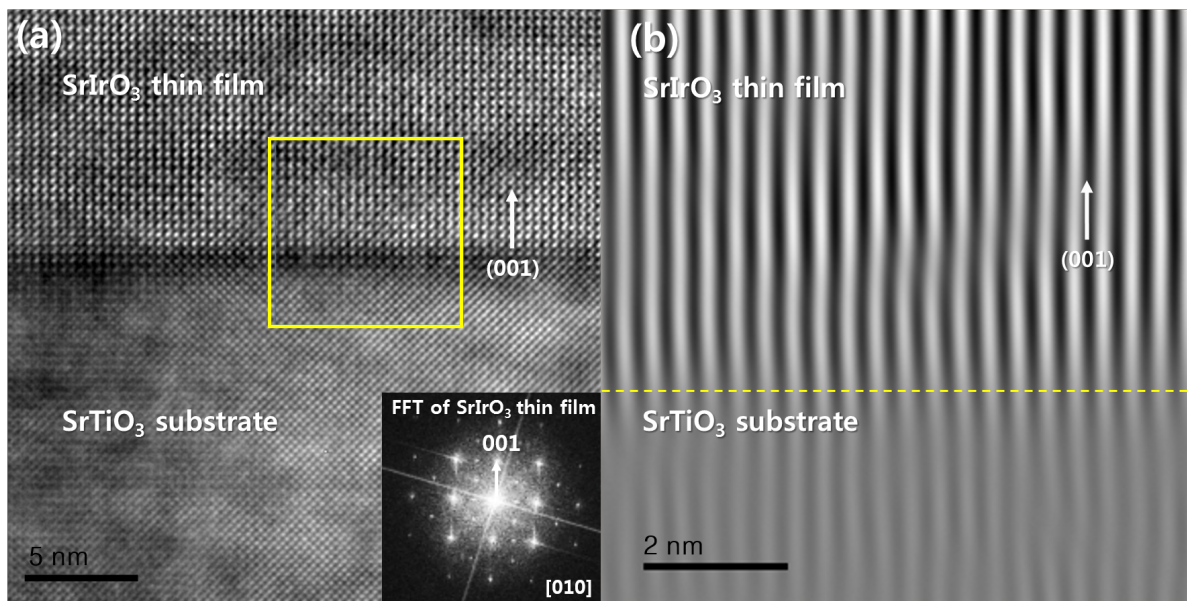


Fig. 2: (a) HRTEM images of SrIrO₃ thin films on SrTiO₃ substrate near the interface (different region with Figure 1. (a)). Inset of (a) shows Fast Fourier Transformation image (FFT) of SrIrO₃ thin film. (b) Inverse Fourier-filtered image of square marked area in (a) shows sharp interface between film and substrate with fewer edge dislocations.

MS-4. Metals, alloys and metal matrix composites

Type of presentation: Poster

MS-4-P-6120 Microstructure Evolution in the Corrosion of Steel Alloys

Gelb J.^{1,2}, Lechner L.², Merkle A.²

¹San Jose State University, San Jose, CA, USA, ²Carl Zeiss X-ray Microscopy, Pleasanton, CA, USA

Email of the presenting author: jeff.gelb@zeiss.com

Steels in the 4100 series are commonly used as structural reinforcements, in automotive components, and in the manufacture of firearms. While these alloys exhibit superior strength to weight ratios as compared to standard 1020 steels, the small amounts of chromium (~1%) incorporated into the 4100 series steels are generally not sufficient to provide high corrosion resistances. As such, corrosion may present failure modes for devices made with these alloys, and a complete understanding of the corrosion process may help to better predict the nature of the materials' ultimate performance.

In this work, a small sample of 4130 chromoly steel was prepared using a focused ion beam lift-out technique and imaged using non-destructive X-ray microscopy with 150 nm resolution. The XRM technique preserves the sample during imaging, allowing the sample to be imaged repeatedly after a time span or environmental treatment. The same sample was then exposed to repeated treatments in a fully saturated aqueous sodium chloride solution to initiate and accelerate corrosion, and XRM datasets were collected after 1, 2, 4, and 7 days of treatment. The results provided, for the first time, a 4D depiction of the corrosion process of 4130 steel, including formation of the oxide, roughening of the surface, and the formation of small pits at the steel/oxide interface. A similar study, performed using micron-scale resolution and a treatment time of 6 weeks will also be presented, to demonstrate the larger-scale corrosion on 4130 steel. Results from a second trial of a different steel alloy will additionally be presented, showing both 4D micro- and nano-scale microstructure characterizations of the corrosion process, and routes toward chemical characterization using correlative XRM-SEM-EDS will also be discussed.

Acknowledgement: The authors wish to acknowledge Prof. Tyler Ley at Oklahoma State University for many useful discussions in designing this experiment. We also thank San Jose State University for their advice and support.

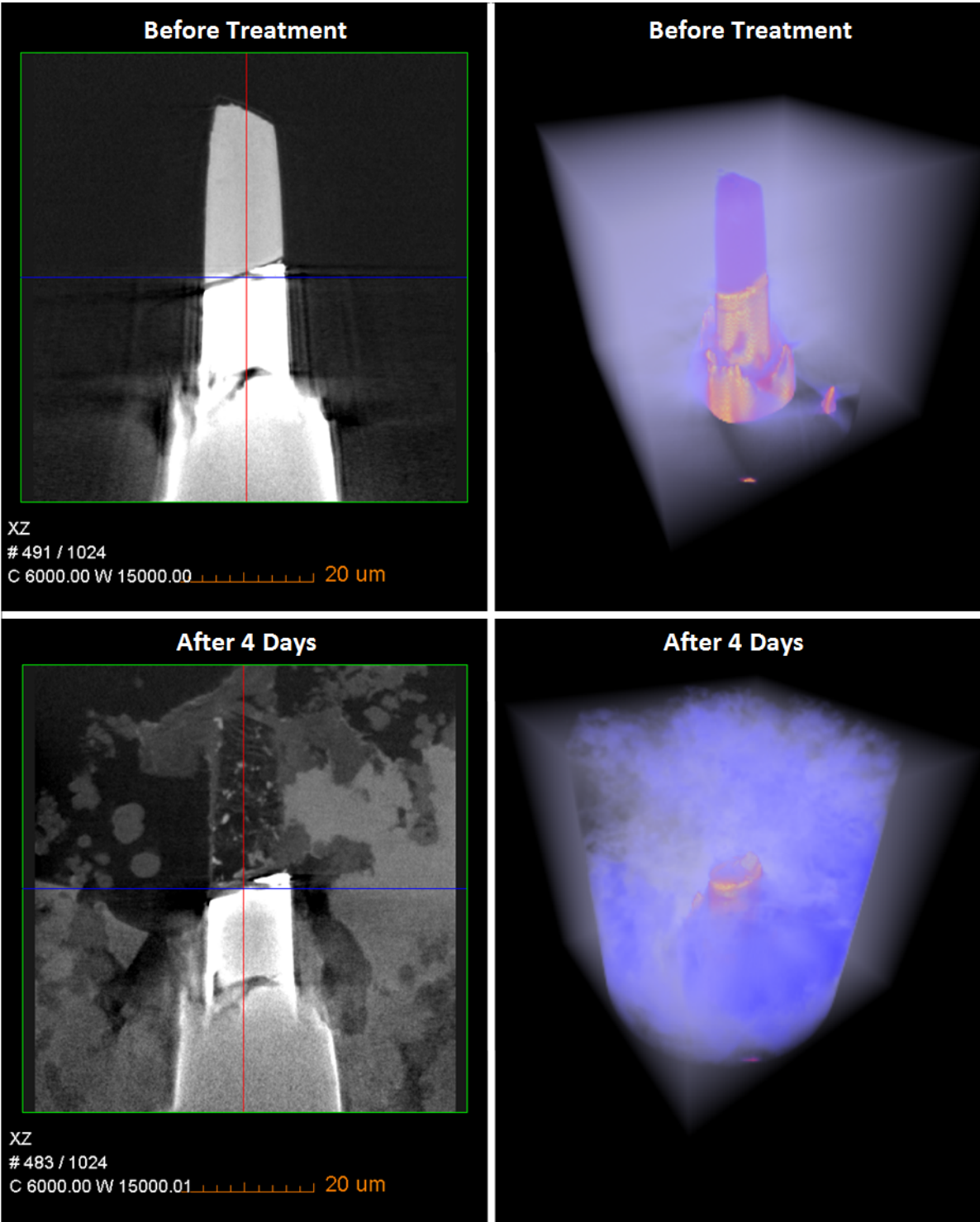


Fig. 1: Virtual slices (left) and 3D volume renderings (right) of the 4130 steel sample before and after solution treatment. Secondary phase formation is clearly seen after 4 days.

MS-6. Polymers and organic materials

Type of presentation: Poster

MS-6-P-6092 TEM of Layered Silicate Nanocomposites Based on Polyamide-6

Orekhov A. S.^{1,2}, Cherdyntseva S. V.¹, Vasilev A. L.^{1,2}, Chvalun S. N.¹

¹National Research Center "Kurchatov Institute", Moscow, Russia, ²Shubnikov Institute of Crystallography of the Russian Academy of Sciences, Moscow, Russia

Email of the presenting author: orekhov.anton@gmail.com

Polyamide 6 is a widespread large capacity polymer applied in different fields of industry. The main way (98%) of polyamide 6 formation is the hydrolytic polymerization. Another method (2%) is anionic polymerization [1]. The improving of mechanical, barrier and thermal properties of the composite can be achieved by adding of nanosized particles to the polymer matrix with homogeneous distribution of the nanoparticles in the polymer and the formation of a strengthened percolation net of the interacting particles. Nanoparticles with a large aspect ratio e.g., different nanotubes or nanofibers, including carbon nanotubes and layered silicates could be the optimal fillers for such goals. One promising filler is the montmorillonite clay mineral [2], which is the layered silicate. To improve the performance of the MMT- polyamide 6 composite, the number of sample were studied by TEM/HREM/EELS/EDXS.

The samples were prepared by microtoming in a Leica UC7 ultramicrotome with a diamond knife, at room temperature. The slice thickness was of 30-50 nm. Electron microscopy study was performed on Titan 80-300 TEM/STEM (FEI, USA) with attached Gatan GIF and EDX spectrometer (EDAX, US).

Three steps of composite formation were found: 1.The micro composite with the MMT particles before the exfoliation and intercalation (Fig.1), the nanocomposite with a large density of intercalated particles (Fig.2) and the nanocomposite with mostly exfoliated particles (Fig.3). The interplanar distances and the uniformity of MMT particle distribution together with texture were studied.

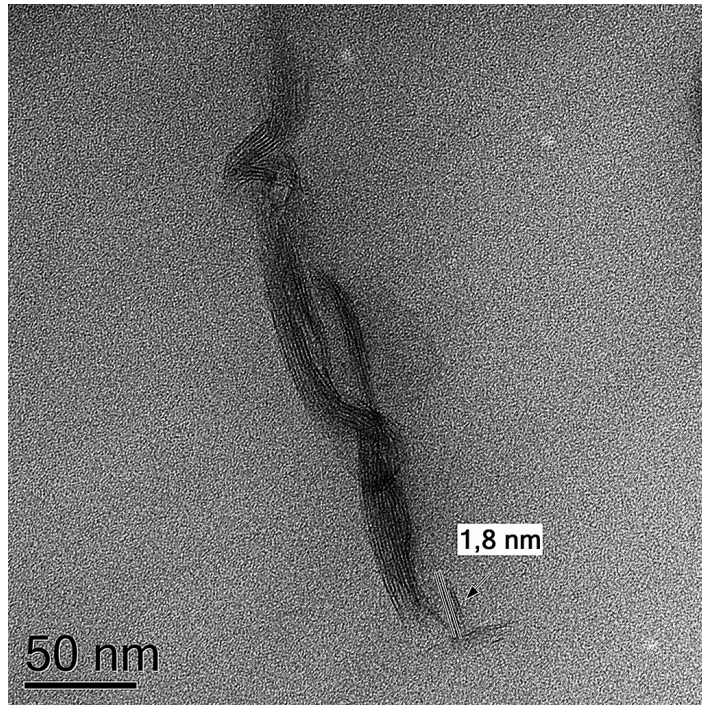


Fig. 1: Micro composite

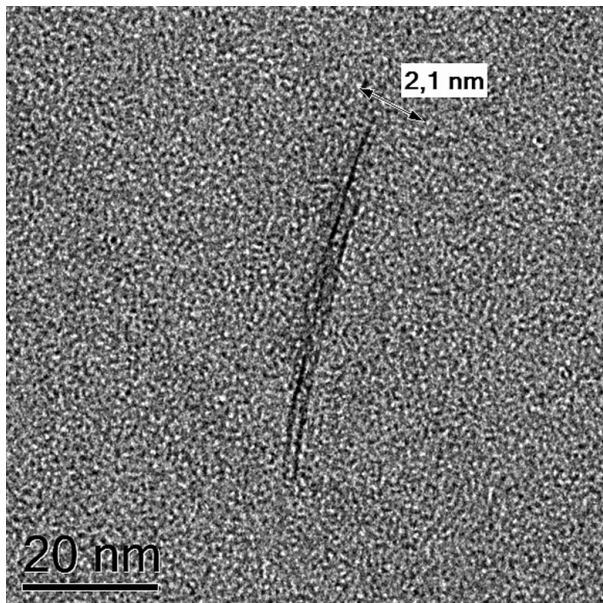


Fig. 2: Intercalation

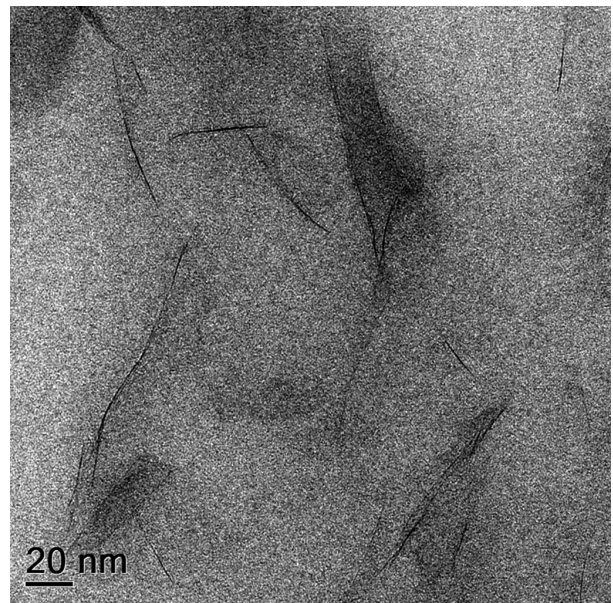


Fig. 3: Exfoliation

MS-8. Semiconductors and materials for information technologies

Type of presentation: Poster

MS-8-P-6133 Metal Oxide Semiconductor Capacitor fabricated by Electron Beam Induced Deposition

Shawrav M. M.¹, Tiefenbacher S.¹, Wanzenboeck H.¹, Belic D.¹, Gavagnin M.¹, Bethge O.¹, Bertagnolli E.¹

¹Institute of Solid State Electronics, Vienna, 1040, Austria

Email of the presenting author: stefan.tiefenbacher@tuwien.ac.at

Recently, the amount of functional units within chips and other electrical building blocks increased dramatically, notwithstanding the size of these electrical components decreased. An improvement in Lithography, which is the dominant method to produce structures in the sub-micro scale, made this development possible but due to the need of a mask and resist the handling of the process in nanometer scale becomes more and more challenging.

An alternative to Lithography could be focused electron beam induced deposition (FEBID), which is a resist-free and mask-free direct writing technology where metals and dielectrics from a precursor gas can be deposited with the help of an electron beam in a single step. Due to the nanometer precision and its ability of depositing noble metals, FEBID is a promising technology for creating 2D and 3D nanoelectronics.

In this work, FEBID will be explored to fabricate noble metal based devices such as metal oxide semiconductor capacitor, which is one of the basic building blocks of Si Nanowire transistors.

To obtain a MOS capacitor, process parameters such as precursor temperature, substrate temperatures etc. have been optimized to increase the rate of deposition. The effect of these parameters in the shape and chemical composition of the deposited structure will be shown. Defocusing option of the electron beam will be used to deposit a planar structure with higher metal content.

To check the conductivity of the FEBID gold, a nanowire has been deposited to connect 5 lithography patterned contact. I-V measurement indicates the tunneling type of electrical conductivity in the gold nanowire. Top electrode of the MOS capacitor structure was fabricated by the FEBID. Corresponding C-V measurements shows a clear capacitor type behavior on the FEBID deposited MOSCAP.

Acknowledgement: European Community's Seventh Framework Programme (FP7/2007-2013) under grant agreement number ENHANCE-238409

Center for Micro- and Nanostructures (ZMNS) & TU WIEN

University Service Centre for Transmission Electron Microscopy (USTEM), TU WIEN

MS-9. Defects in materials and phase transformations

Type of presentation: Poster

MS-9-P-6131 On the complex superstructural ordering of oxygen absorption-desorption in the system $\text{BaFeO}_{3-\delta}$, $0 \leq \delta \leq 0.5$

El Hadri A.², Del Río E.³, Hernández J. C.³, Varela A.², González-Calbet J. M.^{1,2}, Parras M.², Hernando M.², Delgado J. J.³, Pérez-Omil J. A.³, Calvino J. J.³, García-García F. J.¹

¹ICTS-Centro Nacional de Microscopía Electrónica, Facultad de Ciencias Químicas, Universidad Complutense de Madrid, 28040-Madrid, Spain, ²Dpto. Q. Inorgánica, Fac. de Químicas UCM, 28040-Madrid, Spain, ³Dpto. Ciencia de los Materiales e Ingeniería Metalúrgica y Química Inorgánica, F. Ciencias, Universidad de Cádiz, Campus Universitario Río San Pedro s/n, 11150-Puerto Real, Cádiz, Spain.

Email of the presenting author: javier.garcia@cnme.es

In this communication we address the crystal-chemistry implications of an oxygen absorption-desorption process. Nowadays these processes are of high interest in several technological applications. The compound under study is the hexagonal perovskite $6\text{H-BaFeO}_{2.7}$ [1] and we have studied the properties in relation to the oxidation of CO to CO₂. As a first step, we must be aware of the fact that experimentally, in what transmission electron microscopy concerns, an "in-situ" study of the reaction is impossible. Furthermore, the very same conditions than in the catalytic reaction are impossible to reproduce in an "ex-situ" TEM experiment. However, taken into account that the most important steps in the catalysis process is the ability of the oxygen absorption-desorption, we have tried to monitor the evolution of the crystal structure of this compound in two different manners.

Due to the high vacuum inside the column of the electron microscope, along with the help of a high temperature stage and the high energy of the incident beam of electrons, a quite reductive atmosphere should be present and it should push this compound into desorb oxygen in a somehow similar way as it should happen in the studied reaction. A second approach to gain information about the process, was the possible stabilization of the catalyst at the intermediate working temperatures where the catalysis occurs. Thus, we have tried to stabilize the intermediate compounds that might show up in function of oxygen loss, as obtained in the thermo-balance.

We here present and discuss these careful studies and surprisingly we will present some common results from these two different experiments which we interpret as being at the very heart of the catalysis process.

[1] K. Mori, T. Kamiyama, H. Kobayashi, T. Otomo, K. Nishiyama, K. Itoh, T. Fukunaga, S. Ikeda, J. Appl. Cryst., 2007, 40, s-501-s505

Type of presentation: Poster

MS-9-P-6134 TEM of radiation damage in ferritics: role of image forces

Schaeublin R. E.^{1,2}, Wu W.³, Hébert C.⁴, Prokhodtseva A.⁵, Décamps B.⁶, Löffler J.²

¹ScopeM, ETH Zürich, Switzerland, ²LMPT, ETH Zürich, Switzerland, ³NES, Paul Scherrer Institut, Villigen PSI, Switzerland, ⁴LEMS and CIME, EPFL, Lausanne, Switzerland, ⁵CRPP, EPFL, Villigen PSI, Switzerland, ⁶CSNSM, CNRS - Université Paris-Sud 11, Orsay, France

Email of the presenting author: robin.schaeublin@scopem.ethz.ch

A review of the primary damage induced by irradiation in ultra high purity (UHP) Fe(Cr) alloys investigated by transmission electron microscopy (TEM) is given, with a critical analysis of results with respect to the presence of the free surfaces inherent to the TEM thin foil. Indeed, free surfaces induce so-called elastic “image forces” that can bias the resulting irradiation induced damage. This was soon remarked, first by Masters in 1963 [1], in the study of the type of dislocation nanometric loops induced in pure Fe thin foils at 500-600°C. Since then many studies have confirmed that in such a thin foil the loop population is dominated by $a_0\langle 100 \rangle$ loops, counterbalancing the $\frac{1}{2} a_0\langle 111 \rangle$ ones observed in bulk irradiated Fe, even at lower temperatures. Here we review results of UHP Fe(Cr) irradiations at room temperature in situ in a TEM coupled to two ion accelerators, providing simultaneously 500 keV Fe⁺ and 10 keV He⁺ ions [2,3]. Single Fe ions and dual Fe and He ions beam experiments were performed up to a dose of 1 dpa and to a He content of up to 1000 appm. Defects appear in TEM bright field imaging in the form of nanometric black dots with sizes between 1 and 5 nm; they stem from nanometric dislocation loops. From these studies it is concluded that the primary loop population is dominated by $\frac{1}{2} a_0\langle 111 \rangle$ loops, which in thin foils escape to free surfaces, contrary to $a_0\langle 100 \rangle$'s. This is now for the first time quantitatively explained by a proper analysis of the image forces using recent elasticity of the continuum development [4]. Figure 1 shows that the bulging of the free surface induced by a nanometric loop just beneath it is remarkable. These recent calculations of the image forces indicate that free surfaces have a strong effect on the loop population within the Fe foil, with a much larger and deeper impact within the foil on the $\frac{1}{2} a_0\langle 111 \rangle$ relative to the $a_0\langle 100 \rangle$ loops because of the strong anisotropy of Fe. This is shown in Fig. 2, comparing the stress field induced by both types of loop. Results will be presented here, with the first experimental validation of image forces using TEM on dislocations in Fe.

[1] B.C. Masters, “Dislocation loops in irradiated iron”, *Nature*, 200, 254 (1963).

[2] A. Prokhodtseva, B. Décamps, A. Ramar, R. Schaeublin, *Acta Materialia*, 61, 6958 (2013)

[3] A. Prokhodtseva, B. Décamps, A. Ramar, R. Schaeublin, *Journal of Nuclear materials*, 442, S786 (2013)

[4] W. Wu, J. Chen, R. Schaeublin, *Journal of Applied Physics*, 112, 093522 (2012)

Acknowledgement: Financed by the EC for EFDA, the Swiss National Science Foundation and PSI. Experiments were done at JANNuS, Orsay, France, and supported by the French Network EMIR and by EFDA. The authors acknowledge the outstanding work of the JANNuS team.

MS-10. Porous and architected materials

Type of presentation: Poster

MS-10-P-6107 Mesoporous zeolite Y studied by rotation electron diffraction and electron tomography

Xiao C. H.¹, Wan W.¹, Zou X. D.¹, Li K. H.², Garcia-Martinez J.^{2,3}

¹Berzelii Center EXSELENT on Porous Materials and Inorganic and Structural Chemistry, Department of Materials and Environmental Chemistry, Stockholm University, SE-106 91 Stockholm, Sweden, ²Rive Technology, Inc., 1 Deer Park Drive, Suite A, Monmouth Junction, NJ 08852, USA, ³Molecular Nanotechnology Lab, Department of Inorganic Chemistry, University of Alicante, Campus de San Vicente E-03690, Alicante, Spain

Email of the presenting author: wei.wan@mmk.su.se

Microporous zeolites with at least another pore system of meso- (2-50 nm) or macro-sizes (>50 nm) potentially offer the desired fast diffusion, strong zeolitic acidity, and high hydrothermal stability for optimal catalytic performance. By using a simple surfactant-templating post-synthetic modification process (~2-6 nm in size, controlled by the size of the surfactant micelles), a type of mesoporous zeolite Y crystals were prepared [1], which showed significantly improved product selectivity of the fluid catalytic cracking catalysts in both laboratory testing and refinery trials [2]. Here we present a structural study of the mesoporous zeolite Y by advanced characterization techniques, such as electron tomography (ET)[3] and three-dimensional rotation electron diffraction (RED)[4], to reveal the intra-crystalline nature and connectivity of the introduced mesopores [5]. ET and RED data were collected from the same meso-structured zeolite Y particle. A tilt series of bright-field TEM images of the particle was acquired over an angular range of about $\pm 75^\circ$ with the increment of 1° . RED data was collected on the same crystals after electron tomography data collection. The 3D reciprocal lattice and tomogram were reconstructed from the ET and RED data, respectively.

Figure 1a shows that the mesoporous Y crystals are of high crystallinity. The 3D reciprocal lattice reconstructed from the 3D-RED data shows that the particle contains two sets of crystal lattices of zeolite Y, indicating the presence of twinning (Figure 1c). The orientation relationship between the twin components as well as their orientations in relation to the particle could be deduced. The tomogram reconstructed from the ET images shows clearly that uniformly-sized mesopores are distributed throughout the crystal (Figure 1d). The pore architecture and the connectivity of the mesopores are intuitively illustrated from the reconstructed structure model of electron tomography (Figure 1d).

[1] JY Ying and J Garcia-Martinez, US20050239634 patent (2005).

[2] KH Li et al, ChemCatChem 6 (2014) p.46.

[3] J Zecevic et al, Angew. Chem., Int. Ed. 51 (2012) p.4213.

[4] W Wan et al, J. Appl. Crystallogr. 46 (2013) p.1863.

[5] J Garcia-Martinez et al., ChemCatChem (2014) DOI: 10.1002/cctc.201402499.

Acknowledgement: The project is partly (ET and RED work) supported by the Swedish Research Council (VR), the Swedish Governmental Agency for Innovation Systems (VINNOVA), and the Knut & Alice Wallenberg Foundation through the project grant 3DEM-NATUR. The EM facility was supported by the Knut and Alice Wallenberg Foundation.

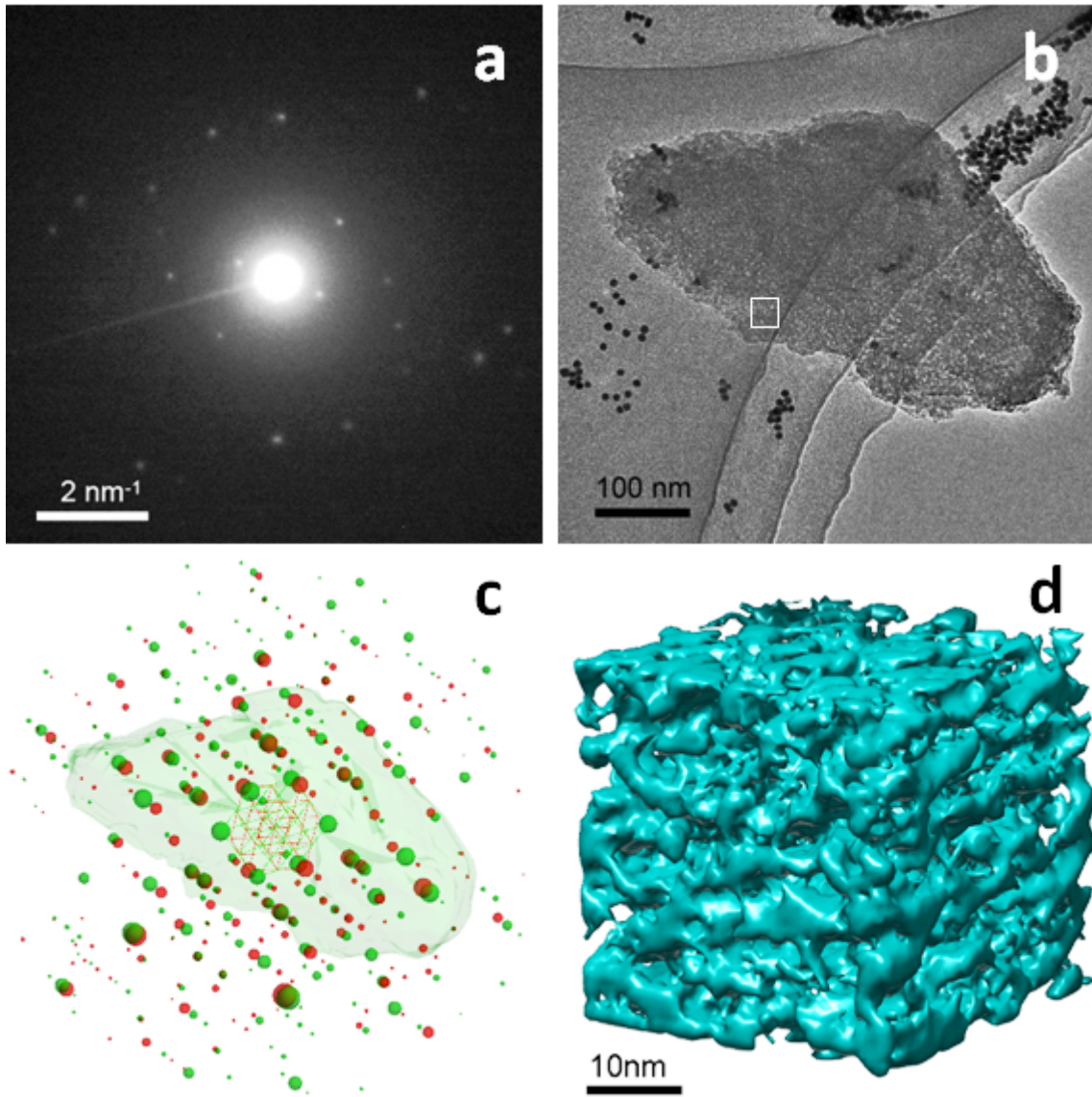


Fig. 1: (a) An ED frame in the RED data and (b) the corresponding image in the ET series. (c) Reconstructed 3D reciprocal lattices with the 3D morphology superimposed. RED data shows that the particle has two twin domains (lattices shown in red and green, respectively) sharing a [111] axis. (d) part of the tomogram from the area marked in (b).

MS-12. Magnetic, superconducting, ferroelectric and multiferroic materials

Type of presentation: Poster

MS-12-P-6114 Scanning electron microscopy and energy dispersive spectroscopy to study the nanomagnetism in minerals

Soares J. M.¹, de Araújo J. H.²

¹University State of Rio Grande do Norte, Mossoro, Brazil, ²University Federal of Rio Grande do Norte, Natal, Brazil

Email of the presenting author: joaomsoares@gmail.com

The Ilmenite-Hematite series can exist in the form of solid solution and of exsolution (separated phases). Occurrences of high magnetic remanence in rocks containing such exsolutions have been known for decades [1], and were recently the subject of intense debate [2-4]. We present results of magnetic measurements, Mössbauer spectroscopy, scanning electron microscopy (SEM) and energy dispersive spectroscopy (EDS) in samples of rocks with intrusive exsolutions of Ilmenite-Hematite series. The strong remanence and high coercivity observed in these samples can not be explained only by the individual properties of the present phases. The X-ray diffraction pattern shows two predominant phases in the sample, identified as Hematite, and Ilmenite. We also identified a small quantity of Magnetite (approximately 5%) in the sample. The hysteresis curve (Fig. 1) shows a coercive field of 35.6 mT, a saturation magnetization (M_s) of 24.5 A/m and one remanent magnetization (M_r) of 5.5 A/m. The coercive field (H_c) is very high for magnetite or any natural ferrite. The M_r/M_s ratio is 22.5%, higher than expected for the Ilmenite-Hematite solid solution value. The Mössbauer spectrum (MS) of this sample (Fig. 2) can be fitted with two sextet attributed to Hematite (63%), one Fe²⁺-doublet assigned to Ilmenite (22%), one Fe³⁺-doublet (3%), two sextets (7%) that can be attributed to Magnetite and one typical Fe²⁺ sextet still unidentified. At room temperature Hematite is antiferromagnetic and ilmenite is paramagnetic, apparently these minerals could not explain the magnetic behavior of this sample, and then we might think that such behavior should be attributed to magnetite. However, the small percentage of magnetite in the samples is insufficient to explain the values shown by magnetic measurements. Figures 3 and 4 shows SEM micrograph and EDS scan, where we can clearly see lamellae of Ilmenite in Hematite matrix. Due to the nanometric nature of these lamellae, an interaction between the Fe³⁺ in hematite and ilmenite Fe²⁺ is possible in the interface [2-4]. So the ilmenite Fe²⁺ who participate in this interaction are magnetically coupled, so having a hyperfine field. This mechanism explains why on the MS there are two non-equivalent sites for hematite and the unidentified Fe²⁺ sextet that can be attributed to Fe²⁺ in Ilmenite who participated in the magnetic coupling at the interface with hematite.

1 Y. Ishikawa and S. Akimoto, J. Phys. Soc. Jpn 13, 1298 (1958).

2 P. Robinson, R. J. Harrison, S.A. McEnroe, and R.B. Hargraves, Nature 418, 517 (2002).

3 T. Kasama, S.A. McEnroe, N. Ozaki, T. Kogure, and A. Putnis, Earth Planet. Sci. Lett. 224, 461 (2004).

4 P. Robinson, S.A. McEnroe, K. Fabian, R.J. Harrison, C.I. Thomas, and H. Mukai, Geophys. J. Int. 196, 1375 (2014).

Acknowledgement: We thanks to CNPq and Capes brazilan agencies and Shimadzu do Brasil company.

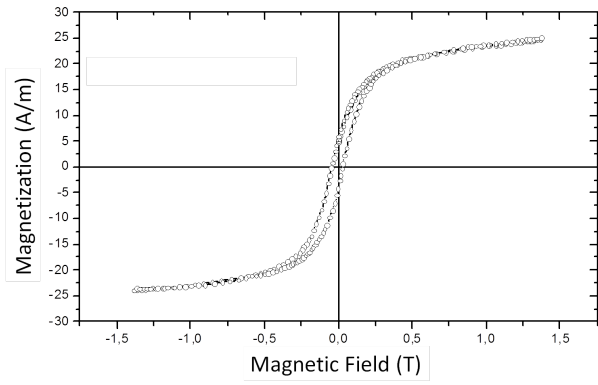


Fig. 1: Magnetization as a function of magnetic field measured at room temperature.

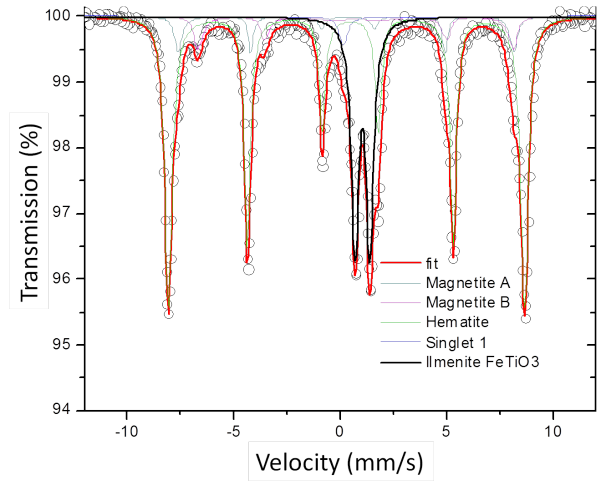


Fig. 2: Mössbauer spectrum recorded at room temperature.

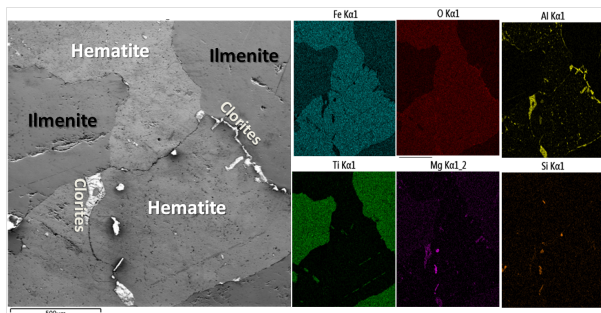


Fig. 3: SEM micrograph and EDS scan of a polished surface of sample.

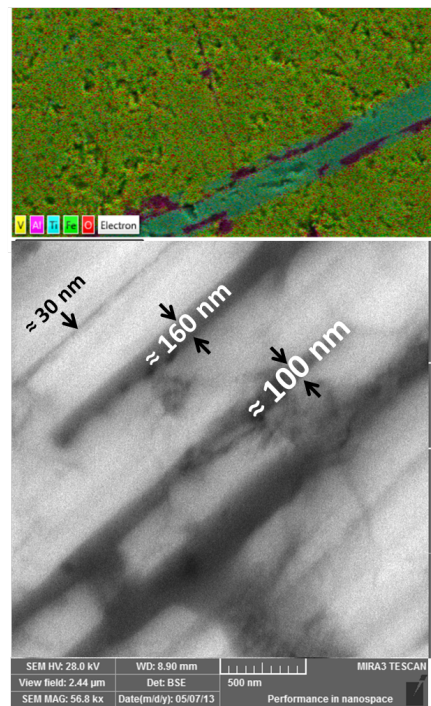


Fig. 4: EDS scan and SEM high resolution micrography of a surface of sample.

MS-14. Energy-related materials

Type of presentation: Poster

MS-14-P-6116 Ex-situ TEM analysis on extra capacities of SnO₂ lithium-ion battery anode material

Lee S. Y.¹, Park K. Y.¹, Kim W. S.¹, Hong S. H.¹, Kang K.¹, Kim M.¹

¹Department of Materials Science and Engineering, Seoul National University, Seoul, Republic of Korea

Email of the presenting author: syasms07@snu.ac.kr

Having high energy densities, lithium ion batteries are widely used and still promising for large electrical energy storage. Tin oxide (SnO₂) anode has been thought as an attractive anode candidate in that they have twice larger theoretical specific capacities than generally used graphite anode. SnO₂ anode is known that it first undergoes irreversible conversion reaction which forms Sn metal and lithium oxide (Li₂O) and then the rechargeable battery is operated by reversible alloying reaction between Sn metal and lithium ions, which can store 4.4 Li per SnO₂.^[1] However, there is still a lack of understanding on the reaction mechanism of tin oxide. The first conversion reaction is generally considered as irreversible, but some researchers posed the possibility of its partial reversibility.^[2] Furthermore, there has been a debate on additional specific capacities exceeding the theoretical value in most of metal oxide anodes. Therefore, it is simply believed that the extra capacities of SnO₂ anode come from the partial reversibility of conversion reaction. On the evidence of NMR studies of ruthenium oxide (RuO₂) material, Hu et al. recently attributed the origin of extra capacities in metal oxide anode to reversible reaction of lithium hydroxide (LiOH) which was first formed by electrolyte decomposition.^[3] But it still does not give an explanation of SnO₂ anode because RuO₂ anode is known to undergo the conversion reaction reversibly in contrast with SnO₂ anode.

Therefore, we traced single SnO₂ particle by ex-situ transmission electron microscopy (TEM) investigation. Having spatial resolution and facilitating nano-area investigation, TEM is perfect to resolve the debates. SnO₂ particles dispersed on TEM grid were dis/charged directly in real battery cell and they were observed on each of major reaction states, which are expressed as Roman numerals in Fig. 1. Fig.2 shows an example of traced SnO₂ particles. We analyzed phase changes of the particles corresponding to the images by selected area electron diffraction (SAED) patterns (Fig. 3). As expressed in Fig. 3, we could identify changes of polymeric layers on the controversial stages and same phases of SnO₂ pristine materials did not appear again. It might indicate that the SnO₂ particles cannot be re-oxidized to the same phases as initial state and the reaction of polymeric layers formed on the surfaces of the particles can influence the capacities of SnO₂ anode. By this robust technique, we could identify the reaction related with the extra capacities of SnO₂ lithium-ion battery anode which has long been controversial.

[1] I.A. Courtney et al., J. Electrochem. Soc., 144(6), 2045-2052(1997).

[2] J. Shiva et al., Chem. Eur. J., 18, 4489-4494(2012).

[3] Y.-Y. Hu et al., Nat. Mater., 12, 1130-1136(2013).

Acknowledgement: This work was supported by the National Research Foundation of Korea (NRF) grant funded by the Korea government (MSIP) (NRF 2013034238)

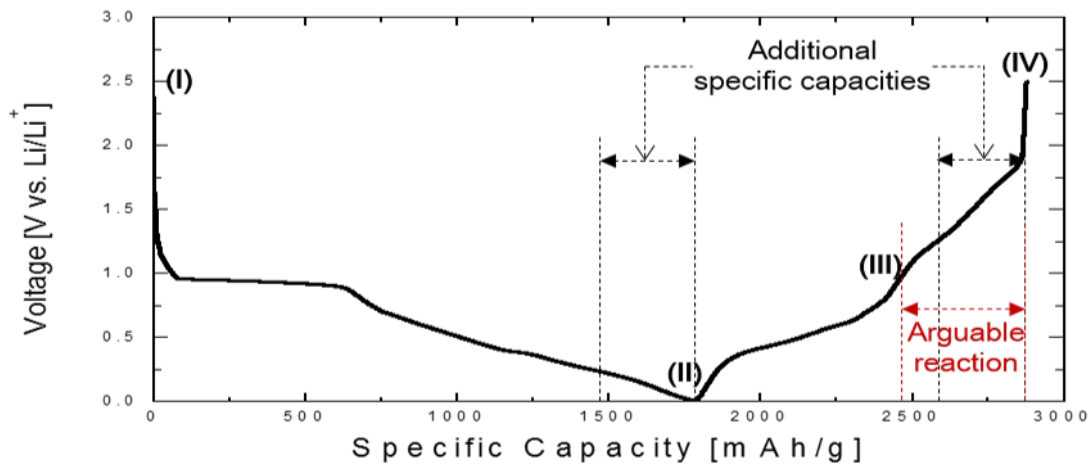


Fig. 1: Voltage vs. specific capacity profiles of SnO₂/Li battery at a current rate of 20mA/g. Additional specific capacities and arguable reaction regions are expressed on the graph. Roman numerals in parentheses expressed as (I) to (IV) indicate the investigated states by ex-situ TEM research.

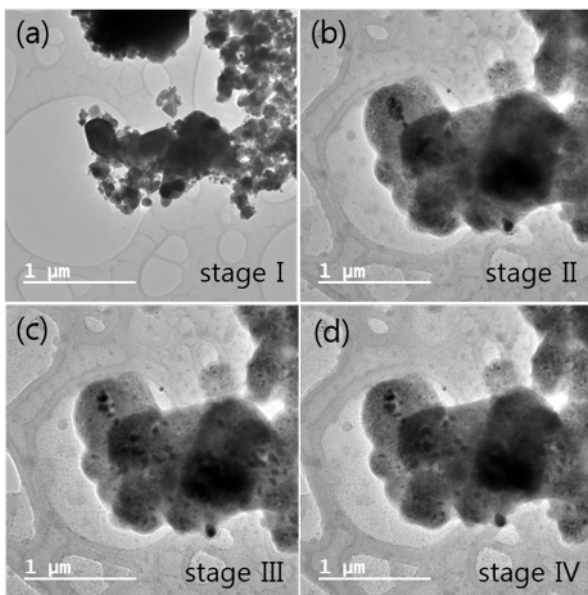


Fig. 2: TEM images of traced SnO₂ particles at (a) stage I, (b) stage II, (c) stage III, and (d) stage IV corresponding to the states indicated in Fig. 1.

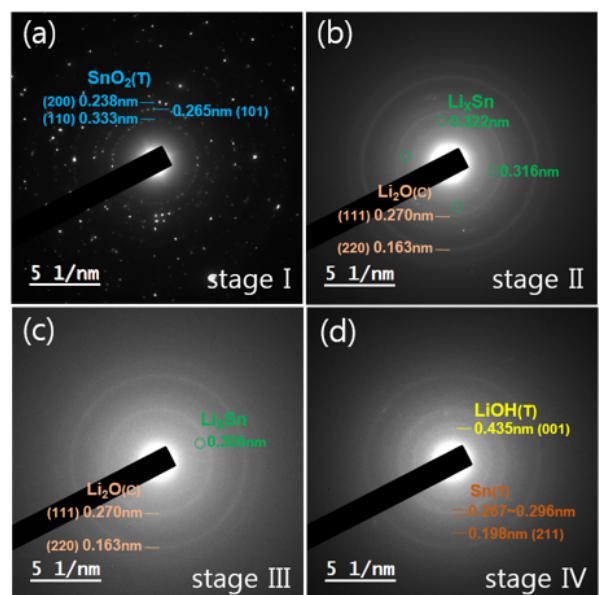


Fig. 3: Corresponding SAED patterns of Fig. (a) 2a (stage I), (b) 2b (stage II), (c) 2c (stage III), (d) 2d (stage IV). The indexed phases, miller indices and d-spacing of planes are marked on each pattern.

Type of presentation: Poster

MS-14-P-6129 AFM and SEM studies on high fluence, low energy iodine implantation in 6H-SiC

Kuhudzai R. J.¹, Malherbe J. B.¹, van der Berg N. G.¹, Buys A. V.²

¹Physics Department University of Pretoria, ²Laboratory for Microscopy and Microanalysis, University of Pretoria, South Africa

Email of the presenting author: joeykuhu@yahoo.com

The study of ion beam modification of surfaces has increasingly become an integral part of the characterisation of nuclear materials. The effect of a relatively high fluence of iodine ions on the surface of 6H-SiC has been investigated. The contribution of vacuum annealing on the evolution of the surface morphology was also studied. Vacuum annealing was performed at 350 °C, 900 °C, 1200 °C and 1500 °C. Atomic force microscopy (AFM) and high resolution scanning electron microscopy (FEG SEM) were employed to analyse the surface microstructure. Images taken from the as-implanted samples revealed the development of cone-like structures (protrusions) on the surface, indicating some form of sputtering process occurred during implantation. An increase in the roughness was also observed after implantation. Root mean square roughness (rms) values of the as-received virgin 6H-SiC was found to be approximately 0.5 nm. After implantation the roughness increased to about 5.0 nm due to sputtering. This sputtering was accompanied by the amorphisation of the near surface region. Annealing at 1200 °C causes recrystallisation of the SiC surface and an increase in the surface roughness. Rutherford backscattering spectroscopy (RBS) studies of the same samples revealed that diffusion of the ion implanted iodine was also observed after the samples were sequentially annealed for periods of up to 5 hours annealing up to 1200 °C. Roughness decreases after 1500 °C due to thermal etching and decomposition of SiC. High Resolution SEM images show that the sample surfaces were now covered by a carbon layer at the higher annealing temperatures due to the sublimation of silicon at these temperatures leaving behind a layer of carbon on the surface. This graphitisation of the surface was confirmed by RBS measurements.

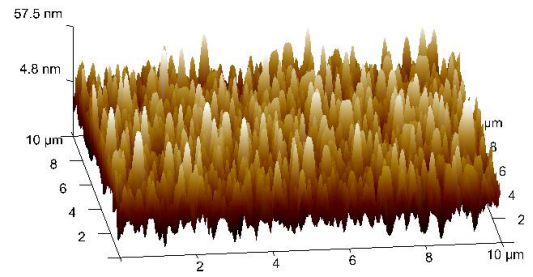
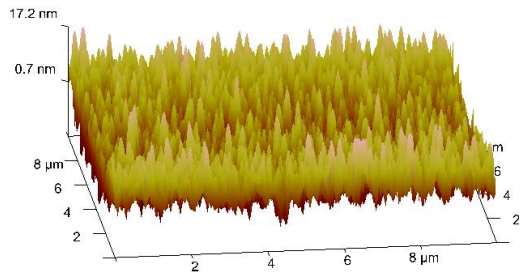


Fig. 1: 3D-AFM image of the as-implanted 6H-SiC implanted with iodine ions. The fluence was $2 \times 10^{17} \text{ cm}^{-2}$. Fig. 2: 3D-AFM image of the iodine implanted sample after annealing at 1200 °C for 5 hours.

LS-1. Live imaging of cells, tissues and organs

Type of presentation: Poster

LS-1-P-6077 The importance of PTEN-PI3K-AKT Signaling Pathway on Invasive Breast Cancer Cell Lines MDA-MB-231

Onal T.¹, Ozgul M.¹, Temel M.¹, Celik M.¹, Turkoz Uluer E.¹, Ozbilgin K.¹, Inan S.¹

¹Celal Bayar University, Faculty of Medicine, Dept. of Histology&Embryology, Manisa, Turkey

Email of the presenting author: drmustafacelik@gmail.com

Breast cancer in women, is the second most common cancer after lung cancer. MDA-MB-231 cells which are isolated from pleural effusion of women who are diagnosed as invasive epithelial breast adenocarcinoma is a useful model for studying in vitro treatments of metastatic breast cancer. These cell lines are also used for modelling cell migration, proliferation and invasion of breast cancer. PTEN-PI3K-AKT signaling pathway plays a role on cell proliferation, growth, metabolism and apoptosis. The aim of this study was to determine the effects of Rapamycine which is mTORC1 inhibitor and PTEN-PI3K-AKT pathway using indirect immunohistochemistry method on invasive MDA-MB 231 breast cancer cell lines.

MDA-MB-231 cells were cultured in RPMI-1640 medium; containing 10% fetal bovine serum, 1% L-glutamine and 1% penicilline/streptomycine solution in a humidity incubator at 37°C, containing 5% CO₂. The study was carried out as the control group (MDA-MB-231 cells) and the Rapamycine group (MDA-MB-231 + IC₅₀ Rapamycine). The effects of Rapamycine on MDA-MB 231 cells were evaluated at 24th hours. The cells were fixed with 4% paraformaldehyde and prepared for immunohistochemical analysis with anti-PTEN, anti-PI3K and anti-AKT by using indirect avidin-biotin peroxidase method. Positively stained cells were counted and the H-score was determined according to the severity of immunoreactivity which were evaluated minimal (1), moderate (2), strong (3) and very strong (4).The results were compared with One way-ANOVA statistical test.

The immunoreactivity of anti-PI3K (Figure 1) and anti-AKT (Figure 2) antibodies were observed as moderate/strong (2/3) and the immunoreactivity of anti-PTEN was observed as strong/very strong (3/4) in the Control group. Decreased immunoreactivities were detected on anti-PI3K (Figure 3) and anti-AKT (Figure 4) on MDA-MB-231 cells in Rapamycine treated group, compared with the Control group (p<0.05). The immunorecativity of anti-PTEN was observed as unchanged (p>0.05).

In this study, Rapamycine has been shown to be effective on PI3K-AKT signaling pathway on invasive breast cancer cell lines MDA-MB-231. PTEN is a dual effective protein/lipid phosphatase which plays an important role in human cancer because of the decreased activity caused by mutation, deletion and methylation. Several cellular systems have different tumor growth properties such as Ras, PIP3; so it was thought that mTOR inhibitors might be beneficial for additional therapy and new drug development on cancer treatment.

References :

1. Figlin RA, et al.. JNCCN 2008; 6: 1-20
2. Zhang HY, et al.. Oncology Letters 2013; 6: 161-168
3. Zaytseva YY, et al.. Cancer Letters 2012; 319: 1-7

Acknowledgement: The material used in this project was funded by Scientific Research Committe of Celal Bayar University (Project Number: 2011-038)

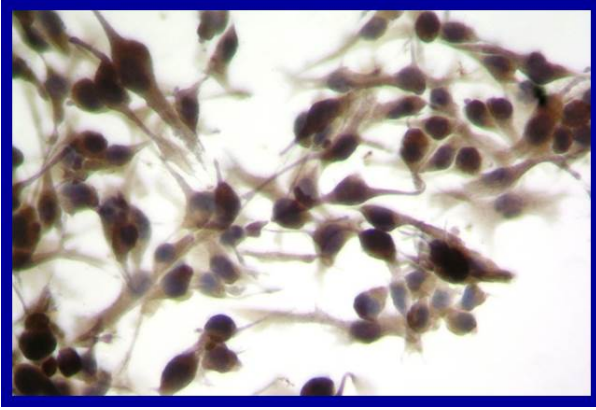


Fig. 1: Immunoreactivity of anti-PI3K on MDA-MB 231 cells in the Control group.

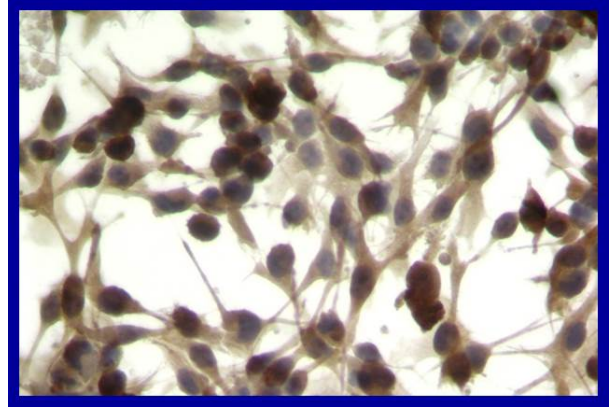


Fig. 2: Immunoreactivity of anti-AKT on MDA-MB 231 cells in the Control group.

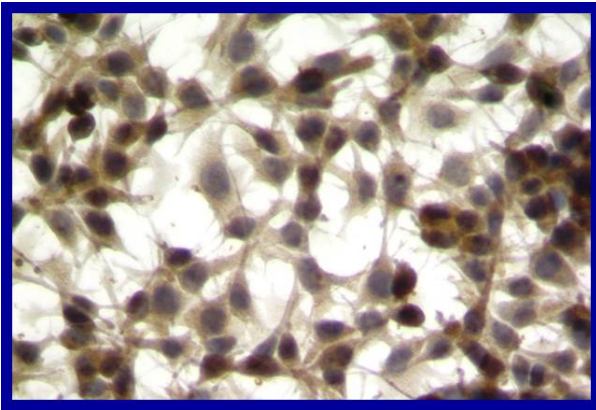


Fig. 3: Immunoreactivity of anti-PI3K on MDA-MB 231 cells in the Rapamycin-treated group.

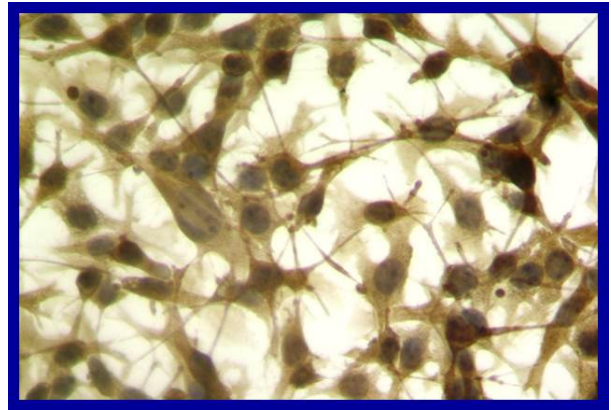


Fig. 4: Immunoreactivity of anti-AKT on MDA-MB 231 cells in the Rapamycin-treated group.

Type of presentation: Poster

LS-1-P-6103 The involvement of Nitric Oxide in breast cancer pathogenesis. Image based investigation at the resolution of single cell clusters (spheroids)

Shafran Y.¹, Zurgil N.¹, Sobolev M.¹, Moshkov S.¹, Ravid O.¹, Afrimzon E.¹, Shainberg A.², Deutsch M.¹

¹The Biophysical Interdisciplinary Schottenstein Center for the Research and Technology of the Cellome, Bar Ilan University, Israel, ²The Mina and Everard Goodman Faculty of Life Sciences, Bar Ilan University, Israel

Email of the presenting author: yana.shafran@gmail.com

Background

Nitric oxide (NO), a short-lived messenger, modulates a variety of physiological functions which are important for tumor survival and propagation. NO has been reported to have a dual effects on tumor depending on many factors such as tissue type, microenvironment and NO concentration. Recently NO releasing drugs have come into the focus for cancer treatment. Breast cancer is the most common cancer in women. The role of NO in breast cancer is still poorly understood. Study of NO influence on breast tumor could lead to the development of new approaches and strategies for the effective treatment of breast cancer.

Method

The current study presents a microscopy live cell imaging technology for the kinetic, real time measurements of the formation and growth of MCF7 (estrogen receptor positive breast cancer cell line) 3D structures (spheroids) treated by different concentrations of exogenous NO. Spheroids have been recognized as an advanced model for in vitro cancer study as compared to monolayer cell growth.

Spheroids are formed in a unique culturing device; a Petri dish equipped with a glass bottom which is embedded with an array of UV adhesive microchambers (MCs). The MCs are coated with polyHEMA in order to prevent cell adhesion to its surface.

Results

After cell loading the spheroid assembly from the individual cells was monitored. The location of each spheroid is preserved in the same MC throughout its growth, NO-donor treatment and imaging.

Kinetic probe free image analysis of spheroid formation and growth showed a significant difference in formation rate and morphology of the spheroids cultured in the presence of estrogen (E2) as compared to its absence. Moreover, different NO concentrations showed biphasic effect. The ratio between individual spheroid volume after and before treatment (the growth rate) was found to be major parameter which reflects the spheroid biophysical change. High NO concentration (0.1 μ M) inhibits growth as compared to the control spheroids ($P < 0.001$), while low exogenous NO level (1 nM) causes enhanced growth ($P = 0.001$). No influence of NO on spheroid growth ratio was observed when E2 was present in the culture media.

Fluorescence microscopy of apoptotic, mitochondria membrane potential, and NO markers showed that high NO concentration promotes apoptosis of the E2 deprived spheroids.

Conclusions

We have developed a MCs device suitable for both probe free and fluorescent microscopy study of cancer spheroids formation, culturing and treatment.

The ability to measure the growth rate of the individual spheroid eliminates the noise caused by the heterogeneity of the spheroid population.

MC methodology could help to understand the mechanisms of NO action on breast cancer and to design novel therapeutic approaches.

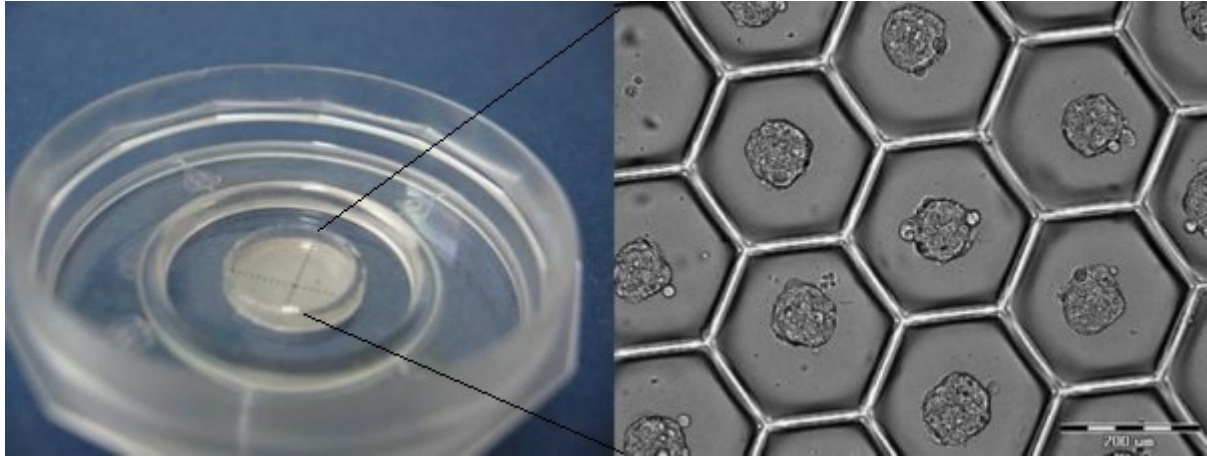


Fig. 1: MCF7 spheroids were grown in the microchambers of the Petri dish device for 72h

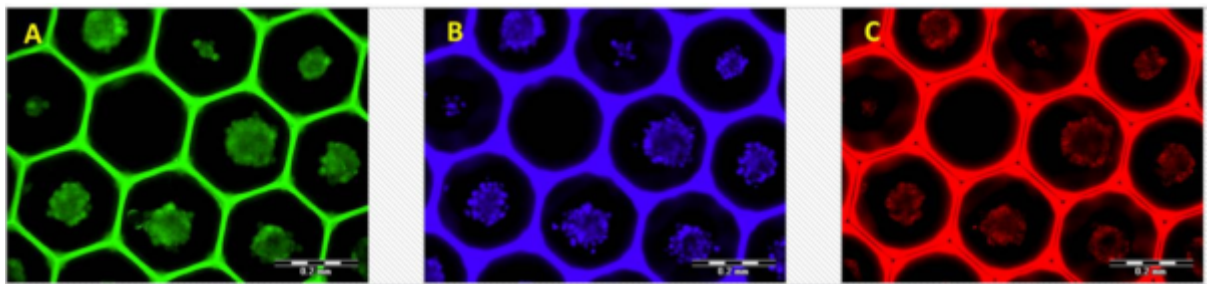


Fig. 2: Triple fluorescence staining of MCF7 spheroids: A- DAF2 indicates endogenous NO level, B- shows clear Hoechst staining of the cells' nuclei and C- mitochondrial membrane potential evaluated by TMRM

LS-2. Structure and function of cells and organelles

Type of presentation: Poster

LS-2-P-6117 Multi-protein assemblies underlie the mesoscale organization of the plasma membrane

Saka S. K.¹, Honigmann A.², Eggeling C.³, Hell S. W.², Lang T.⁴, Rizzoli S. O.¹

¹University of Goettingen Medical Centre, Goettingen, Germany, ²Max Planck Institute for Biophysical Chemistry, Goettingen, Germany, ³Weatherall Institute of Molecular Medicine, Oxford, UK, ⁴Life and Medical Sciences (LIMES) Institute, University of Bonn, Bonn, Germany

Email of the presenting author: ssaka@gwdg.de

Most proteins have uneven distributions in the plasma membrane¹. This may be caused by mechanisms specific to each protein, or may be a consequence of a general pattern that affects the distribution of all membrane proteins. To find out if a general mechanism exists behind this observation, we introduced several imaging approaches that aim to investigate all proteins in the plasma membrane simultaneously rather than focusing on interactions of individual protein species. This was achieved by large-scale metabolic labeling of proteins in mammalian cells through extended incorporation of non-canonical amino acid analogues, followed by fluorescent tagging via click chemistry². By combining this direct labeling method with super-resolution stimulated emission depletion (STED) microscopy, we studied the protein patterning in plasma membranes of living cells, as well as in membrane sheets. We found that a general mosaic-like pattern governs the protein organization³. Multiple proteins were heterogeneously gathered into protein-rich domains surrounded by a protein-poor background. We termed these long-lived high-abundance domains "protein assemblies" and examined the contributions of different factors to their formation and maintenance. We identified cholesterol as the main organizer of the assembly pattern and the actin cytoskeleton as a secondary factor that borders and separates the assemblies. To understand the relation of this mesoscale arrangement to the nanoclusters of individual protein species, we analyzed distributions of specific proteins with respect to the protein assemblies. All of the specific proteins we analyzed were enriched in the assemblies, but they displayed differential enrichment profiles. Many proteins were preferentially located in particular areas within the assemblies, such as their edges or centers. Functionally related protein groups showed similar preferences, suggesting that functional protein-protein interactions create specialized subdomains within the assemblies. We conclude that the assemblies constitute a fundamental principle of the mesoscale membrane organization, which affects the nanoscale patterning of most membrane proteins, and possibly also their activity.

References:

1. Lang T & Rizzoli SO. Membrane protein clusters at nanoscale resolution: more than pretty pictures. *Physiology* 25, 116-124 (2010).
2. Dieterich DC et al. In situ visualization and dynamics of newly synthesized proteins in rat hippocampal neurons. *Nat Neurosci* 13, 897-905 (2010).
3. Saka SK et al. Multi-protein assemblies underlie the mesoscale organization of the plasma membrane. *Nat Commun* 5, 4509 (2014).

Acknowledgement: SKS was supported by a Boehringer Ingelheim Fonds PhD Fellowship and by the Dorothea Schloezer Program of University of Goettingen. The work was supported by ERC grants FP7 Starting Grant Nanomap and ERC-2013-CoG NeuroMolAnatomy and by DFG grants LA 1272/3-1/RI 1967/3-1 and RI 1967/2-1 to SOR and TL.

Type of presentation: Poster

LS-2-P-6118 SEM/FIB of cell-interface in 3D-electrodes

Panaitov G.¹, Santoro F.¹, Neumann E.¹, Offenhäusser A.¹

¹Peter Grünberg Institute for Biosensorics (PGI-8), Research Center Jülich, Germany

Email of the presenting author: g.panaitov@fz-juelich.de

Recordings/stimulations of neurone cells in Multi-Electrode Arrays (MEA) depend on quality of the interface between the cells and the surface of the electrodes. In order enhance the electrical signal transfer the cell contact area should be increased and cleft between cells and contact electrodes should be minimised.

For improvement of cell-device adhesion, we apply micro-structural modification of the surface of the MEA device. The 3-dimensional gold micro-spines have been fabricated on the MEA electrodes and the cells (HL1, rat neuron) have been grown at the contact area.

We applied SEM and FIB techniques for characterisation of the interface between the cells and gold micro-spines. The bio-samples have been prepared by standard chemical fixation and critical point drying. FIB cross-sectioning of the cell/electrode area shows that the structure of the interface is strongly dependent on dimensions of the gold spines and position of the spine relative to the cell body. We found that HL-1 cells prefer to engulf gold pillars contacting to the central part of the cell. We assume that the engulfed pillars are stabilized by an actin network in the center of the cell, while this network is in a much more dynamic state at the edge of the cell, driving the filopodia on the planar substrate /1/.

/1/ Francesca Santoro, Sabyasachi Dasgupta, Jan Schnitker, Thorsten Auth, Elmar Neumann, Gregory

Panaitov, Gerhard Gompfer, Andreas Offenhäusser. Interfacing Electrogenic Cells with 3D Nanoelectrodes: Position, Shape, and Size Matter. ACS Nano, 2014, 8 (7), pp 6713–6723

LS-3. Super-resolution localization of molecular targets and macromolecular complexes

Type of presentation: Poster

LS-3-P-6085 3D structured illumination superresolution microscopy (3D-SIM) for studying the synaptonemal complex

Wright G. D.¹, Horn H. F.¹, Wong E. S.¹, Stewart C. L.¹, Burke B.¹

¹Institute of Medical Biology, A*STAR, Singapore

Email of the presenting author: graham.wright@imb.a-star.edu.sg

3D structured illumination microscopy (3D-SIM) enables microscopy at finer resolution than can be achieved with standard optical microscopes. The diffraction limit has meant that, until relatively recently, lateral resolution has been limited to ~250nm at best. By utilising the moiré fringes produced from illuminating the sample with a structured pattern, higher frequency information from the sample can be collected and, with subsequent computational processing, a resolution of ~120nm can be attained. At the Institute of Medical Biology Microscopy Unit this technique, using the DeltaVision OMX, is being applied to cell and developmental biology research. Here we will present results from our research into chromosomal pairing and the synaptonemal complex formation during meiosis.

Chromosome pairing is an essential meiotic event that ensures faithful haploidization and recombination of the genome. Pairing of homologous chromosomes is facilitated by telomere-led chromosome movements and formation of a meiotic bouquet, where telomeres cluster to one pole of the nucleus. In metazoans, telomere clustering is dynein and microtubule dependent and requires Sun1, an inner nuclear membrane protein. Here we provide a functional analysis of KASH5, a mammalian dynein-binding protein of the outer nuclear membrane that forms a meiotic complex with Sun1. Mice deficient in KASH5 are infertile. Males display meiotic arrest in which pairing of homologous chromosomes fails. These findings demonstrate that telomere attachment to the nuclear envelope is insufficient to promote pairing and that telomere attachment sites must be coupled to cytoplasmic dynein and the microtubule system to ensure meiotic progression.

Type of presentation: Poster

LS-3-P-6108 3D Super Resolution Microscopy: Multi-plane Imaging

Lo Schiavo V.¹, Guastamacchia M.¹, Dalgarno P. A.², Webb S. E.¹, Martin-Fernandez M.¹

¹Science and Technology Facilities, Rutherford Appleton Laboratory, Central Laser Facility, Harwell Campus, Oxfordshire, OX11 0FA, UK , ²Institute of Biological Chemistry, Biophysics and Bioengineering/SUPA, School of Engineering and Physical Science, Heriot-Watt University Edinburgh, EH14 4AS, UK

Email of the presenting author: valentina.lo-schiavo@stfc.ac.uk

High resolution optical microscopy is an important tool in cell biology as it offers a non-invasive and non-destructive diagnostic technique. Such technique can be used to image biological structures inside a cell on a sub-micron scale and in 3D. Microscopy available for cell biology has experienced considerable advances in the last decades. However, all the current techniques (i.e. confocal 3D imaging, wide-field, super-resolution microscopy) are limited in their ability to extract information in real-time and in 3D.

We have developed a method for real-time 3D imaging and tracking which involves the recording of images from different object planes simultaneously. We can achieve this by adding a customised diffractive optical element (DOE) to the camera port of a standard microscope. The DOE consists of an image-relay system with a distorted diffraction grating and lens which allow us to image multiple object z-planes simultaneously onto a single image plane [1]. The separation of the object-planes ranges from zero to a few tens of microns, ideal for applications in cell biology. Such separation is determined by the magnification of the microscope, the properties of the grating and the focal length of the relay lens. The diffraction grating will have a quadratic distortion of the lines, similar to an off-axis Fresnel lens, producing positive focusing power in the positive diffraction orders, negative focusing power in the negative orders and unchanging the zeroth order beam.

The DOE produces then three images on the camera, associated with diffraction orders $m=-1$, 0, and $+1$. Simultaneous multi-plane images can be taken using several imaging modes, e.g. bright-field, fluorescence, phase-contrast, etc. Single particles can be tracked and localized with a 10 nm axial accuracy through a full cell ($\sim 10 \mu\text{m}$ depth) using 9 planes (by employing 2 mutually perpendicular gratings) and modest plane separations [2]. We are employing the DOE on super-resolution microscopes in order to resolve sub-nm structures with high voxel precision. However, drawbacks related to this method arise from chromatic aberrations. Indeed, in order to limit such distortions the DOE-based technique is narrow band, limiting the incident spectral bandwidth, restricting photon flux and prohibiting application to multiple-colour imaging.

In conclusion, the above approach offers all of the advantages of multi-plane imaging using beam-splitters and multiple cameras with the additional advantages of simplicity, low cost and full compatibility with commercial microscopes.

[1] Paul A. Dalgarno et al., Optics Express, 2010

[2] Heather I.C. Dalgarno et al., J. R. Soc. Interface, 2011

Type of presentation: Poster

LS-3-P-6119 Polarized Emission of CdSe Nanorods to Probe Three-Dimensional Structural Dynamics of Single Molecular Motor Proteins

Dadosh T.¹, Lippert L.², Diroll B. T.³, Murray C. B.³, Goladman Y. E.²

¹Department of Chemical Research Support, Weizmann Institute of Science, Israel,
²Pennsylvania Muscle Institute, School of Medicine, University of Pennsylvania, Philadelphia, PA, USA, ³Department of Materials Science and Engineering, University of Pennsylvania, Philadelphia, PA, USA

Email of the presenting author: tali.dadosh@weizmann.ac.il

The ubiquitous nature of motility in living cells and the structural homologies among motor proteins give fundamental research on molecular motors wide impact. The present work seeks to apply novel and powerful approaches for studying the structural changes of motor proteins during their movement along actin filaments. Labeling motor proteins with semi-conducting, highly fluorescent CdSe / CdS nanorods (20 nm in length) allows determination of the position and the three-dimensional orientation of single motor proteins while walking on actin filaments.

The nanorods of CdSe core and CdS shell, functionalized with streptavidin, were attached to myosin V and myosin VI via a biotin linker. The carried nanorod does not inhibit the function of the motor protein as it moves along the filaments, as the measured velocity of the protein and its average step size is similar to the values reported in the literature.

The polarized emission of the attached nanorods is divided into four different polarization angles and projected onto an EMCCD camera. The three dimensional orientation of the nanorods is then calculated from the relative intensity of the emission at the different polarization angles.

The emission of nanorods attached to the c-terminus of truncated myosin V and myosin VI constructs shows discrete angle changes of the probe during processive stepping, which indicate that the motors rotate as they step along actin filaments in a discrete manner. This polarized TIRF microscopy can provide further understanding of the dynamic processes of single molecule systems.

Acknowledgement: Supported by NIH Structural Biology Training Grant, and NIH PPG GM087253.

LS-4. Structure of macromolecules and macromolecular complexes

Type of presentation: Poster

LS-4-P-6130 Structural characterization of Photosystem II supercomplex from Norway spruce indicates a different organization of light-harvesting antenna compared to flowering plants

Kouřil R.¹, Nosek L.¹, Ilík P.¹, Boekema E. J.²

¹Centre of the Region Haná for Biotechnological and Agricultural Research, Palacký University, Olomouc, Czech Republic 1, ²Department of Biophysical Chemistry, GBB, University of Groningen, The Netherlands 2

Email of the presenting author: roman.kouril@upol.cz

Plant Photosystem II is a large multiprotein complex, which catalyzes splitting of water molecules and reduction of plastoquinone necessary to transform sunlight into chemically bound energy. The supramolecular organization of the Photosystem II supercomplex in angiosperms (flowering plants), e.g. Arabidopsis, is known at 12Å resolution (Caffarri S. et al., Functional architecture of higher plant photosystem II supercomplexes. EMBO J 28: 3052-3063). It shows the location and the orientation of the Photosystem core complex and associated light harvesting complex, which is organized in heterotrimers composed of the Lhcb1-3 proteins and three monomers, Lhcb4 (CP29), Lhcb5 (CP26), and Lhcb6 (CP24). According to the frequency of occurrence of the heterotrimers, the three binding sites were designated "S", "M" and "L" (Strongly, Moderately, Loosely bound heterotrimer, respectively). However, structural information about the architecture of the Photosystem II supercomplex in gymnosperms is completely lacking. We isolated different forms of Photosystem II supercomplexes from young seedlings of Norway spruce (*Picea abies*) using high resolution clear-native electrophoresis. Structural analysis of negatively stained Photosystem II supercomplexes was performed using single particle electron microscopy and image analysis. Structural data indicate a different architecture of the light harvesting complex in spruce compared to Arabidopsis. The spruce PSII supercomplex lacks the minor antenna protein CP24. As a consequence of the CP24 absence, the M type of the heterotrimer of the light harvesting complex has different orientation in the spruce Photosystem II supercomplex, which has never been observed in flowering plants.

Acknowledgement: This work was supported by the Ministry of Education, Youth and Sports of the Czech Republic (grants No. ED0007/01/01 - Centre of the Region Haná for Biotechnological and Agricultural Research) and the Grant Agency of the Czech Republic (13-28093S/P501).

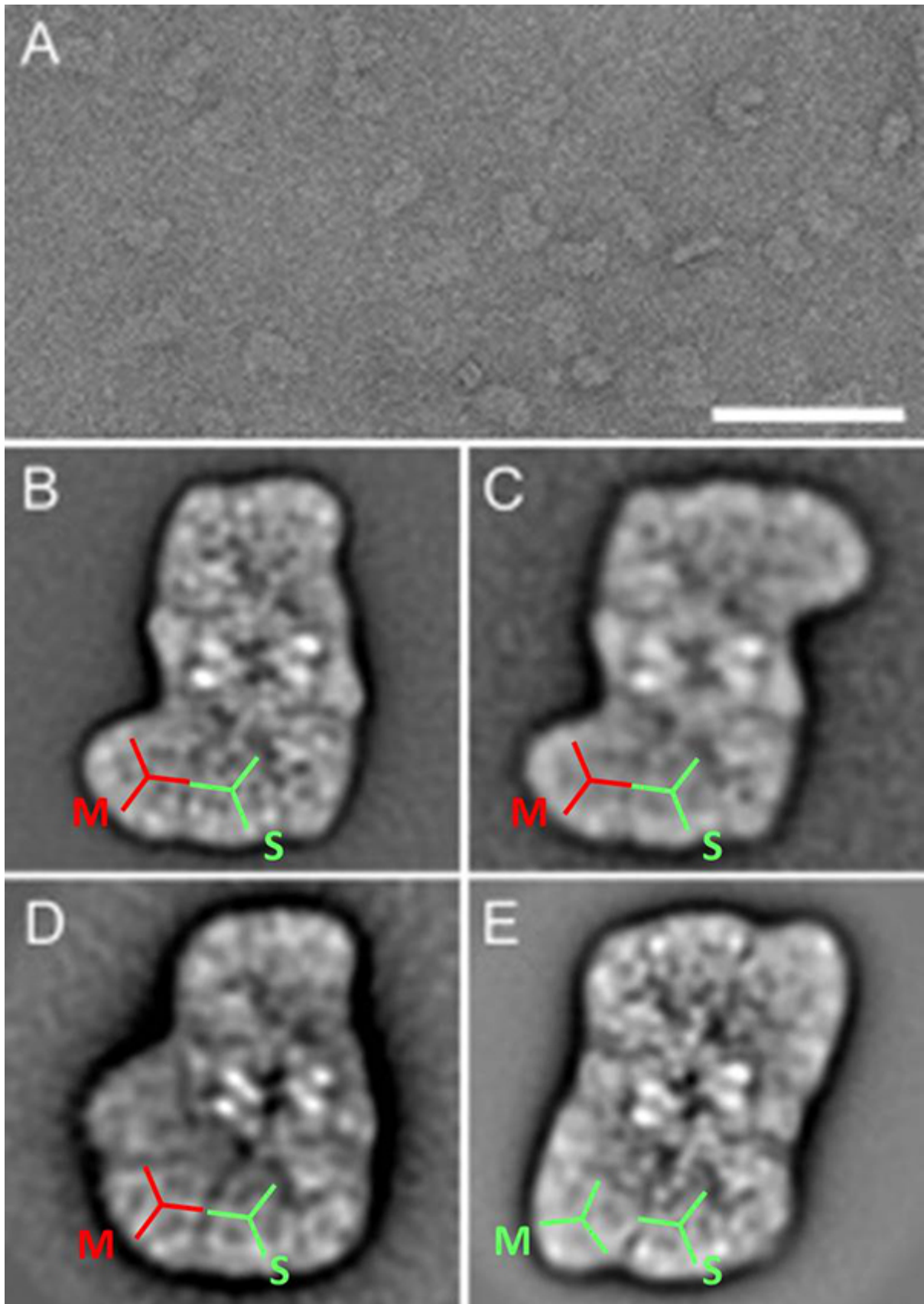


Fig. 1: A raw electron micrograph of a negatively stained specimen of the spruce PSII supercomplexes (scale 100 nm) (A). Comparison of PSII supercomplexes from spruce (B,C), *Chlamydomonas* (D) (adopted from Drop B. et al., JBC, 2014) and *Arabidopsis* (E) (adopted from Caffarri S. et al., EMBO J, 2009). Orientations of the S and M trimers are highlighted.

LS-6. Microbiology and virology

Type of presentation: Poster

LS-6-P-6121 Targeting Buried Features in a Resin-Embedded Mouse Cornea with Correlative X-ray and Electron Microscopy

Gelb J.^{1,2}, Park C.³, Beuerman R. W.⁴, Padmanabhan S.⁴, Lechner L.², Merkle A.²

¹San Jose State University, San Jose, CA, USA, ²Carl Zeiss X-ray Microscopy, Inc., Pleasanton, CA, USA, ³Carl Zeiss Pte. Ltd., Singapore, ⁴Singapore Eye Research Institute, Singapore

Email of the presenting author: jeff.gelb@zeiss.com

In the life sciences, one common practice is to embed specimens in resin prior to performing microscopic analysis. Resin represents a mechanically robust, yet optically transparent matrix for housing specimens, and is a time-tested carrier for optical imaging, physical sectioning, and electron microscopy. In order to capture the smallest features within a specimen in 2D, a scanning-electron microscope is typically employed; more recently, in-situ microtomes and focused ion beams have extended these high-resolution SEM investigations to three dimensions using a "slice and view" approach. Many biological specimens, however, are very large, and it may be difficult to identify specific regions of interest for high-resolution SEM analysis using 2D optical techniques alone. Furthermore, the destructive nature of slice-and-view 3D imaging techniques makes it impossible to view the 3D interior of a specimen and then localize for further characterization.

X-ray microscopy (XRM) is a modern characterization technique, capable of producing very high spatial resolutions (down to the 10s of nanometers) with a non-destructive imaging approach. Employing XRM, a large specimen may be imaged with sub-micron resolution while physically preserving the intact structure, resulting in a stack of virtual slices making up the 3D specimen volume. The data produced may be examined and smaller regions of interest identified for higher-resolution SEM analysis.

Here, we will present the results of imaging a pseudomonas bacteria infected mouse cornea, which was fixed with gluteraldehyde, stained with osmium tetroxide, and embedded in araldite resin. The resin-block specimen is imaged with XRM using sub-micron resolution and then transferred to the SEM for higher-resolution imaging using an automated correlative microscopy workflow. The XRM images reveal regions of the cornea that may contain bacteria, which is confirmed in 3D using FIB-SEM.

LS-14. Neuroscience

Type of presentation: Poster

LS-14-P-6123 Time-Dependent Changes Between Immature Neurons Contacting GABAergic Nerve Cells Using Double Immunogold Labeling in Wistar and GAERS rats

Cilingir O. T.¹, Gursoy D.¹, Moore C.², Meshul C. K.², Onat F.³, Sirvanci S.¹

¹Marmara University, School of Medicine, Department of Histology and Embryology, Istanbul, Turkey, ²Veterans Hospital/Portland and Oregon Health and Science University, Department of Behavioral Neuroscience and Pathology, Portland, USA, ³Marmara University, School of Medicine, Department of Pharmacology and Clinical Pharmacology, Istanbul, Turkey

Email of the presenting author: tugce.cilingir@marmara.edu.tr

Introduction: Neurogenesis occurs during the life-time period in two distinct areas of the adult brain; the subventricular zone (SVZ) of the lateral ventricles and the dentate gyrus (DG) of the hippocampus. Recent studies have shown that neurological disorders or injuries cause an increase in neurogenesis, however, a significant decrease occurs during ageing (1, 2). It is generally accepted that excessive GABA mediation plays an important role in absence epilepsy (3). To determine the effects of absence epilepsy on neurogenesis, we used an animal model of this disorder, genetic absence epilepsy rats from Strasbourg (GAERS), and used Wistar rats as control (4). Because neurogenesis is dependent on the age of animals, we tested both 21-day- and 3-month-old rats. In the present study, we examined whether newly born neural cells integrate into the local circuitry and synapse with GABAergic cells in both the epileptic and aged animals. Doublecortin (DCX), a marker of immature neurons, and GABA were identified together using double postembedding immunogold labelling at the electron microscopic level.

Materials and Methods: 21-day- and 3-month-old Wistar and GAERS rats were sacrificed by intracardiac perfusion fixation. Brains were removed and 300 µm-thick coronal vibratome sections were obtained and DG region was dissected. For immunocytochemical investigations, the tissues were embedded in epon. Ultrathin sections were obtained by using an ultramicrotome and double immunogold labeling was carried out with two different sized gold particles for localization of DCX and GABA.

Results: In all groups, DCX and GABA were seen co-localized in axon terminals, dendrites and somata. DCX positive profiles were observed making synaptic contacts. GABA positive axon terminals synapsed with DCX immunoreactive neuronal cell bodies. DCX and GABA positive terminals were shown synapsing with DCX and GABA immunoreactive dendritic profiles.

Conclusion: The results of the present study show that DCX immunoreactive newly born cells synapse with local GABAergic cells in immature and adult control and epileptic rats. This suggests that immature neurons contribute to the neuronal circuitry in control and absence epileptic pup and adult rats.

References:

1. Yu D. X., Di Giorgio F. P., Yao J., Marchetto M. C., Brennand K., Wright R., Mei A., McHenry L., Lisuk D., Grasmick J. M., Silberman P., Silberman G., Jappelli R., Gage F. H. Stem Cell Reports, 2011;2, 295-310.
2. Galvan V., Jin K. Clinical Interventions in Aging, 2007;2(4), 605-610.
3. Sirvanci S., Meshul C. K., Onat F., San T. Brain Research, 2005: 1053(1-2), 108-115.
4. Sirvanci S., Meshul C.K., Onat F., San T. Brain Research, 2003:988(1-2), 180-188.

ID-5. Nanoparticles: Biomedical applications and bio-safety issues

Type of presentation: Poster

ID-5-P-6111 A closer look at hydrophilic core-shell iron oxide nanoparticles for medical applications

Lassenberger A.¹, Grünewald T.², Zirbs R.¹, Lichtenegger H.², Reimhult E.¹

¹University of Natural Resources and Life Sciences BOKU Vienna, Institute for Biologically inspired Materials, ²University of Natural Resources and Life Sciences BOKU Vienna, Institute for Physics and Material Sciences

Email of the presenting author: andrea.lassenberger@boku.ac.at

The increasing use of nanomaterials in drug delivery, imaging and cosmetics requires a deeper understanding of how nanoparticles (NPs) interact with human cell membranes. This understanding can be realized by designing NPs that can be used for imaging and have controlled interactions with biological matter.

We have developed the synthesis of monodisperse superparamagnetic iron oxide core NPs with monodisperse hydrophilic polymer shells. These stealth NPs can easily be modified for diverse applications such as imaging and/or targeting, membrane interaction studies and drug delivery.

Monodisperse ($\sigma \leq 5\%$) oleic acid (OA) coated iron oxide NPs in the range of 3-10 nm were synthesized by a modified heat-up method [1]. The evolution of the nanoparticle nucleation and growth was investigated by a combination of image analysis based on HR-TEM and time-resolved small angle x-ray scattering; size, morphology, crystallinity and monodispersity were investigated.

In a next step, the iron oxide cores were made hydrophilic and biologically non-interacting by ligand replacement of OA with polyethyleneglycol (PEG), irreversible anchored to the NP surface by a nitrodopamine (NDA) anchor [2]. The ligand replacement, crucial removal of excess dispersant as function of purification protocol and the final grafting density of PEG chains were investigated by thermogravimetric analysis.

[1] T. Hyeon, S. S. Lee, J. Park, Y. Chung and H. B. Na, J. Am. Chem. Soc., **2001**, 123, 12798-12801

[2] E. Amstad, T. Gillich, I. Bilecka, M. Textor, and E. Reimhult, Nano Letters, **2009**, 12, 4042-4048

Acknowledgement: We thank Heinz Amenitsch for his help at Elettra synchrotron Trieste where the SAXS measurements were done and Oliver Bixner for helpful input and discussions. The author thanks the European Research Council under the European Union's Seventh Framework Programme (FP/2007-2013) / ERC Grant Agreement n. 310034 for financial support.

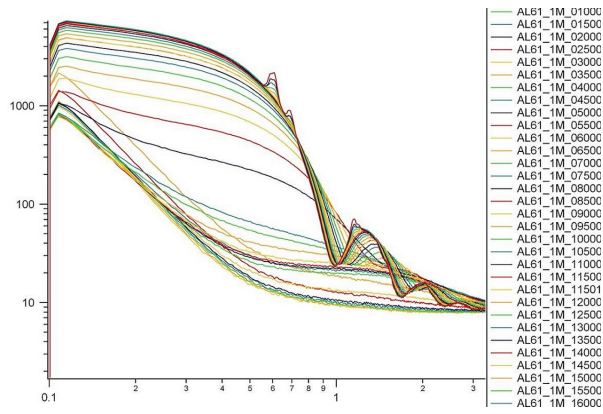


Fig. 1: Time-resolved small angle x-ray scattering of the iron oxide NP core synthesis

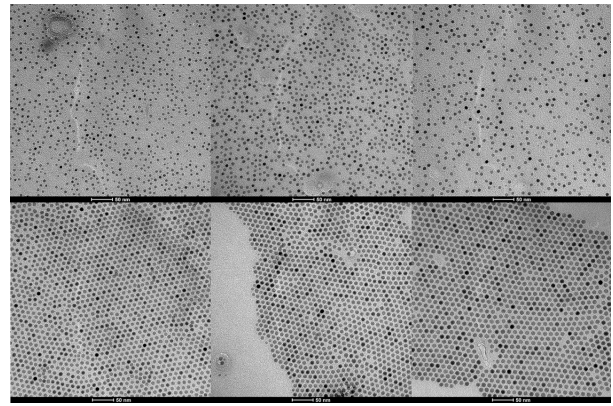


Fig. 2: HR-TEM micrographs of the NP growth in the core synthesis

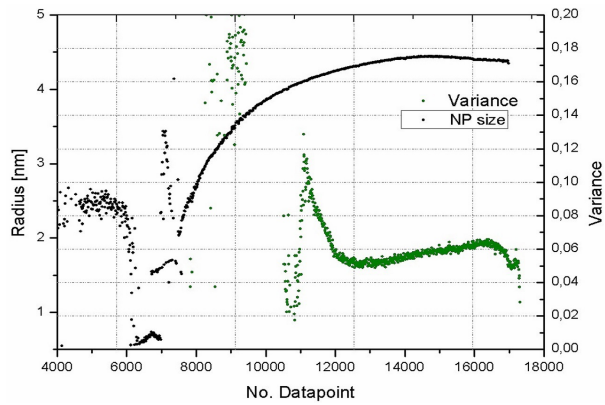


Fig. 3: Scattering data of the core synthesis: evolution of NP size and polydispersity over time

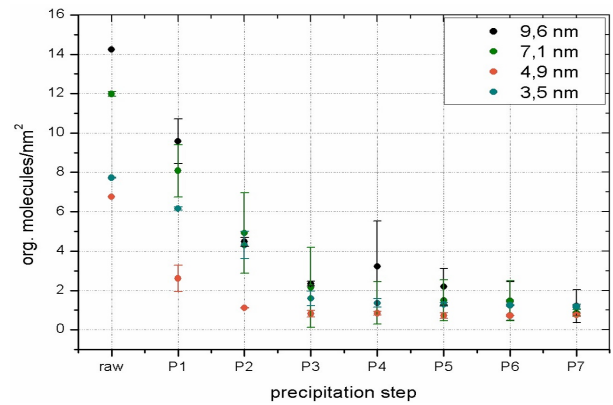


Fig. 4: Removal of excess dispersant by a magnetic decantation method and final grafting density of PEG

ID-10. Advances in sample preparation techniques

Type of presentation: Poster

ID-10-P-6139 Beam damage of embedding media sections and their investigations by SEM

Krzyžánek V.¹, Novotná V.², Hrubanová K.^{1,3}, Nebesářová J.⁴

¹Institute of Scientific Instrument ASČR, Department of Electron Microscopy, Brno, Czech Republic, ²Brno University of Technology, Department of Biomedical Engineering, Brno, Czech Republic, ³Brno University of Technology, Institute of Physical Engineering, Brno, Czech Republic, ⁴Biology center ASČR, Institute of Parasitology, České Budějovice, Czech Republic

Email of the presenting author: krzyzanek@isibrno.cz

A scanning transmission electron microscope (STEM) is useful device combining features of scanning and transmission electron microscopes. The sample in form of the ultrathin section is scanned by the electron probe and the transmitted electrons are detected. Except the dedicated STEMs [1] this mode can exist as options in both TEM and SEM [2]. The STEM based on the SEM equipped by a transmission detector was used for presented experiments. Nowadays, such low voltage STEM is more often used, and in many cases replaces the typical TEM. Here, we report investigations of embedding media that are typically used for TEM preparation of biological samples.

The STEM detector in SEM may be able to detect both bright-field and dark-fields images. It uses much lower acceleration voltages (30 kV and below) than conventional TEM or STEM. However, materials like biological samples, polymers including embedding media are electron beam sensitive. Two the most important beam damages are the mass loss and the contamination. Both types of damages depend on the used electron energy and the electron dose applied to the sample. The mass loss depends on the sample composition, and the contamination results from the poor vacuum in the specimen chamber of the SEM, cleanness of the sample surface, etc.

For simplicity, we have started with an estimation of the mass loss of different types of embedding media for biological samples. We collected bright-field (BF) images of the same area at the sample; an overview of the scanned area taken after multiple scans at a half magnification shows the increase of the signal due to the mass loss (Figure 1) and burning out in the center (Figure 1b). The Figure 2 shows the change of the BF signal to the total dose of electrons for all three embedding media of thickness 30 nm and 150 nm, respectively. The experiments have been done using SEM Magellan 400L (FEI) at 30 kV and lower and the lowest probe current (1.6 pA). Thin sections were cut from blocks of pure embedding media Epon, Spurr and LR White. The image processing was programmed in MATLAB.

Our preliminary results show that the mass loss at 30 keV can be high even at a dose of 500 el/nm², where for example, the Spurr and LR White sections were completely destroyed. The Epon resin is the most stable resin under electron beam. Samples of different thicknesses are investigated using different microscope settings and STEM imaging modes.

References:

- [1] Adv. Imaging & Electron Phys. 159 (2009), pp. 101-121 & 357-386.
- [2] A Bogner et al, Micron 38 (2007), p. 390.

Acknowledgement: The authors acknowledge the support by the grants 14-20012S (GAČR) and TE01020118 (TAČR).

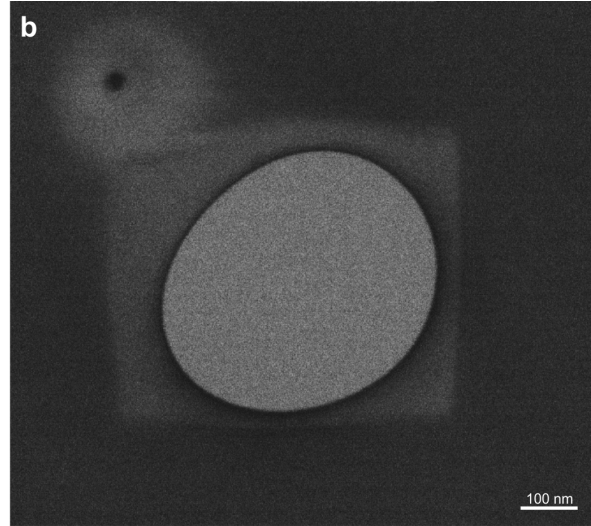
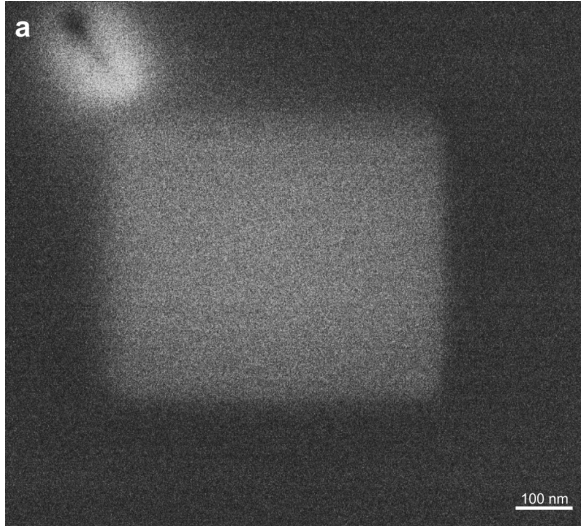


Fig. 1: Bright-field micrographs showing an overview of the multiple scanned area at a half magnification of Epon (a) and Spurr (b).

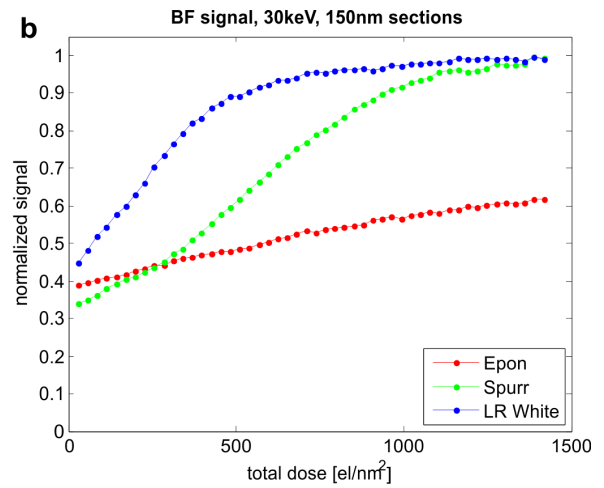
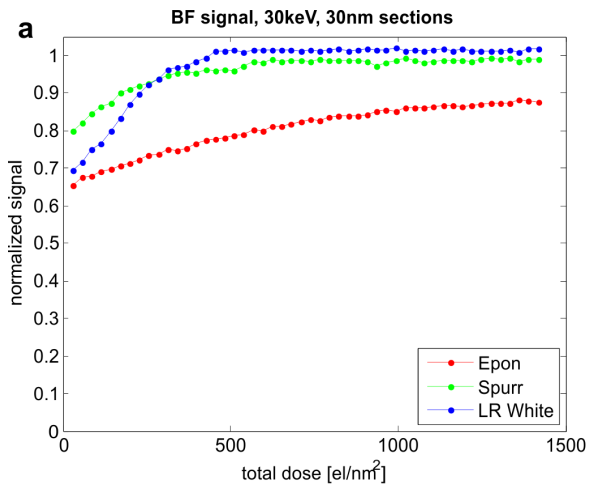


Fig. 2: Mean value of the bright-field signal in the scanned image vs. total irradiated dose for Epon, Spurr and LR White resins at 30 keV and thicknesses of the sections 30 nm (a) and 150 nm (b).

Index of Authors

Addadi S.

IT-4-P-6135 airSEM™, high resolution SEM operating in open air, a new approach for correlative imaging of hydrated samples

Afrimzon E.

LS-1-P-6103 The involvement of Nitric Oxide in breast cancer pathogenesis. Image based investigation at the resolution of single cell clusters (spheroids)

Bachmatiuk A.

IT-7-P-6127 In situ observations of confined platinum nanoparticles coalescing within carbon nanotubes

Balboni R.

IT-1-P-6140 Toward holographic approach to spherical aberration correction in STEM

Bals S.

IT-10-P-6113 On resolution in electron tomography of beam sensitive materials

Bared G.

IT-8-P-6122 High-Throughput Characterization of Nanoparticles by TEM

Bassem I.

IT-4-P-6101 Direct-write chlorine based etching of semiconductor devices utilizing a SEM

Batenburg K. J.

IT-10-P-6113 On resolution in electron tomography of beam sensitive materials

Bauerdick S.

IT-13-P-6109 High Resolution, Stable and Low Damage FIB Nanofabrication employing Gallium and New Ion Species

Belic D.

MS-8-P-6133 Metal Oxide Semiconductor Capacitor fabricated by Electron Beam Induced Deposition

Bertagnolli E.

IT-4-P-6101 Direct-write chlorine based etching of semiconductor devices utilizing a SEM
MS-8-P-6133 Metal Oxide Semiconductor Capacitor fabricated by Electron Beam Induced Deposition

Bethge O.

MS-8-P-6133 Metal Oxide Semiconductor Capacitor fabricated by Electron Beam Induced Deposition

Beuerman R. W.

LS-6-P-6121 Targeting Buried Features in a Resin-Embedded Mouse Cornea with Correlative X-ray and Electron Microscopy

Bleichrodt F.

IT-10-P-6113 On resolution in electron tomography of beam sensitive materials

Boekema E. J.

LS-4-P-6130 Structural characterization of Photosystem II supercomplex from Norway spruce indicates a different organization of light-harvesting antenna compared to flowering plants

Boothroyd C. B.

- IT-11-P-6126 Three-wave electron vortex lattices for vortex interferometry
-
- Boyd R.
IT-1-P-6140 Toward holographic approach to spherical aberration correction in STEM
-
- Brami Y.
IT-4-P-6136 airSEM™: Enabling EDX material analysis in open air
IT-4-P-6138 airSTEM: high resolution STEM detection in open air
-
- Brenny B. J.
IT-12-P-6115 Angle-Resolved Cathodoluminescence Imaging Spectroscopy
-
- Bruchhaus L.
IT-13-P-6109 High Resolution, Stable and Low Damage FIB Nanofabrication employing Gallium and New Ion Species
-
- Burke B.
LS-3-P-6085 3D structured illumination superresolution microscopy (3D-SIM) for studying the synaptonemal complex
-
- Buys A. V.
MS-14-P-6129 AFM and SEM studies on high fluence, low energy iodine implantation in 6H-SiC
-
- Calvino J. J.
MS-9-P-6131 On the complex superstructural ordering of oxygen absorption-desorption in the system $\text{BaFeO}_{3-\delta}$, $0 \leq \delta \leq 0.5$
-
- Celik M.
LS-1-P-6077 The importance of PTEN-PI3K-AKT Signaling Pathway on Invasive Breast Cancer Cell Lines MDA-MB-231
-
- Chang S.
IT-11-P-6126 Three-wave electron vortex lattices for vortex interferometry
-
- Chen D. L.
IT-10-P-6113 On resolution in electron tomography of beam sensitive materials
-
- Cherdyntseva S. V.
MS-6-P-6092 TEM of Layered Silicate Nanocomposites Based on Polyamide-6
-
- Chvalun S. N.
MS-6-P-6092 TEM of Layered Silicate Nanocomposites Based on Polyamide-6
-
- Cichocka M. O.
IT-7-P-6127 In situ observations of confined platinum nanoparticles coalescing within carbon nanotubes
-
- Cilingir O. T.
LS-14-P-6123 Time-Dependent Changes Between Immature Neurons Contacting GABAergic Nerve Cells Using Double Immunogold Labeling in Wistar and GAERS rats
-
- Coenen T.
IT-12-P-6115 Angle-Resolved Cathodoluminescence Imaging Spectroscopy
-
- Cordill M. J.
IT-7-P-6125 Beyond Current SEM - AFM Solutions: A Highly Flexible in-situ AFM for Correlated Microscopy in Micromechanical Testing
-
- Czigány Z.
IT-16-P-6075 Examination of the possibility of application of the Monte Carlo method for study of electron diffraction of textured nanocomposite materials

Dadosh T.

LS-3-P-6119 Polarized Emission of CdSe Nanorods to Probe Three-Dimensional Structural Dynamics of Single Molecular Motor Proteins

Dalgarno P. A.

LS-3-P-6108 3D Super Resolution Microscopy: Multi-plane Imaging

Del Río E.

MS-9-P-6131 On the complex superstructural ordering of oxygen absorption-desorption in the system $\text{BaFeO}_{3-\delta}$, $0 \leq \delta \leq 0.5$

Delgado J. J.

MS-9-P-6131 On the complex superstructural ordering of oxygen absorption-desorption in the system $\text{BaFeO}_{3-\delta}$, $0 \leq \delta \leq 0.5$

Deutsch M.

LS-1-P-6103 The involvement of Nitric Oxide in breast cancer pathogenesis. Image based investigation at the resolution of single cell clusters (spheroids)

Diroll B. T.

LS-3-P-6119 Polarized Emission of CdSe Nanorods to Probe Three-Dimensional Structural Dynamics of Single Molecular Motor Proteins

Dufresne C.

IT-8-P-6122 High-Throughput Characterization of Nanoparticles by TEM

Dunnin-Borkowski R. E.

IT-11-P-6126 Three-wave electron vortex lattices for vortex interferometry

Dwyer C.

IT-11-P-6126 Three-wave electron vortex lattices for vortex interferometry

Décamps B.

MS-9-P-6134 TEM of radiation damage in ferritics: role of image forces

Eckert J.

IT-7-P-6127 In situ observations of confined platinum nanoparticles coalescing within carbon nanotubes

Eggeling C.

LS-2-P-6117 Multi-protein assemblies underlie the mesoscale organization of the plasma membrane

El Hadri A.

MS-9-P-6131 On the complex superstructural ordering of oxygen absorption-desorption in the system $\text{BaFeO}_{3-\delta}$, $0 \leq \delta \leq 0.5$

Erickson B.

IT-7-P-6125 Beyond Current SEM - AFM Solutions: A Highly Flexible in-situ AFM for Correlated Microscopy in Micromechanical Testing

Fantner E. J.

IT-7-P-6125 Beyond Current SEM - AFM Solutions: A Highly Flexible in-situ AFM for Correlated Microscopy in Micromechanical Testing

Fantner G. E.

IT-7-P-6125 Beyond Current SEM - AFM Solutions: A Highly Flexible in-situ AFM for Correlated Microscopy in Micromechanical Testing

Frabboni S.

-
- IT-1-P-6140 Toward holographic approach to spherical aberration correction in STEM
-
- Frank L.
IT-16-P-6106 Improving quantification in Scanning Electron Microscopy by comparing transmission experiments with Monte Carlo Simulation.
-
- Friedrich H.
IT-10-P-6113 On resolution in electron tomography of beam sensitive materials
-
- Fu L.
IT-7-P-6127 In situ observations of confined platinum nanoparticles coalescing within carbon nanotubes
-
- Garcia-Martinez J.
MS-10-P-6107 Mesoporous zeolite Y studied by rotation electron diffraction and electron tomography
-
- García-García F. J.
MS-9-P-6131 On the complex superstructural ordering of oxygen absorption-desorption in the system $\text{BaFeO}_{3-\delta}$, $0 \leq \delta \leq 0.5$
-
- Gavagnin M.
MS-8-P-6133 Metal Oxide Semiconductor Capacitor fabricated by Electron Beam Induced Deposition
-
- Gazzadi G. C.
IT-1-P-6140 Toward holographic approach to spherical aberration correction in STEM
-
- Gelb J.
MS-4-P-6120 Microstructure Evolution in the Corrosion of Steel Alloys
LS-6-P-6121 Targeting Buried Features in a Resin-Embedded Mouse Cornea with Correlative X-ray and Electron Microscopy
-
- Goladman Y. E.
LS-3-P-6119 Polarized Emission of CdSe Nanorods to Probe Three-Dimensional Structural Dynamics of Single Molecular Motor Proteins
-
- Gonzalez-Martinez I. G.
IT-7-P-6127 In situ observations of confined platinum nanoparticles coalescing within carbon nanotubes
-
- González-Calbet J. M.
MS-9-P-6131 On the complex superstructural ordering of oxygen absorption-desorption in the system $\text{BaFeO}_{3-\delta}$, $0 \leq \delta \leq 0.5$
-
- Gorantla S. M.
IT-7-P-6127 In situ observations of confined platinum nanoparticles coalescing within carbon nanotubes
-
- Goris B.
IT-10-P-6113 On resolution in electron tomography of beam sensitive materials
-
- Granick S.
IT-3-P-6078 Beyond Electron Microscopy with Super-Resolution Nanoscopy in Soft Matter
-
- Grillo V.
IT-1-P-6140 Toward holographic approach to spherical aberration correction in STEM
-
- Grünewald T.
ID-5-P-6111 A closer look at hydrophilic core-shell iron oxide nanoparticles for medical applications

Guastamacchia M.

LS-3-P-6108 3D Super Resolution Microscopy: Multi-plane Imaging

Gursoy D.

LS-14-P-6123 Time-Dependent Changes Between Immature Neurons Contacting GABAergic Nerve Cells Using Double Immunogold Labeling in Wistar and GAERS rats

Gökdeniz Z. G.

IT-4-P-6101 Direct-write chlorine based etching of semiconductor devices utilizing a SEM

Heidari Mezerji H.

IT-10-P-6113 On resolution in electron tomography of beam sensitive materials

Hell S. W.

LS-2-P-6117 Multi-protein assemblies underlie the mesoscale organization of the plasma membrane

Hernando M.

MS-9-P-6131 On the complex superstructural ordering of oxygen absorption-desorption in the system $\text{BaFeO}_{3-\delta}$, $0 \leq \delta \leq 0.5$

Hernández J. C.

MS-9-P-6131 On the complex superstructural ordering of oxygen absorption-desorption in the system $\text{BaFeO}_{3-\delta}$, $0 \leq \delta \leq 0.5$

Hidaka K.

IT-16-P-6132 Resolution Simulation of the Practical Rayleigh Criterion Taking Account of Particle Diameter and Contrast-to-Noise Ratio for Scanning Electron Microscopes

Hofer F.

IT-7-P-6125 Beyond Current SEM – AFM Solutions: A Highly Flexible in-situ AFM for Correlated Microscopy in Micromechanical Testing

Hong S. H.

MS-14-P-6116 Ex-situ TEM analysis on extra capacities of SnO_2 lithium-ion battery anode material

Honigmann A.

LS-2-P-6117 Multi-protein assemblies underlie the mesoscale organization of the plasma membrane

Horn H. F.

LS-3-P-6085 3D structured illumination superresolution microscopy (3D-SIM) for studying the synaptonemal complex

Hrubanová K.

ID-10-P-6139 Beam damage of embedding media sections and their investigations by SEM

Hébert C.

MS-9-P-6134 TEM of radiation damage in ferritics: role of image forces

Ilík P.

LS-4-P-6130 Structural characterization of Photosystem II supercomplex from Norway spruce indicates a different organization of light-harvesting antenna compared to flowering plants

Inan S.

LS-1-P-6077 The importance of PTEN-PI3K-AKT Signaling Pathway on Invasive Breast Cancer Cell Lines MDA-MB-231

Ivanov-Pankov S.

IT-8-P-6122 High-Throughput Characterization of Nanoparticles by TEM

Jede R.

IT-13-P-6109 High Resolution, Stable and Low Damage FIB Nanofabrication employing Gallium and New Ion Species

Kang K.

MS-14-P-6116 Ex-situ TEM analysis on extra capacities of SnO₂ lithium-ion battery anode material

Kang S. J.

MS-3-P-6128 TEM study of Epitaxial SrIrO₃ Thin Films Grown by Pulsed Laser Deposition Technique

Karimi E.

IT-1-P-6140 Toward holographic approach to spherical aberration correction in STEM

Kim E.

MS-3-P-6128 TEM study of Epitaxial SrIrO₃ Thin Films Grown by Pulsed Laser Deposition Technique

Kim M.

MS-3-P-6128 TEM study of Epitaxial SrIrO₃ Thin Films Grown by Pulsed Laser Deposition Technique

MS-3-P-6128 TEM study of Epitaxial SrIrO₃ Thin Films Grown by Pulsed Laser Deposition Technique

MS-14-P-6116 Ex-situ TEM analysis on extra capacities of SnO₂ lithium-ion battery anode material

Kim W. S.

MS-14-P-6116 Ex-situ TEM analysis on extra capacities of SnO₂ lithium-ion battery anode material

King J. T.

IT-3-P-6078 Beyond Electron Microscopy with Super-Resolution Nanoscopy in Soft Matter

Kolonits T.

IT-16-P-6075 Examination of the possibility of application of the Monte Carlo method for study of electron diffraction of textured nanocomposite materials

Kolosov V. Y.

MS-1-P-6137 Sb-Te films: crystallized microstructures and "transrotation" examined by TEM

Konvalina I.

IT-16-P-6106 Improving quantification in Scanning Electron Microscopy by comparing transmission experiments with Monte Carlo Simulation.

Kouřil R.

LS-4-P-6130 Structural characterization of Photosystem II supercomplex from Norway spruce indicates a different organization of light-harvesting antenna compared to flowering plants

Kreith J.

IT-7-P-6125 Beyond Current SEM - AFM Solutions: A Highly Flexible in-situ AFM for Correlated Microscopy in Micromechanical Testing

Krzyžánek V.

ID-10-P-6139 Beam damage of embedding media sections and their investigations by SEM

Kuhudzai R. J.

MS-14-P-6129 AFM and SEM studies on high fluence, low energy iodine implantation in 6H-SiC

Kuo C. T.

MS-3-P-6128 TEM study of Epitaxial SrIrO₃ Thin Films Grown by Pulsed Laser Deposition Technique

Lang T.

LS-2-P-6117 Multi-protein assemblies underlie the mesoscale organization of the plasma membrane

Lassenberger A.

- ID-5-P-6111 A closer look at hydrophilic core-shell iron oxide nanoparticles for medical applications
-
- Lechner L.
MS-4-P-6120 Microstructure Evolution in the Corrosion of Steel Alloys
LS-6-P-6121 Targeting Buried Features in a Resin-Embedded Mouse Cornea with Correlative X-ray and Electron Microscopy
-
- Lee S. Y.
MS-14-P-6116 Ex-situ TEM analysis on extra capacities of SnO₂ lithium-ion battery anode material
-
- Li K. H.
MS-10-P-6107 Mesoporous zeolite Y studied by rotation electron diffraction and electron tomography
-
- Lichtenegger H.
ID-5-P-6111 A closer look at hydrophilic core-shell iron oxide nanoparticles for medical applications
-
- Liddicoat P. V.
IT-17-P-6104 Sub-angstrom resolution in 3D - Exploring high-resolution atom probe microscopy
-
- Lippert L.
LS-3-P-6119 Polarized Emission of CdSe Nanorods to Probe Three-Dimensional Structural Dynamics of Single Molecular Motor Proteins
-
- Lo Schiavo V.
LS-3-P-6108 3D Super Resolution Microscopy: Multi-plane Imaging
-
- Lugstein A.
IT-4-P-6101 Direct-write chlorine based etching of semiconductor devices utilizing a SEM
-
- Löffler J.
MS-9-P-6134 TEM of radiation damage in ferritics: role of image forces
-
- Mafakheri E.
IT-1-P-6140 Toward holographic approach to spherical aberration correction in STEM
-
- Malherbe J. B.
MS-14-P-6129 AFM and SEM studies on high fluence, low energy iodine implantation in 6H-SiC
-
- Martin-Fernandez M.
LS-3-P-6108 3D Super Resolution Microscopy: Multi-plane Imaging
-
- Mazarov P.
IT-13-P-6109 High Resolution, Stable and Low Damage FIB Nanofabrication employing Gallium and New Ion Species
-
- Merkle A.
MS-4-P-6120 Microstructure Evolution in the Corrosion of Steel Alloys
LS-6-P-6121 Targeting Buried Features in a Resin-Embedded Mouse Cornea with Correlative X-ray and Electron Microscopy
-
- Meshul C. K.
LS-14-P-6123 Time-Dependent Changes Between Immature Neurons Contacting GABAergic Nerve Cells Using Double Immunogold Labeling in Wistar and GAERS rats
-
- Mika F.
IT-16-P-6106 Improving quantification in Scanning Electron Microscopy by comparing transmission experiments with Monte Carlo Simulation.
-
- Mika J.
IT-4-P-6101 Direct-write chlorine based etching of semiconductor devices utilizing a SEM

Milstein Y.

IT-4-P-6135 airSEM™, high resolution SEM operating in open air, a new approach for correlative imaging of hydrated samples

IT-4-P-6136 airSEM™: Enabling EDX material analysis in open air

IT-4-P-6138 airSTEM: high resolution STEM detection in open air

Moore C.

LS-14-P-6123 Time-Dependent Changes Between Immature Neurons Contacting GABAergic Nerve Cells Using Double Immunogold Labeling in Wistar and GAERS rats

Moshkov S.

LS-1-P-6103 The involvement of Nitric Oxide in breast cancer pathogenesis. Image based investigation at the resolution of single cell clusters (spheroids)

Murray C. B.

LS-3-P-6119 Polarized Emission of CdSe Nanorods to Probe Three-Dimensional Structural Dynamics of Single Molecular Motor Proteins

Müllerová I.

IT-16-P-6106 Improving quantification in Scanning Electron Microscopy by comparing transmission experiments with Monte Carlo Simulation.

Nadzeyka A.

IT-13-P-6109 High Resolution, Stable and Low Damage FIB Nanofabrication employing Gallium and New Ion Species

Nebesářová J.

ID-10-P-6139 Beam damage of embedding media sections and their investigations by SEM

Neumann E.

LS-2-P-6118 SEM/FIB of cell-interface in 3D-electrodes

Noh T. W.

MS-3-P-6128 TEM study of Epitaxial SrIrO₃ Thin Films Grown by Pulsed Laser Deposition Technique

Nosek L.

LS-4-P-6130 Structural characterization of Photosystem II supercomplex from Norway spruce indicates a different organization of light-harvesting antenna compared to flowering plants

Novotná V.

ID-10-P-6139 Beam damage of embedding media sections and their investigations by SEM

Offenhäusser A.

LS-2-P-6118 SEM/FIB of cell-interface in 3D-electrodes

Onal T.

LS-1-P-6077 The importance of PTEN-PI3K-AKT Signaling Pathway on Invasive Breast Cancer Cell Lines MDA-MB-231

Onat F.

LS-14-P-6123 Time-Dependent Changes Between Immature Neurons Contacting GABAergic Nerve Cells Using Double Immunogold Labeling in Wistar and GAERS rats

Onuki J.

IT-16-P-6132 Resolution Simulation of the Practical Rayleigh Criterion Taking Account of Particle Diameter and Contrast-to-Noise Ratio for Scanning Electron Microscopes

Orehov A. S.

MS-6-P-6092 TEM of Layered Silicate Nanocomposites Based on Polyamide-6

Ozbilgin K.

LS-1-P-6077 The importance of PTEN-PI3K-AKT Signaling Pathway on Invasive Breast Cancer Cell Lines MDA-MB-231

Ozgul M.

LS-1-P-6077 The importance of PTEN-PI3K-AKT Signaling Pathway on Invasive Breast Cancer Cell Lines MDA-MB-231

Padmanabhan S.

LS-6-P-6121 Targeting Buried Features in a Resin-Embedded Mouse Cornea with Correlative X-ray and Electron Microscopy

Panaitov G.

LS-2-P-6118 SEM/FIB of cell-interface in 3D-electrodes

Park C.

LS-6-P-6121 Targeting Buried Features in a Resin-Embedded Mouse Cornea with Correlative X-ray and Electron Microscopy

Park K. Y.

MS-14-P-6116 Ex-situ TEM analysis on extra capacities of SnO₂ lithium-ion battery anode material

Parras M.

MS-9-P-6131 On the complex superstructural ordering of oxygen absorption-desorption in the system BaFeO_{3-δ}, 0 ≤ δ ≤ 0.5

Plank H.

IT-7-P-6125 Beyond Current SEM - AFM Solutions: A Highly Flexible in-situ AFM for Correlated Microscopy in Micromechanical Testing

Polman A.

IT-12-P-6115 Angle-Resolved Cathodoluminescence Imaging Spectroscopy

Prokhotseva A.

MS-9-P-6134 TEM of radiation damage in ferritics: role of image forces

Pérez-Omil J. A.

MS-9-P-6131 On the complex superstructural ordering of oxygen absorption-desorption in the system BaFeO_{3-δ}, 0 ≤ δ ≤ 0.5

Quang H. T.

IT-7-P-6127 In situ observations of confined platinum nanoparticles coalescing within carbon nanotubes

Ravid O.

LS-1-P-6103 The involvement of Nitric Oxide in breast cancer pathogenesis. Image based investigation at the resolution of single cell clusters (spheroids)

Reimhult E.

ID-5-P-6111 A closer look at hydrophilic core-shell iron oxide nanoparticles for medical applications

Rizzoli S. O.

LS-2-P-6117 Multi-protein assemblies underlie the mesoscale organization of the plasma membrane

Rümmeli M. H.

IT-7-P-6127 In situ observations of confined platinum nanoparticles coalescing within carbon nanotubes

Saka S. K.

- LS-2-P-6117 Multi-protein assemblies underlie the mesoscale organization of the plasma membrane
-
- Santoro F.
LS-2-P-6118 SEM/FIB of cell-interface in 3D-electrodes
-
- Sasaki T.
IT-16-P-6132 Resolution Simulation of the Practical Rayleigh Criterion Taking Account of Particle Diameter and Contrast-to-Noise Ratio for Scanning Electron Microscopes
-
- Sato M.
IT-16-P-6132 Resolution Simulation of the Practical Rayleigh Criterion Taking Account of Particle Diameter and Contrast-to-Noise Ratio for Scanning Electron Microscopes
-
- Schaeublin R. E.
MS-9-P-6134 TEM of radiation damage in ferritics: role of image forces
-
- Schwamm C. L.
MS-1-P-6137 Sb-Te films: crystallized microstructures and "transrotation" examined by TEM
-
- Shachal D.
IT-4-P-6135 airSEM™, high resolution SEM operating in open air, a new approach for correlative imaging of hydrated samples
IT-4-P-6136 airSEM™: Enabling EDX material analysis in open air
IT-4-P-6138 airSTEM: high resolution STEM detection in open air
-
- Shafran Y.
LS-1-P-6103 The involvement of Nitric Oxide in breast cancer pathogenesis. Image based investigation at the resolution of single cell clusters (spheroids)
-
- Shainberg A.
LS-1-P-6103 The involvement of Nitric Oxide in breast cancer pathogenesis. Image based investigation at the resolution of single cell clusters (spheroids)
-
- Shawrav M. M.
IT-4-P-6101 Direct-write chlorine based etching of semiconductor devices utilizing a SEM
MS-8-P-6133 Metal Oxide Semiconductor Capacitor fabricated by Electron Beam Induced Deposition
-
- Sirvanci S.
LS-14-P-6123 Time-Dependent Changes Between Immature Neurons Contacting GABAergic Nerve Cells Using Double Immunogold Labeling in Wistar and GAERS rats
-
- Soares J. M.
MS-12-P-6114 Scanning electron microscopy and energy dispersive spectroscopy to study the nanomagnetism in minerals
-
- Sobolev M.
LS-1-P-6103 The involvement of Nitric Oxide in breast cancer pathogenesis. Image based investigation at the resolution of single cell clusters (spheroids)
-
- Sohn W.
MS-3-P-6128 TEM study of Epitaxial SrIrO₃ Thin Films Grown by Pulsed Laser Deposition Technique
-
- Stewart C. L.
LS-3-P-6085 3D structured illumination superresolution microscopy (3D-SIM) for studying the synaptonemal complex
-
- Strunz T.

IT-7-P-6125 Beyond Current SEM – AFM Solutions: A Highly Flexible in-situ AFM for Correlated Microscopy in Micromechanical Testing

Tanimura K.

IT-8-P-6102 Development of femtosecond time-resolved relativistic-energy electron microscopy

Temel M.

LS-1-P-6077 The importance of PTEN-PI3K-AKT Signaling Pathway on Invasive Breast Cancer Cell Lines MDA-MB-231

Tiefenbacher S.

MS-8-P-6133 Metal Oxide Semiconductor Capacitor fabricated by Electron Beam Induced Deposition

Turkoz Uluer E.

LS-1-P-6077 The importance of PTEN-PI3K-AKT Signaling Pathway on Invasive Breast Cancer Cell Lines MDA-MB-231

Urakawa J.

IT-8-P-6102 Development of femtosecond time-resolved relativistic-energy electron microscopy

Varela A.

MS-9-P-6131 On the complex superstructural ordering of oxygen absorption-desorption in the system $\text{BaFeO}_{3-\delta}$, $0 \leq \delta \leq 0.5$

Vasilev A. L.

MS-6-P-6092 TEM of Layered Silicate Nanocomposites Based on Polyamide-6

Veretennikov L. M.

MS-1-P-6137 Sb-Te films: crystallized microstructures and "transrotation" examined by TEM

Vorobev M.

IT-4-P-6105 New opportunities for biomedical research in the Saint-Petersburg State University

Walker C. G.

IT-16-P-6106 Improving quantification in Scanning Electron Microscopy by comparing transmission experiments with Monte Carlo Simulation.

Wan W.

MS-10-P-6107 Mesoporous zeolite Y studied by rotation electron diffraction and electron tomography

Wanzenboeck H.

MS-8-P-6133 Metal Oxide Semiconductor Capacitor fabricated by Electron Beam Induced Deposition

Wanzenboeck H. D.

IT-4-P-6101 Direct-write chlorine based etching of semiconductor devices utilizing a SEM

Warner J. H.

IT-7-P-6127 In situ observations of confined platinum nanoparticles coalescing within carbon nanotubes

Webb S. E.

LS-3-P-6108 3D Super Resolution Microscopy: Multi-plane Imaging

Weigel W.

IT-8-P-6122 High-Throughput Characterization of Nanoparticles by TEM

Winkler R.

- IT-7-P-6125 Beyond Current SEM – AFM Solutions: A Highly Flexible in-situ AFM for Correlated Microscopy in Micromechanical Testing
-
- Wong E. S.
LS-3-P-6085 3D structured illumination superresolution microscopy (3D-SIM) for studying the synaptonemal complex
-
- Wright G. D.
LS-3-P-6085 3D structured illumination superresolution microscopy (3D-SIM) for studying the synaptonemal complex
-
- Wu W.
MS-9-P-6134 TEM of radiation damage in ferritics: role of image forces
-
- Xiao C. H.
MS-10-P-6107 Mesoporous zeolite Y studied by rotation electron diffraction and electron tomography
-
- Yang J.
IT-8-P-6102 Development of femtosecond time-resolved relativistic-energy electron microscopy
-
- Yoshida Y.
IT-8-P-6102 Development of femtosecond time-resolved relativistic-energy electron microscopy
-
- Zeiner C.
IT-4-P-6101 Direct-write chlorine based etching of semiconductor devices utilizing a SEM
-
- Zhao J.
IT-7-P-6127 In situ observations of confined platinum nanoparticles coalescing within carbon nanotubes
-
- Zirbs R.
ID-5-P-6111 A closer look at hydrophilic core-shell iron oxide nanoparticles for medical applications
-
- Zou X. D.
MS-10-P-6107 Mesoporous zeolite Y studied by rotation electron diffraction and electron tomography
-
- Zurgil N.
LS-1-P-6103 The involvement of Nitric Oxide in breast cancer pathogenesis. Image based investigation at the resolution of single cell clusters (spheroids)
-
- de Araújo J. H.
MS-12-P-6114 Scanning electron microscopy and energy dispersive spectroscopy to study the nanomagnetism in minerals
-
- de Picciotto R.
IT-4-P-6135 airSEM™, high resolution SEM operating in open air, a new approach for correlative imaging of hydrated samples
IT-4-P-6136 airSEM™: Enabling EDX material analysis in open air
IT-4-P-6138 airSTEM: high resolution STEM detection in open air
-
- de With G.
IT-10-P-6113 On resolution in electron tomography of beam sensitive materials
-
- van der Berg N. G.
MS-14-P-6129 AFM and SEM studies on high fluence, low energy iodine implantation in 6H-SiC